Monthly Notices
of the
ROYAL ASTRONOMICAL SOCIETY

MNRAS **439,** 2211–2270 (2014)
Advance Access publication 2014 February 19

doi:10.1093/mnras/stt2033

Optically visible post-AGB/RGB stars and young stellar objects in the Small Magellanic Cloud: candidate selection, spectral energy distributions and spectroscopic examination

D. Kamath,[1,2]★ P. R. Wood[1] and H. Van Winckel[2]

[1]*Research School of Astronomy and Astrophysics, Mount Stromlo Observatory, Weston Creek, ACT 2611, Australia*
[2]*Instituut voor Sterrenkunde, K.U.Leuven, Celestijnenlaan 200D bus 2401, B-3001 Leuven, Belgium*

Accepted 2013 October 10. Received 2013 September 18; in original form 2013 April 26

ABSTRACT

We have carried out a search for optically visible post-asymptotic giant branch (post-AGB) candidates in the Small Magellanic Cloud (SMC). First, we used mid-IR observations from the *Spitzer Space Telescope* to select optically visible candidates with excess mid-IR flux and then we obtained low-resolution optical spectra for 801 of the candidates. After removing poor-quality spectra and contaminants, such as M-stars, C-stars, planetary nebulae, quasi-stellar objects and background galaxies, we ended up with a final sample of 63 high-probability post-AGB/RGB candidates of A–F spectral type. From the spectral observations, we estimated the stellar parameters: effective temperature ($T_{\rm eff}$), surface gravity ($\log g$) and metallicity ([Fe/H]). We also estimated the reddening and deduced the luminosity using the stellar parameters combined with photometry. For the post-AGB/RGB candidates, we found that the metallicity distribution peaks at [Fe/H] ≈ -1.00 dex. Based on a luminosity criterion, 42 of these 63 sources were classified as post-red giant branch (post-RGB) candidates and the remaining 21 as post-AGB candidates. From the spectral energy distributions, we were able to infer that 6 of the 63 post-AGB/RGB candidates have a surrounding circumstellar shell suggesting that they are single stars, while 27 of the post-AGB/RGB candidates have a surrounding disc, suggesting that they lie in binary systems. For the remaining 30 post-AGB/RGB candidates the nature of the circumstellar environment was unclear. Variability is displayed by 38 of the 63 post-AGB/RGB candidates with the most common variability types being the Population II Cepheids (including RV-Tauri stars) and semiregular variables. This study has also revealed a new RV Tauri star in the SMC, J005107.19-734133.3, which shows signs of *s*-process enrichment. From the numbers of post-AGB/RGB stars in the SMC, we were able to estimate evolutionary rates. We find that the number of post-AGB and post-RGB candidates that we have identified are in good agreement with the stellar evolution models with some mass-loss in the post-AGB phase and a small amount of re-accretion in the lower luminosity post-RGB phase. This study also resulted in a new sample of 40 young stellar objects (YSOs) of A–F spectral type. The 40 YSO candidates for which we could estimate stellar parameters are luminous and of high mass ($\sim$3–10 $M_{\odot}$). They lie on the cool side of the usually adopted birthline in the HR-diagram. This line separates visually obscured protostars from optically visible pre-main-sequence stars, meaning that our YSO candidates have become optically visible in the region of the HR diagram usually reserved for obscured protostars. Additionally, we also identified a group of 63 objects whose spectra are dominated by emission lines and in some cases, a significant UV continuum. These objects are very likely to be either hot post-AGB/RGB candidates or luminous YSOs.

Key words: methods: observational – techniques: photometric – techniques: spectroscopic – stars: AGB and post-AGB – stars: fundamental parameters – Magellanic Clouds.

★ E-mail: devika@ster.kuleuven.be

1 INTRODUCTION

The post-asymptotic giant branch (post-AGB) phase of evolution is a transient phase between the AGB and planetary nebula (PN) phases of stellar evolution. A super-wind with mass-loss rates up to 10^{-4} $M_{\odot}$ yr^{-1} generally terminates the AGB phase, reducing the hydrogen-rich envelope to small values. Subsequently, the radius of the central star decreases and within about 10^2–10^4 yr, the star evolves to higher temperatures (from 3×10^3 K on the AGB to $\sim 3 \times 10^4$ K where PN formation begins) with a constant luminosity (e.g. Schönberner 1983; Vassiliadis & Wood 1993, 1994). The ejected circumstellar matter expands and cools during the post-AGB phase, resulting in stars with a large mid-IR excess (see Kwok 1993; Habing & Olofsson 2003; Van Winckel 2003, for reviews). Post-AGB stars emit radiation over a broad spectral range owing to a combination of high temperatures in the photosphere and low temperatures in circumstellar dust. This enables the simultaneous study of the stellar photosphere and the circumstellar environment, with the central star emitting in the ultraviolet (UV), optical and near-infrared (IR), and the cool circumstellar environment radiating in the near- and mid-IR. As the post-AGB star evolves to higher temperatures, the ejected circumstellar material gets ionized to form a PN, after which the central star declines in luminosity and cools to become a white dwarf star. These phenomenon mark the end of stellar evolution for low-to-intermediate-mass single stars.

For stars in binary systems, a different mechanism can terminate the red giant evolution. The large expansions that occur when a star becomes a red giant can cause the primary star to overfill its Roche lobe. Theory suggests that Roche lobe overflow during the red giant phase will lead to runaway mass transfer on a dynamical or thermal time-scale, until all that is left of the mass-losing star is the He or C/O core of the red giant, orbiting in a binary system: alternatively, complete merging may occur (e.g. Paczyński & Sienkiewicz 1972; Iben, Tutukov & Yungelson 1996; Han, Podsiadlowski & Eggleton 1995). This process occurs for binaries with periods on the main sequence in the approximate range 20–1000 d, from low on the red giant branch (RGB) to the tip of the AGB. The outcome of these systems are as of yet difficult to predict as many binary interaction process are poorly understood. A significant fraction of the ejected matter may end up in a circumbinary disc of dust and gas, and inside the disc is a binary system containing a post-AGB star or a post-RGB star. The distinction between these two cases is as follows: if the primary star fills its Roche lobe before reaching the RGB tip,[1] it will be referred to as a post-RGB star while if the primary star successfully evolves past the RGB tip on its second ascent of the giant branch it will be referred to as a post-AGB star.

One of the challenges in the study of the post-AGB phase of evolution is the identification of post-AGB objects as they have a very short lifetime. Since they have dusty circumstellar envelopes, the detection of cold circumstellar dust using mid-IR photometry is an efficient method to select and study them. The first extensive search for these objects was initiated in the mid-80's using results from the *Infrared Astronomical Satellite* (*IRAS*). The large-scale mid-IR *IRAS* mission enabled the identification of post-AGB stars in the Galaxy (Kwok 1993). The Toruń catalogue (Szczerba et al. 2007) for Galactic post-AGB stars lists around 391 very likely post-AGB objects. The Galactic sample of optically visible post-AGB objects has revealed two highly distinct populations: one with cold, detached, expanding dust shells (these probably arise from single stars and produce 'shell' or 'outflow sources'; Van Winckel 2003), and another with hot dust and circumstellar discs (these arise from binary stars and are called 'disc sources'; de Ruyter et al. 2006; Van Winckel 2007; Gielen et al. 2009; Van Winckel et al. 2009; Dermine et al. 2012). This is as expected from the single and binary star evolution scenarios described above.

So far, in the Galaxy, the luminosities (and hence initial masses) of the diverse group of post-AGB stars are badly affected by their unknown distances, making it difficult to use the observational characteristics of these interesting objects to throw light on the poorly understood late stages of stellar evolution.

The Magellanic clouds are well suited for the identification and observation of post-AGB stars. The well-constrained distances to these extragalactic systems mean that distance-dependent parameters such as luminosities can be determined accurately. The Large Magellanic Cloud (LMC) and Small Magellanic Cloud (SMC) are both very suitable environments to locate individual post-AGB objects and study their evolution as a function of initial mass and metallicity.

In the SMC, only five possible post-AGB candidates have been identified previously. One *IRAS* source (IRAS 00350-7436) is believed to be a post-AGB star (Whitelock et al. 1989). Kučinskas et al. (2000) identified a near-IR object in the field of the SMC cluster NGC 330 using *ISO* (*Infrared Space Observatory*) observations. This object was classified as a likely post-AGB star in a proto-PN stage, or a Be-supergiant. Using low-resolution mid-IR spectra from the *Spitzer Space Telescope* (*SST*), Kraemer et al. (2006) identified a possible isolated post-AGB star (MSX SMC 029) in the SMC. Volk et al. (2011) identified two 21 μm sources in the SMC (J004441.04-732136.44 and J010546.40-714705.27). For the Galaxy, the unidentified 21 μm feature only occurs around C-rich post-AGB stars. J004441.04-732136.44 was also identified in a preliminary version of this study by Wood et al. (2011), who examined some of the brighter sources presented here and found a number of post-AGB candidates. De Smedt et al. (2012) carried out a detailed chemical abundance analysis on J004441.04-732136.44 and found it to be indeed C-rich and an extremely *s*-process enriched shell source.

In the LMC, post-AGB candidates have been identified by van Aarle et al. (2011) and references therein. van Aarle et al. (2011) constructed a catalogue of 1337 optically visible post-AGB candidates in the LMC based on mid-IR selection criteria and examination of spectral energy distributions (SEDs). They also carried out a spectroscopic examination of 105 candidates which resulted in 70 likely post-AGB candidates in the LMC.

To fully understand the post-AGB/RGB population in the Magellanic Clouds and to provide a better sample of post-AGB/RGB stars whose properties can be compared to models, a larger sample of these objects is definitely required. We have therefore carried out an extensive search for post-AGB/RGB stars in the SMC, to complement the survey of van Aarle et al. (2011) in the LMC. In this paper, we present the results of our survey of

[1] According to observational studies in the Magellanic Clouds (e.g. Frogel, Cohen & Persson 1983; Cioni et al. 1999; Wood et al. 1999) and evolutionary tracks of Bertelli et al. (2008) corresponding to LMC and SMC metallicities, the bolometric luminosity of the RGB tip is found to be close to $M_{\rm bol} - 3.6$ mag.

post-AGB/RGB stars in the SMC. This includes a low-resolution optical spectral survey of the post-AGB candidates.[2]

The structure of this paper is as follows: in Section 2, we present the selection criteria used to obtain an initial sample of post-AGB/RGB candidates in the SMC. We also present the photometric data, covering the UV, optical and IR wavelengths and use it to compute the SEDs for all the sources in our sample. Optical spectra, along with the data reduction procedure and a preliminary spectral classification, are presented in Section 3. In Sections 4–6, we describe the method used to estimate the stellar parameters ($T_{\rm eff}$, $\log g$ and [Fe/H]) from the spectra, and the reddening from SED fitting. Subsequently, in Section 7 we present the catalogues of the post-AGB/RGB and YSO candidates. In Sections 8–11, we analyse different characteristics of the two populations by examining the SEDs, the optical spectra and the light curves of the individual candidates. In Section 12, we present the completeness of the survey, and in Section 13, we empirically estimate the evolutionary rates of the transient post-AGB/RGB phase. Finally, we conclude with a summary of our survey.

2 SAMPLE SELECTION, PHOTOMETRIC DATA, EXTINCTION AND INTEGRATED LUMINOSITIES

The successful completion of the large-scale mid-IR *SST* surveys: SAGE for the LMC (Blum et al. 2006; Meixner et al. 2006) and S^{3}MC (Bolatto et al. 2007) and SAGE-SMC (Gordon et al. 2011) for the SMC, provides the opportunity to make a new search for post-AGB/RGB star candidates. Post-AGB/RGB stars are expected to show excess mid-IR flux, and can therefore be identified in the SMC using S^{3}MC and SAGE-SMC. These surveys cover the IRAC (3.6, 4.5, 5.8 and 8 μm) and the MIPS (24.0, 70.0 and 160.0 μm) bands. The *Spitzer* sources have been merged with the Two Micron All Sky Survey (2MASS) J, H and K bands (1.24, 1.66 and 2.16 μm; Skrutskie et al. 2006) in the S^{3}MC and SAGE-SMC catalogues.

In our survey, we used the SAGE-SMC catalogue[3] (including the 2MASS near-IR photometry) along with additional optical and mid-IR photometry. Photometry in the U, V, B and I bands was added from the Magellanic Clouds Photometric Survey (MCPS; Zaritsky et al. 2002). We required the MCPS coordinate to lie within 2 arcsec of the SAGE-SMC coordinate for a match. For those candidates with no I magnitude from the MCPS survey, we searched for an I magnitude in the DENIS (Deep Near-Infrared Survey of the Southern Sky) Catalog (Epchtein 1998). We also added *WISE* photometry in the 3.4, 4.6, 12 and 22 μm bands $W1$, $W2$, $W3$ and $W4$, respectively (Wright et al. 2010).

In the study by van Aarle et al. (2011), they define criteria to select optically visible post-AGB stars in the LMC based on an initial cross-correlation of the *Spitzer* SAGE catalogue with optical catalogues. Their selection criteria require that the sources have an MIPS 24 μm detection and also an optical detection in the U, B, V, R or I filters. They further narrow their sample by applying a colour selection [8]–[24] $>$ 1.384, inspired by what is known from Galactic sources. To reject the obvious intruders such as supergiants and young stellar objects (YSOs), which also have a large mid-IR excess, they impose a luminosity criterion which rejects sources with luminosities less than 1000 $L_\odot$ (thereby rejecting low-mass YSOs) and greater than 35 000 $L_\odot$ (thereby rejecting super giants).

To select candidate post-AGB/RGB stars in the SMC, we used a selection procedure similar to the one used by van Aarle et al. (2011). Our first criterion is that all objects should have $V < 20$, therefore restricting our search to optically visible post-AGB/RGB candidates. We also require that all objects should have a valid 8 μm detection in the SAGE-SMC catalogue as opposed to the MIPS 24 μm detection required for the LMC objects (van Aarle et al. 2011), since the objects in the SMC are fainter than in the LMC.

We further narrowed this sample of objects by selecting those candidates that satisfy any one of the following five selection criteria, which includes a colour criterion and a luminosity criterion. These selection criteria remove extreme AGB stars, red supergiants and low-mass YSOs.

(i) For those candidates that have a 24 μm magnitude, we used the [8]–[24] $>$ 1.384 and 1000 $< L/L_\odot <$ 35 000 criteria which were used in the LMC by van Aarle et al. (2011). We selected 150 objects in this way and gave them a priority 1 when assigning objects for spectroscopic observations.

(ii) To include lower luminosity objects, we also select those candidates that obey the same colour–colour criteria as for the priority 1 objects [item (i)] but with a slightly relaxed luminosity criterion of 500 $< L/L_\odot <$ 35 000. We selected 54 objects in this way and gave them a priority 2 when assigning objects for spectroscopic observations.

(iii) To further relax the previous selection criteria, we also include stars that have [8]–[24] $<$ 1.384 provided [3.6]−[8] $>$ 1 with a luminosity criterion of 500 $< L/L_\odot <$ 35 000. This selection criterion resulted in 71 objects and we gave these objects also a priority 2 when assigning objects for spectroscopic observations.

(iv) Since for majority of the stars in the SMC there is no MIPS 24 μm magnitude, we also select those sources with $I - [3.6] > 1.5$ and $I - [8] > 0.50 + 1.06 \times (I - [3.6])$ (a colour–colour cut which is defined to select objects such as post-AGB/RGB stars which have hot central stars) with a luminosity criterion of 500 $< L/L_\odot <$ 35 000. This selection criterion resulted in 178 objects and we gave them a priority 2 as well when assigning objects for spectroscopic observations.

(v) To increase the sample of objects available to fill the fibres of the multifibre spectrograph (see Section 3), we used the same colour–colour criterion as for the priority 2 objects (items (ii), (iii) and (iv) above) but relaxed the luminosity criterion to 100 $< L/L_\odot <$ 35 000, thereby including lower luminosity objects. This yielded 741 additional objects which were given a priority 3 when assigning objects for spectroscopic observations.

The luminosities for the selected sources were obtained by integrating under the SED defined by the photometry after correcting for the effects of reddening. All objects in the SMC are subjected to some level of reddening. This reddening can be attributed to three possible sources. The first is produced by the interstellar dust in our Galaxy, along the line of sight of the SMC. This extinction is small with an average of $E(B - V) = 0.037$ mag (Schlegel, Finkbeiner & Davis 1998). The second source of reddening is from the SMC itself. Keller & Wood (2006) derived a mean reddening $E(B - V) = 0.12$ mag for the combined SMC and Galactic components. The final source of reddening for the central stars in

[2] We have also carried out a low-resolution optical spectroscopic examination for the sample of the LMC post-AGB candidates identified by van Aarle et al. (2011). The results will be presented in a following publication (Kamath et al., in preparation).

[3] By 2010, S^{3}MC had been superseded by SAGE-SMC, so we did not use the former.

each object is the circumstellar dust envelope. The circumstellar reddening for each individual star differs, but it can be estimated from spectroscopic observations (see Section 5).

For all the candidates in the sample, the photometry was corrected for foreground (SMC plus Galactic) extinction corresponding to $E(B-V) = 0.12$ and Rv = 3.1 using the extinction law of Cardelli, Clayton & Mathis (1989). A luminosity for each candidate was obtained by integrating the SED that is defined by the photometry corrected for foreground SMC extinction. The integration was not extended beyond the longest wavelength point in the flux distribution. Therefore, in objects where the flux is still rising at the longest wavelength of observation, the estimated luminosity will be a lower limit since large amounts of flux will be missing. The circumstellar extinction was not corrected for because it was assumed that all radiation absorbed by the circumstellar matter was re-radiated at a longer mid-IR wavelength still within the wavelength range of the observed SED. The observed luminosity ($L_{\rm obs}/L_{\odot}$) of each candidate was then obtained by applying a distance modulus for the SMC of 18.93 (Keller & Wood 2006).

At this stage, we were left with a total of 1194 objects within which we expect to find post-AGB/RGB candidates. The positions of the 1194 objects are marked on the $I-[8]$ versus $I-[3.6]$ colour–colour plot in Fig. 1. We represent the priority 1 objects with red filled circles, the priority 2 objects with blue filled squares and the priority 3 objects with green filled triangles. We note in passing that we also selected a group of 352 probable Be star candidates for future study (represented with cyan crosses in Fig. 1). These Be star candidates will not be discussed in this paper but will be examined in a following publication.

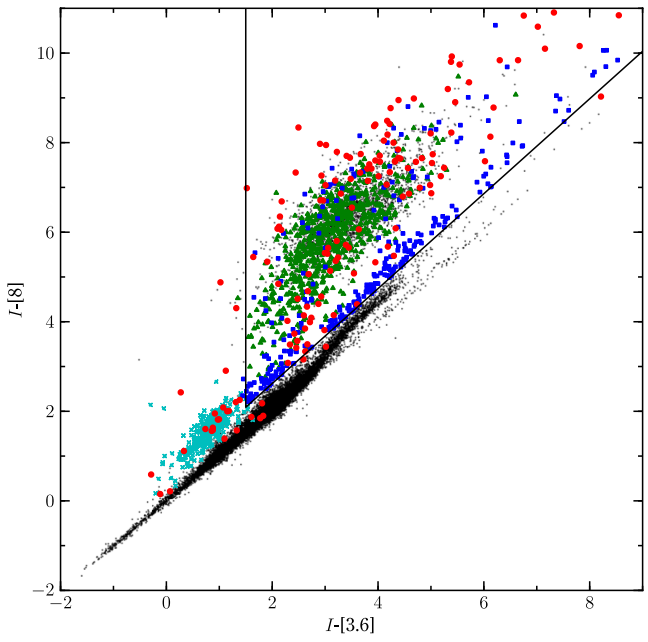

Figure 1. The colour–colour plot of $I-[8]$ versus $I-[3.6]$. The small black dots in the background represent the entire field SMC population with a valid [8] magnitude from the SAGE-SMC catalogue. The red filled circles represent the 150 priority 1 candidates. The blue filled squares represent the 303 priority 2 objects and the green filled squares represent the 741 priority 3 objects. The region within the black solid lines defines our selection criterion in this plane. The black dots in this region fail the luminosity or V magnitude selection criteria. The cyan crosses near $(I-[3.6], I-[8]) = (1, 1.5)$ represent the probable Be star population. We note that some of our selected objects fall outside the boundaries of this region as these are sources with an MIPS [24] magnitude and were selected using the colour criteria used for selecting sources with MIPS [24] magnitudes. See the text for further details.

In Table 1, we provide photometric magnitudes for the five candidates from the selected sample. Column (22) of Table 1 gives the observed luminosity of the candidates. We also estimate an effective temperature, ($T_{\rm eff,\,SED}$) presented in Column (23) of Table 1, by fitting ATLAS9 atmosphere models (Castelli & Kurucz 2003) to the B, V, I and J bands corrected for foreground extinction. However, since the photometry has not been corrected for circumstellar reddening, this estimate of photometric $T_{\rm eff}$ can only serve as a rough estimate. We determine the true $T_{\rm eff}$, as well as other stellar parameters, from the spectra of the candidates (see Section 4). The full table which contains the photometry of the 1194 candidates is available as online Supporting Information.

3 SPECTROSCOPIC OBSERVATIONS

We have conducted a low-resolution optical spectroscopic survey of our SMC post-AGB/RGB candidates. The spectra were taken using the AAOmega double-beam multifibre spectrograph (Sharp et al. 2006) mounted on the 3.9 m Anglo Australian Telescope (AAT) at Siding Spring Observatory. AAOmega allows for the simultaneous observation of 392 targets (including science objects, sky-positions and fiducial guide stars) over a 2° field using the 2dF fibre positioner (Lewis et al. 2002). The fibres are of 2 arcsec projected diameter. Within each configuration there is a minimum target separation of ∼30 arcsec imposed by the physical size of the fibres (Miszalski et al. 2006). The positional information for our targets was taken from the 2MASS Point Source Catalogue (Skrutskie et al. 2006) which has an accuracy of ∼ 0.1 arcsec. The fibre allocations were done automatically using the AAOmega specific CONFIGURE program (Miszalski et al. 2006) which ensures the optimal allocation of fibres in terms of maximizing the number of objects observed. 30 fibres were assigned to random positions in the sky to sample the background sky spectrum. About 5–8 fibres were allocated to guide stars. Excluding the defective fibres, the remaining fibres were assigned science targets. Altogether, four overlapping 2° diameter fields were chosen to cover the survey region of the SMC. The field centres of the SMC observations in our survey are given in Table 2 and shown in Fig. 2. A Ne–Ar arc and a quartz lamp flat-field exposure were taken per field for calibration. We used the 580V grating with a central wavelength of 4800 Å, and the 385R grating with a central wavelength of 7250 Å. This combination provides a maximum spectral coverage of 3700–8800 Å at a resolution of 1300.

The AAOmega raw data were reduced using a combination of the AAOmega-2dFDR reduction pipeline[4] supplied and maintained by the Anglo-Australian Observatory and IRAF[5] routines. Prior to reduction with 2dFDR, bad pixel columns were identified and repaired. We then used 2dFDR to perform a bias subtraction, cosmic ray rejection, flat-field, throughput calibration and sky subtraction on the data. For each CCD, the final co-addition of science frames was carried out after excluding any single exposures with very low flux relative to the other frames. The 2dFDR splicing routine was used to join the red and blue arms. As a consequence of the splicing,

[4] http://www.aao.gov.au/AAO/2df/aaomega/aaomega_software.html

[5] IRAF is distributed by the National Optical Astronomy Observatory, which is operated by the Association of Universities for Research in Astronomy (AURA) under cooperative agreement with the National Science Foundation.

Table 1. Photometric data. Optical photometry (*U*, *V*, *B* and *I* bands) is from MCPS, with the *I* band from the DENIS Catalog if the MCPS has no *I* magnitude. *J*, *H* and *K* photometry is from 2MASS. Mid-IR photometry is from the *SST* survey SAGE-SMC in the IRAC (3.6, 4.5, 5.8 and 8 μm) and the MIPS (24.0, 72.0 and 160 μm) bands, and from WISE in the 3.4, 4.6, 12 and 22 μm bands (*W*1, *W*2, *W*3 and *W*4). The full table is available as online Supporting Information.

Object name	RA (°)	Dec. (°)	*U*	*B*	*V*	*I*	*J*	*H*	*K*	*W*1	[3.6]	[4.5]	*W*2	[5.8]	[8.0]	*W*3	*W*4	[24]	[70]	[160]	$L_{obs}/L_{\odot}$	$T_{eff,\,SED}$ (K)
J002417.12-734932.2	6.071 333	−73.825 611	99.999	20.444	19.432	18.357	17.525	16.951	16.168	99.999	15.836	15.697	99.999	14.2	12.703	99.999	99.999	99.999	99.999	99.999	101	4500
J002420.34-733611.2	6.084 75	−73.603 111	99.999	21.888	17.621	14.667	13.177	12.001	11.078	99.999	9.608	9.129	99.999	8.671	8.356	99.999	99.999	8.228	99.999	99.999	8141	3500
J002439.95-734016.8	6.166 458	−73.671 333	19.693	20.213	19.387	18.407	16.464	15.898	15.024	99.999	14.788	14.231	99.999	12.922	11.613	99.999	99.999	8.342	99.999	99.999	272	4750
J002521.94-735519.8	6.341 417	−73.922 167	20.401	20.712	19.964	18.359	17.417	16.644	16.167	99.999	15.652	15.128	99.999	13.798	12.468	99.999	99.999	8.926	99.999	99.999	139	4750
J002546.36-740328.2	6.443 167	−74.057 833	99.999	20.783	19.696	18.625	17.004	16.31	15.869	99.999	15.305	14.737	99.999	14.421	11.593	99.999	99.999	8.906	99.999	99.999	177	4000

Note. The object name is the SAGE name. The RA and Dec. coordinates are given for the J2000 epoch. Null magnitudes are listed as 99.999. $L_{obs}/L_{\odot}$ is the observed luminosity and $T_{eff,\,SED}$ (K) is the photometric temperature (see the text for details).

Table 2. The field centres of the SMC observations in our survey and the corresponding exposure times.

Field	RA (2000)	Dec. (2000)	Exposure
SMC1	01 00 00.00	−72 06 00.0	4 × 900 s
SMC2	00 48 00.00	−73 36 00.0	4 × 900 s
SMC3	01 07 12.00	−73 36 00.0	3 × 900 s
SMC4	00 39 36.00	−72 24 00.0	4 × 900 s

Figure 2. A Digitalised Sky Survey (DSS) image of a 5° field of view centred on the SMC. The four circles represent the observed 2° fields of the SMC that were covered in our survey.

for most of the objects, a slight artificial slope difference was introduced in the blue spectra with respect to the red spectra. The spectra were therefore continuum normalized before spectral analysis (see Section 4). At the end of the data reduction procedure, a multifits file containing the spectra for all the objects observed in each field was produced.

To remove the telluric absorption lines imprinted on the spectra, we performed a telluric line removal. For each field, we constructed an individual telluric spectrum by averaging around 5–10 spectra of hot stars. All the stellar spectral features were manually removed from the telluric spectrum. Telluric line removal was then performed with this artificial telluric spectrum using the IRAF task TELLURIC.

We obtained a total of 1060 spectra. Not all the 1194 candidates could be observed since some were out of the fields observed and some objects were too close spatially for fibre assignments to be done simultaneously. Furthermore, owing to the overlap in the observed fields, some of the target sources were observed multiple times. For such sources, we either averaged the multiple observations or rejected the observations with low signal-to-noise ratio, retaining only the spectrum with a higher signal to noise. In the end, we were left with spectra of 801 unique candidates from the initial selected sample of 1194. For these 801 candidates, we found that a small fraction of their spectra were affected by sinusoidal continuum variations attributed to the fringing patterns exhibited by specific fibres. This fringing is caused by a gap between the front end of the fibres and their refractors. The fringing is not

stable, resulting in unstable spectra (Sharp, Brough & Cannon 2013). A total of 18 spectra with severe fringing were discarded, leaving 783 candidates. We also found that for 162 objects their spectra had low signal with less than 200 counts. We discarded these objects. At this stage we were left with a good spectra of 621 individual objects.

3.1 Preliminary spectral classification

Since our colour and luminosity criteria are not very restrictive, it is very likely that the selected sample of post-AGB/RGB candidates is contaminated by objects with similar IR colours. Of the 621 candidates for which we have spectra, the intermingled contaminants include M stars, C stars, PNe, red shifted galaxies, quasi-stellar objects (QSOs) and YSOs which have $L_{\rm obs}/L_{\odot} > 100$.

We performed a preliminary spectral analysis, by eye, to categorize the remaining spectra into bins based on the nature of the spectra. We found 20 M-stars identified based on the presence of strong molecular absorption features of titanium oxide (TiO) and vanadium oxide (VO) (e.g. Kirkpatrick et al. 1999). We identified 140 C-stars characterized by the presence of key molecules such as C_2, CN and CH (see Wallerstein & Knapp 1998, for a review on C stars). A group of 204 background galaxies and 36 QSOs were identified by their large redshifts and the width of the emission lines of hydrogen and ionic lines (e.g. Field 1973; Vanden Berk et al. 2001). Based on the presence of an emission-line spectrum characterized by recombination lines of hydrogen and helium as well as various collisionally excited forbidden lines of heavier elements such as O, N, C, Ne and Ar, we were able to identify 46 PNe (see Frew & Parker 2010, for further details on identifying PNe). Nine stars in our sample were identified to be stars with TiO bands in emission. These objects are discussed in Wood, Kamath & Van Winckel (2013) and are not considered further here.

The sample of M-stars, C-stars and the PNe is presented in Appendix B. The sample of background galaxies and QSOs will be discussed in a following publication.

Of the remaining sample of 166 objects, we expect to find not just post-AGB/RGB candidates but also luminous massive YSOs. In general, the spectra of luminous massive YSOs are similar to those of post-AGB/RGB stars. However, owing to that fact that the post-AGB/RGB candidates have different masses (and hence surface gravities) from the luminous YSO candidates, one way to separate them is by carrying out a detailed spectral analysis to estimate their surface gravities.

We found that 63 of the remaining 166 objects had prominent emission lines mostly along with a strong UV continuum. These two features are characteristic of both hot post-AGB/RGB objects as well as YSOs. Hot post-AGB/RGB stars are likely to have an emission-line spectrum characterized by weak recombination lines of hydrogen and helium and various collisionally excited forbidden lines of heavier elements (e.g. Van Winckel 2003). The spectra of YSO candidates are likely to show a broad Hα line profile owing to the disc accretion in YSOs (Jayawardhana, Mohanty & Basri 2002; Natta et al. 2002). Furthermore the YSO objects show a flared SED peaking at longer wavelengths (mostly $>100\,\mu$m). Therefore, we classify these 63 objects as probable hot post-AGB/RGB or YSO candidates. We do not carry out any further photospheric analysis on these objects, owing to their spectra being completely dominated by emission lines. The properties of these objects are presented in Appendix A. Table A1 contains a list of all the objects along with their $L_{\rm obs}$, the emission lines seen, previous identifications of the objects as well as the most probable nature of the object (hot post-AGB/RGB or YSO). This classification was performed based on a visual inspection of the spectra and SEDs of the candidates resulting in 40 probable hot post-AGB/RGB candidates, 23 probable YSOs. Out of these 23 objects that we classified as YSOs, 6 have been identified previously as YSOs by Oliveira et al. (2013). The spectra and SEDs of these 63 objects are also shown in Appendix A.

The remaining 103 objects are carried forward for detailed spectral analysis, to search for post-AGB/RGB candidates (mostly of A, F, G, K spectral types) and remove the luminous YSO candidates.

Fig. 3 shows all of the 621 sources with good spectra plotted on the colour–colour plot of $I-[8]$ versus $I-[3.6]$ used for our sample selection (see Section 2), with the symbol type showing the type of source, as described above.

3.2 Establishing SMC membership of the probable post-AGB/RGB and YSO candidates

To establish SMC membership of the group of 103 probable post-AGB/RGB and YSO candidates, we derived heliocentric radial velocities using the Fourier cross-correlation technique. For cross-correlation, we used only certain regions of the spectra. The regions used were the calcium IR triplet (CaT) region from 8400 to 8700 Å, the Balmer line region from 3700 to 4000 Å and the Hα region from 6250 to 6450 Å. The cross-correlation was done using the routine FXCOR in IRAF, using as templates three separate individual synthetic spectra that covered the CaT, the Balmer and the Hα regions, respectively. For each object, we estimated three radial velocities resulting from the cross-correlation of the three regions of the spectra with the three templates. Radial velocity errors for each cross-correlation were computed by FXCOR based on the fitted peak height and the antisymmetric noise as described by Tonry & Davis (1979). The adopted heliocentric velocity was chosen to be the one with the minimum radial velocity error. A typical error in the adopted radial velocity is 6 km s^{-1}. We note that in some objects, instead of the CaT absorption lines, there are CaT lines in emission. For such objects, only two regions (Balmer line region and Hα region) were used for cross-correlation. This also applies to stars of an earlier spectral type that have Paschen lines that lie in the CaT region.

Fig. 4 shows the histogram of the heliocentric velocities for the 103 probable post-AGB/RGB and YSO candidates. A Gaussian fit to the histogram results in an average velocity of 165 km s^{-1} and standard deviation of 50 km s^{-1}. The estimated average velocity agrees well the velocity expected for stars in the SMC. In a radial velocity study of red giants in the SMC, De Propris et al. (2010) observe a double peak in the radial velocities of stars, with one component peaking at the classical SMC recession velocity of $\sim$160 km s^{-1} and the second component peaking at a higher velocity of about $\sim$200 km s^{-1}. They also find a low-velocity component at $\sim$106 km s^{-1} in the most distant field of their study (3.9 kpc from the SMC centre). In Fig. 4 the blue dotted lines denote the high- and low-velocity peaks from De Propris et al. (2010). Based on these results and also the shape of the velocity distribution of our sample of stars, we found that all objects lie well within the range of 40–290 km s^{-1} (a 2.5σ deviation from the mean radial velocity), resulting in a sample of 103 possible post-AGB/RGB and YSO candidates with confirmed SMC membership. The blue dashed lines in Fig. 4 denotes the radial velocity interval that we use in our study.

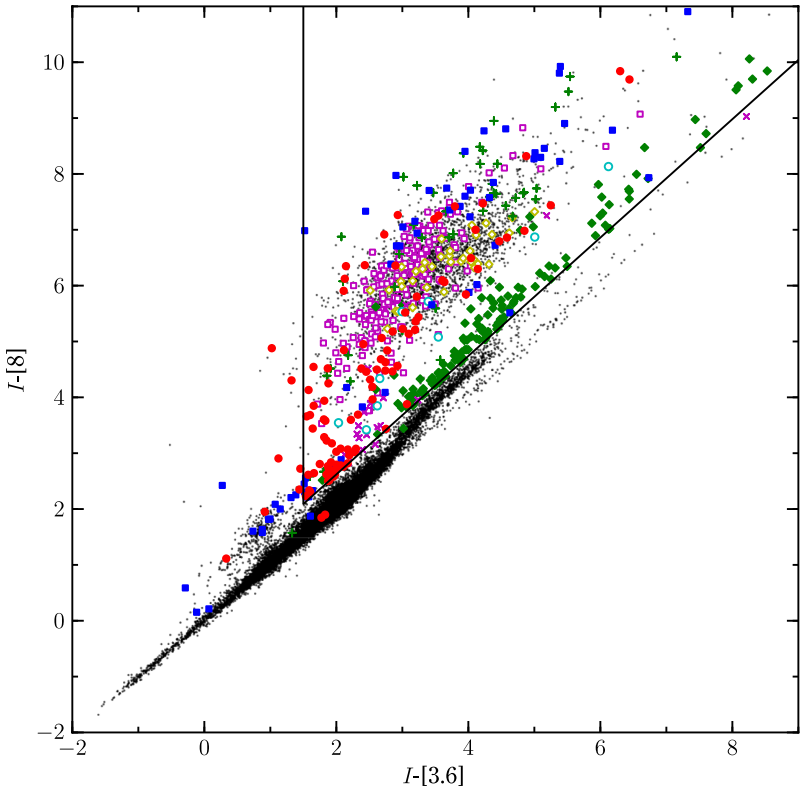

Figure 3. The colour–colour plot of $I-[8]$ versus $I-[3.6]$. The black dots in the background represent the entire field SMC population with a valid 8 μm magnitude from the SAGE-SMC IRAC catalogue. The red filled circles represent the sample of 103 probable post-AGB/RGB and luminous YSO candidates. The blue filled squares represent the sample of 63 objects that have strong emission lines and a significant UV continuum. The cyan open circles represent the nine objects with TiO bands in emission. The green plus symbols represent the PN population. The magenta open squares represent the sample that has been classified as background galaxies. The yellow open diamonds represent the sources identified as QSOs. The green filled diamonds represent the C-stars, and the magenta crosses represent the sources that were classified as M-stars.

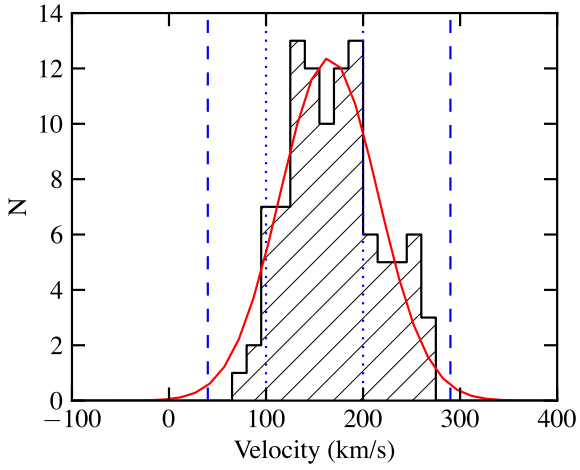

Figure 4. Radial velocity histogram for the group of 103 post-AGB/RGB and YSO candidates. The red curve denotes a Gaussian with a mean of 165 km s^{-1} and a standard deviation of 50 km s^{-1}. The formal standard error in the mean velocity, computed from the individual velocity errors, is 6 km s^{-1}. The blue dotted lines mark the low velocity component (at ∼106 km s^{-1}) and the high-velocity component (at 200 km s^{-1}) observed by De Propris et al. (2010) in the SMC. The blue dashed lines denote the radial velocity interval (defined by a 2.5σ deviation from the mean) used in our study. See the text for further details.

4 SPECTROSCOPIC ANALYSIS

We developed a fully automated spectral typing pipeline (STP) to simultaneously determine the stellar parameters ($T_{\rm eff}$, $\log g$ and [Fe/H]) of the candidates. The STP matches each individual observed spectrum to a library of synthetic templates, and finds the minimum rms deviation over a restricted $T_{\rm eff}$, $\log g$ and [Fe/H] grid.

The synthetic templates were obtained from the Munari synthetic library (Munari et al. 2005) which consists of a grid of nearly 60 000 spectra, based on the local thermodynamical equilibrium (LTE) Kurucz–Castelli atmosphere models (Castelli & Kurucz 2003). For the purpose of our study, we choose the grid characterized by the following ranges of stellar parameters: $3500 \leq T_{\rm eff} \leq 47\,500$ K, $0.0 \leq \log g \leq 5.0$, $-2.5 \leq$ [Fe/H] ≤ 0.5, the microturbulence velocity fixed at 2 km s^{-1}, $V_{\rm rot}$ fixed at 0 km s^{-1} and a scaled solar composition. The STP is designed for normalized spectra (to avoid the effects of reddening) of low resolution ($R = 1300$) and with a wavelength range of 3700–8800 Å. The synthetic templates used within the STP are convolved to match the resolution of the observed spectra.

The spectra of our selected objects are often affected by significant amounts of reddening. This, coupled with inherent systematic difficulties in the flux calibration of AAOmega spectra, makes the overall continuum slope unreliable for estimating the $T_{\rm eff}$, and we restrict the use of the slope to only a small interval $\lambda < 4000$ Å.

The Balmer lines and slope of the continuum in the region <4000 Åprovide an excellent $T_{\rm eff}$ diagnostic for cool stars due to

their virtually nil gravity dependence (Gray 1992; Heiter et al. 2002). So for those stars with photometric temperatures (see Section 2) cooler than 8000 K, we make use of the slope of the continuum region <4000 Å. For these spectra, the normalization was carried out by splitting each spectrum into two parts: the region blueward of 4000 Åand the region beyond 4000 Å. For the region ≤4000 Å, we simply divided the spectral flux by the value at 4000 Å. For region of spectrum beyond 4000 Å, we normalized as usual using a low-order polynomial fit. The two regions were then joined back together. For stars with effective temperatures >8000 K, we performed a standard continuum normalization using the IRAF task CONTINUUM. Finally, the spectra of all the candidates were corrected to zero radial velocity using the IRAF task DOPCOR. The normalized and shifted spectra were then used to derive the stellar parameters. The templates were also normalized based on their temperatures, using the same normalization procedure as used for the observed spectra.

For each individual spectrum, the STP performs a grid search over a restricted $T_{\rm eff}$ range initially centred at the photometric temperature of the candidate.[6] The $\log g$ values for models are constrained to lie between the theoretical values of $\log g$ expected for a star in the post-AGB/RGB phase and a star in the pre-main-sequence (PMS) phase. To derive the $\log g$, the star would have in the post-AGB phase, the mass of the post-AGB star is derived using the observed luminosity and the luminosity–core mass relation (Wood & Zarro 1981) for AGB stars (candidates with $L/\,{\rm L}_{\odot} > 2500$ are assumed to be post-AGB stars). For the post-RGB stars ($L/\,{\rm L}_{\odot} \leq 2500$), a similar procedure is used but using a luminosity–core mass relation derived from a fit to the evolutionary tracks of Bertelli et al. (2008) with $Z = 0.004$. We note that for post-AGB/RGB stars, the stellar mass is essentially the core mass of the progenitor AGB/RGB star. Using the mass, the observed luminosity and the photometric temperature, the theoretical $\log g$, is calculated. Similarly, using the PISA PMS evolutionary tracks (Tognelli, Prada Moroni & Degl'Innocenti 2011) for $Z = 0.004$ (and an extrapolation to higher masses since the maximum mass of the PISA tracks is 7 $\rm M_{\odot}$), we can estimate the theoretical value of $\log g$ a star would have on a PMS evolutionary track at the observed luminosity and photometric $T_{\rm eff}$. We find that for a star of a given luminosity and $T_{\rm eff}$, the value of $\log g$ differs by a factor of ∼1.3 between the post-AGB/RGB stars and the PMS stars of K–G spectral types.

The restricted grid search reduces computational time and also reduces the occurrence of degeneracies between stellar parameters. No restriction is placed on [Fe/H]. Before the spectral matching is carried out, each synthetic template is shifted in velocity to that of the observed spectrum by cross-correlating the template with the observed spectrum. The template is then resampled at the observed wavelength points. For each grid point in the $T_{\rm eff}$, $\log g$ and [Fe/H] space, the rms deviation between the template and the observed spectrum is calculated as described below. The minimum of the rms deviation gives the best-fitting $T_{\rm eff}$, $\log g$ and [Fe/H].

Specific spectral regions are sensitive to specific stellar parameters. Our rms calculations preferentially weight specific spectral regions to help break the degeneracy that often plagues automated spectral classification algorithms. We use weights w_1, w_2 and w_3 such that

$$\mathrm{RMS} = \mathrm{RMS}_{\rm wide} + w_1 \cdot \mathrm{RMS}_{T_{\rm eff}} + w_2 \cdot \mathrm{RMS}_{\log g} + w_3 \cdot \mathrm{RMS}_{\rm [Fe/H]}\,, \quad (1)$$

where the weights were determined by trial and error such that the spectral typing results are consistent with that of previously classified targets, and visual classification of selected targets ($w_1 = 70$, $w_2 = 60$, $w_3 = 40$).

For those objects whose spectra show the presence of CaT absorption lines or Paschen lines in absorption, $\mathrm{RMS}_{\rm wide}$ is calculated from the full spectrum, omitting the Hα region at 6500–6650 Å since the Hα line at 6563 Å is predominantly in emission and it is dominated by non-LTE effects. For those objects whose spectra do not show CaT or Paschen lines or if these lines are in emission, then we consider only the region from 3700 to 6000 Åwhen calculating $\mathrm{RMS}_{\rm wide}$.

$\mathrm{RMS}_{T_{\rm eff}}$, $\mathrm{RMS}_{\log g}$, $\mathrm{RMS}_{\rm [Fe/H]}$ are calculated using the $T_{\rm eff}$, $\log g$ and [Fe/H] sensitive spectral regions (see below), respectively. The weighted spectral regions we choose, differ for targets with different $T_{\rm eff}$ estimates. They are listed in Table 3. For example, the Mg b lines near 5170 Å are indicators of $\log g$ for stars with $T_{\rm eff} \sim 5000$ K, while the CaT region from 8400 to 8700 Å serves as a better $\log g$ indicator for stars with $T_{\rm eff} \sim 6500$ K.

Since our spectral resolution is low, the only preferentially weighted spectral region that can be used when calculating $\mathrm{RMS}_{\rm [Fe/H]}$ is the CaT region with the CaT lines in absorption, as they serve as good metallicity indicators. Therefore, for those stars whose spectra do not contain CaT absorption lines (this includes all stars with $T_{\rm eff} > 8000$ K) [Fe/H] is fixed to −1.0 as we have no [Fe/H] sensitive regions defined and $w_3 = 0$ in these cases.

To estimate the best $T_{\rm eff}$, $\log g$ and [Fe/H] value, the STP performs a local quadratic interpolation of the rms deviation in a $3 \times 3 \times 3$ grid in $T_{\rm eff}$, $\log g$ and [Fe/H] space. At the borders of the parameter space, or in the case of missing grid points, we reduce the dimensions of the interpolation accordingly. The entire process is performed iteratively by feeding the estimated best-fitting $T_{\rm eff}$ value of the previous iteration to the new iteration. This is done for a maximum of 20 iterations or until the best-fitting model does not change on successive iterations.

As an example, the fitting result for a candidate (J004441.04-732136.4) is shown in Fig. 5. The plot presents the inverse rms distribution (goodness of fit) in the $T_{\rm eff}$–$\log g$ space and the $T_{\rm eff}$– [Fe/H] space, with the interpolated final values marked. The preferentially weighted spectral regions used during the spectral typing process are plotted and important spectral features are also indicated. Depending on the strength of the spectral features, lines such as the Ba II line at 4554.03 Å, the Ba II line at 6496.89 Å and the Ba I line at 6498.76 Åcan be detected. These are indicators of *s*-process enrichment and are marked on each plot for the identification of the sources in which we can identify *s*-process enrichment. Similarly, Li I lines at 6707.77 and 6707.92 Å are also marked for identification of Li in the candidates (although the two lines are unresolved at the resolution of our spectra and their position is indicated by a single blue dashed vertical line in Fig. 5.)

The 103 objects that were fed into the STP had their $T_{\rm eff}$, $\log g$ and [Fe/H] derived. We obtained 63 post-AGB/RGB candidates and 40 YSO candidates (see Section 7). The estimated $T_{\rm eff}$, $\log g$ and [Fe/H] for our final sample of high-probability post-AGB/RGB and YSO candidates are listed in Tables 4–7. Furthermore, the post-AGB/RGB and YSO candidates have been grouped into quality one (Q1) and quality two (Q2) (see Section 7), giving the four

[6] We note that the photometric $T_{\rm eff}$ does not skew the final estimated $T_{\rm eff}$ in any way. In fact, we find that for stars with large reddening, the estimated $T_{\rm eff}$ by the STP is larger than the photometric $T_{\rm eff}$ and for stars with small reddening the photometric $T_{\rm eff}$ and the estimated $T_{\rm eff}$ are similar, as expected.

Table 3. The preferentially weighted spectral regions. $\lambda_{\rm Teff}$ and $\lambda_{\log g}$ indicate the regions sensitive to $T_{\rm eff}$ and $\log g$, respectively, as a function of the $T_{\rm eff}$ estimate. For stars with CaT lines in absorption and $\lambda_{\rm [Fe/H]}$ is the CaT region from 8450 to 8700 Å. For stars without CaT absorption lines, their spectra have no [Fe/H] sensitive regions defined ($w3 = 0$) and [Fe/H] $= -1$ is assumed. See the text for more details.

$T_{\rm eff}$	All spectra $\lambda_{\rm Teff}$ (Å)	Spectra with CaT absorption lines $\lambda_{\log g}$ (Å)	Spectra without CaT absorption lines $\lambda_{\log g}$ (Å)
<4300 K	3750–4000	4720–4970	4270–4970
4300–5000 K	3750–4000	5100–5200	5100–5200
5000–6500 K	3750–4000,4240–4340	4240–4340,5100–5200	4240–4340,5100–5200
6500–8000 K	3750–4000	8350–8800	3750–3950
8000–15 000 K	3750–6000		3750–3950
15 000–30 000 K	4000–4050,4300–4500		4000–4050,4300–4500
>30 000 K	4000–4050,4300–4500,5610–5830		4000–4050,4300–4500

tables. The spectra of the 103 final objects are shown in Appendix C (Figs C5–C8) and Tables C1–C4 list their spectral features. Plots similar to Fig. 5 for the final sample of high-probability post-AGB/RGB and YSO candidates are available as online Supporting Information.

4.1 Estimating the error of the spectral typing routine

As a first check of uncertainty in our spectral typing method, we identified the stars in our sample that had been previously examined using high-resolution spectra. In the SMC, so far, a detailed chemical analysis has been carried out on only one of our stars J004441.04-732136.4 (De Smedt et al. 2012). A comparison of our derived stellar parameters to those of De Smedt et al. (2012), who obtained high-resolution optical UVES spectra, resulted in $\Delta T_{\rm eff}$= 82 K, $\Delta \log g = 0.5$, Δ[Fe/H] = 0.27 dex. High-resolution chemical analysis studies have been carried out for two LMC stars (van Aarle et al. 2013) in our LMC sample (Kamath et al., in preparation). Comparing the stellar parameters that we derived for the two stars (J053250.69-713925.8 and J053253.51-695915.1) to the values estimated from the high-resolution chemical abundance study, we find that for J053250.69-713925.8, $\Delta T_{\rm eff}$= 394K, $\Delta \log g = 0$ and Δ[Fe/H] = 0.23 and for J053253.51-695915.1, $\Delta T_{\rm eff}$= 57K, $\Delta \log g = 1.0$ and Δ[Fe/H] = 0.07 dex. Thus, the mean rms difference between our measurements and the literature values are $\Delta T_{\rm eff}$= 135K, $\Delta \log g = 0.37$ and Δ[Fe/H] = 0.12 dex.

The low-resolution optical AAOmega spectra have a range of signal from 100 to 3000 counts. To test the reliability of our STP as a function of signal, we took a set of synthetic spectra varying in temperatures from 3500 to 9500 K (the $T_{\rm eff}$ region over which we expect most of the post-AGB/RGB and YSO candidates to lie), in $\log g$ from 0.5 to 1.5, with fixed [Fe/H] $= -1.0$. We added to the synthetic spectra AAOmega detector read noise and varying levels of photon noise, resulting in artificial spectra with quality equivalent to measured spectra of 100, 500, 1500 and 3000 counts. The artificial spectra were then passed through the STP. Table 8 shows the mean errors in the measurements of $T_{\rm eff}$, $\log g$ and [Fe/H] as a function of counts. From this error estimation exercise and comparison with high-resolution studies, we conclude that the mean errors in our derived parameters are smaller than the grid spacings of the synthetic template spectra: 250 K in $T_{\rm eff}$, 0.5 in $\log g$ and 0.5 in [Fe/H].

5 REDDENING ESTIMATES

The total reddening, which includes both the interstellar and circumstellar reddening, can be determined by estimating the difference between the intrinsic colour of the candidate (derived from the $T_{\rm eff}$ estimated from the spectrum) and the measured colour (derived from the raw photometry). We calculated the $E(B-V)$ for each individual candidate by estimating the value of $E(B-V)$ that minimized the sum of the squared differences between the dereddened observed and the intrinsic B, V, I and J magnitudes (at longer wavelengths, emission from dust can contribute to the observed magnitudes). We used the Cardelli et al. (1989) extinction law, assuming Rv = 3.1. It is possible that the circumstellar extinction law is different from the interstellar extinction law but we have not explored this possibility. The derived $E(B-V)$ values were used to correct the observed magnitudes for extinction. Then the *BVIJ* fluxes of the best-fitting model atmosphere (derived from the STP) were normalized to the corrected *BVIJ* fluxes.

Typically, the uncertainty in the $E(B-V)$ estimate is dominated by the errors in the derived $T_{\rm eff}$ values. The uncertainty in the $E(B-V)$ estimate owing to other errors, such as errors in the photometry, are small. Given that the uncertainty in the estimated $T_{\rm eff}$ could be up to $\pm$ 250 K, we estimated the maximum error in $E(B-V)$ to be the difference between $E(B-V)$ at the estimated $T_{\rm eff}$, and at $T_{\rm eff}$ values of $\pm$ 250. The error $\Delta E(B-V) \approx 0.2$ mag at $T_{\rm eff} \sim$ 4000 K and declines with increasing $T_{\rm eff}$ to $\Delta E(B-V) \approx 0.1$ mag at $T_{\rm eff} \sim 5000$ K and $\Delta E(B-V) \approx 0.05$ mag at $T_{\rm eff} \sim 6500$ K

The total $E(B-V)$ estimated for the final sample of post-AGB/RGB and YSO candidates is listed in Tables 4–7. For some stars the estimated $E(B-V)$ was negative which indicates that the $T_{\rm eff}$ estimated from the spectra is likely to be cooler than the actual $T_{\rm eff}$ of the star. For such stars, we estimated the $E(B-V)$ using $T_{\rm eff}$ values increased by 250 and 500 K. These stars are denoted using a suffix 'b' and 'c', respectively, in Tables 4–7. The SEDs, both as observed and de-extincted, are plotted in Appendix C, Figs C1–C4.

6 LUMINOSITY OF THE CENTRAL STAR

For post-AGB/RGB stars and YSOs the central star is surrounded by circumstellar dust that is not necessarily spherically symmetric. For such cases, the observed luminosity $L_{\rm obs}$ could either be overestimated or underestimated. For this reason, it is essential to estimate the photospheric luminosity of the central star $L_{\rm phot}$. This photospheric luminosity can be derived from the bolometric correction for the model atmosphere corresponding to each individual candidate normalized to the de-extincted V magnitude, coupled with the distance modulus to the SMC. In Tables 4–7, we list the photospheric luminosities ($L_{\rm phot}$) for the central star of the post-AGB/RGB and YSO candidates.

For some of our objects we encounter an energy problem as the available luminosity $L_{\rm phot}$ from the central star is too small to

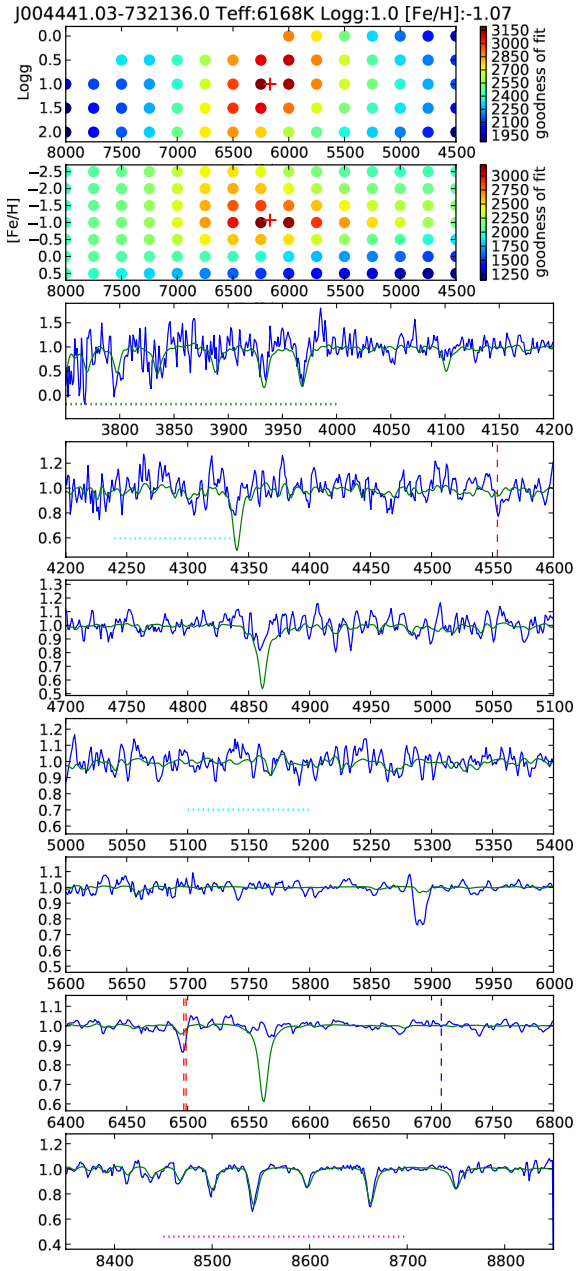

Figure 5. Spectral typing result for J004441.04-732136.4. The first two subplots show the inverse rms distribution (goodness of fit) in the $T_{\rm eff}$–$\log g$ space and $T_{\rm eff}$–[Fe/H] space with a red plus representing the final interpolated value. In the remaining subplots, the observed spectrum is shown in blue, whilst the green line represents the best-fitting synthetic spectrum. The green, cyan and pink dotted horizontal dotted lines represents the preferentially weighted $T_{\rm eff}$, $\log g$ and [Fe/H] regions (see the text for details). The blue dashed vertical line marks the position of the Li I lines. The single red dashed marks the position of the Ba II line at 4554.03 Åand the double red dashed lines mark the positions of the Ba II line at 6496.89 Å, and the Ba I line at 6498.76 Å.

account for the luminosity $L_{\rm obs}$ derived by integrating the total SED thus resulting in $L_{\rm obs}$ being ∼1.5–5 times $L_{\rm phot}$. It is possible that if scattered light dominates in the optical part of the spectrum, the reddening as well as the luminosity estimate $L_{\rm phot}$ are not correct and the luminosity $L_{\rm obs}$ could be a better tracer of the total luminosity of the object. Models by Men'shchikov et al. (2002) show that $L_{\rm obs}$ can be several times $L_{\rm phot}$ which is consistent with the luminosity ratios we obtain for some objects. Another possibility is that there is another independent object coincident on the sky with the optically observed star.

7 SEPARATING THE POST-AGB/RGB AND YSO CANDIDATES

Disentangling the post-AGB/RGB candidates from the YSO candidates is a concern since these unrelated objects lie in the same region of the HR diagram. One of the ways to distinguish between these objects is to use the derived $\log g$ values from the spectral fit for the individual objects. As mentioned in Section 4, the $\log g$ values that a star would have in the post-AGB/RGB phase and in the PMS phase differ by ∼1.3; hence, we separated the post-AGB/RGB candidates from the YSO candidates by comparing the individual derived $\log g$ values from the spectral fitting to the theoretical value of $\log g$ a star would have in the post-AGB/RGB phase and in the PMS phase. Based on this separation scheme, we formed the final sample which consisted of 63 post-AGB/RGB candidates and 40 YSO candidates.

We note that in determining the stellar parameters such as $T_{\rm eff}$, $\log g$ and [Fe/H], the $\log g$ estimates have the highest uncertainty since the $\log g$ value least affects the spectra when compared to the $T_{\rm eff}$ and [Fe/H]. Therefore, despite the criteria used to separate the post-AGB/RGB candidates from the YSOs, there remains a degree of uncertainty in our classification method. Detailed studies based on high-resolution spectra are needed to confirm the nature of the individual objects.

The 63 post-AGB/RGB and 40 YSO candidates were then further classified into two groups: Q1 (quality 1) and Q2 (quality 2) based on the signal of the observed spectrum and also a visual inspection of the results of the spectral typing routine. We classified those candidates with a relatively high signal and a good spectral matching fit as Q1 and the remaining candidates were classified as Q2 candidates. Therefore, our final sample of 63 post-AGB/RGB candidates were split into 2 groups of 38 Q1 and 25 Q2 objects. Similarly, the final sample of 40 YSO candidates were split into 2 groups consisting of 27 Q1 and 13 Q2 objects.

In Tables 4 and 5, we list the final sample of post-AGB/RGB candidates, along with their stellar parameters and their SED classification (see Section 8). We also make the distinction between post-AGB and post-RGB candidates using a luminosity criterion based on the expected luminosity of the RGB-tip for stars in the LMC and SMC (see Section 1). We consider post-AGB stars to be those objects with $L_{\rm phot}/{\rm L}_{\odot} > 2500$ and post-RGB stars to be those objects with $L_{\rm phot}/{\rm L}_{\odot} \leq 2500$. We find that our sample consists of 42 post-RGB candidates and 21 post-AGB candidates.

Similarly, in Tables 6 and 7 we present the final sample of YSO candidates.

Since post-AGB/RGB stars are an old to intermediate-age population, we expect them to be more metal poor than the YSOs which belong to the young SMC population, which has a mean metallicity of [Fe/H] $\simeq -0.7$ (Luck et al. 1998). Fig. 6 shows the [Fe/H] distribution for the post-AGB/RGB candidates (represented by the red histogram) and YSO candidates (represented by the blue histogram).[7] From Gaussian fits to the histograms (Fig. 6), we find that the post-AGB/RGB sample peaks at a [Fe/H] $= -1.14$ with

[7] Note. The post-AGB/RGB and YSO candidates for which we imposed an [Fe/H] value of −1.00 (see Tables 4–7) have not been considered while plotting the [Fe/H] distribution.

Table 4. The observational and stellar parameters for the Q1 post-AGB/RGB candidates.

#	Name	$T_{\rm eff}$ (K)	log g	[Fe/H]	$E(B-V)$	($L_{\rm obs}$/L$_\odot$)	($L_{\rm phot}$/L$_\odot$)	Type	RV (km s^{-1})	M/M$_\odot$	SED	Catalogue
					Candidates with [Fe/H] estimates from spectra							
1	J003441.01-732908.0^c	4485	0.50	−1.66	0.00	337	226	p-RGB	162.1 ± 6.2	0.32	Disc	–
2	J003643.94-723722.1	7458	0.50	−0.63	0.48	3699	8495	p-AGB	195.8 ± 7.4	0.64	Shell	–
3	J003829.99-730334.1	5080	0.48	−1.03	0.18	3919	4361	p-RGB	152.5 ± 2.0	0.57	Uncertain	RSG[1]
4	J003908.89-724314.9	5099	1.00	−0.79	0.23	562	684	p-RGB	164.7 ± 6.7	0.38	Uncertain	–
5	J003941.74-714708.5^b	4147	0.00	−1.24	0.12	1778	1633	p-RGB	155.6 ± 1.7	0.43	Uncertain	–
6	J004050.18-733226.6	5706	1.05	−1.31	0.12	885	894	p-RGB	149.9 ± 2.9	0.39	Uncertain	–
7	J004114.10-741130.1	5722	0.50	−1.04	0.96	3924	12 000	p-AGB	172.5 ± 5.0	0.70	Shell	FIR[1]
8	J004441.03-732136.0	6168	1.00	−1.07	0.82	4504	12 729	p-AGB	167.1 ± 5.5	0.71	Shell	RGB[1], p-AGB[2], [21] [3]
9	J004906.52-733136.1	5068	1.00	−1.25	0.15	411	452	p-RGB	107.5 ± 6.0	0.35	Disc	–
10	J004909.72-724745.4	6271	0.50	−0.86	0.83	2882	7641	p-AGB	203.0 ± 4.7	0.62	Uncertain	aO-AGB[1]
11	J004944.15-725209.0	5787	0.50	−1.09	0.70	912	2834	p-AGB	129.4 ± 3.0	0.54	Uncertain	–
12	J005107.19-734133.3^c	5767	0.72	−1.56	0.09	3465	1773	p-RGB	187.5 ± 4.3	0.43	Disc	x-AGB[1]
13	J005159.04-734214.4	4240	0.66	−1.01	0.20	1915	2163	p-RGB	142.4 ± 2.5	0.44	Uncertain	RGB[1]
14	J005252.87-722842.9	7651	1.39	−1.97	0.02	8093	7338	p-AGB	252.7 ± 10.6	0.62	Uncertain	–
15	J005307.35-734404.5^b	4134	0.00	−1.04	0.11	1545	1472	p-RGB	177.8 ± 2.6	0.42	Uncertain	RGB[1]
16	J005310.08-722921.0	4941	0.23	−1.05	0.20	7740	8456	p-AGB	112.5 ± 1.5	0.64	Uncertain	RSG[1]
17	J005803.08-732245.1	6348	0.50	−1.03	1.12	4633	11 868	p-AGB	182.0 ± 5.6	0.70	Shell	FIR[1]
18	J005914.20-723327.1	5002	0.50	−1.48	0.06	939	886	p-RGB	125.3 ± 3.2	0.39	Uncertain	–
19	J010056.93-715551.3^b	4295	0.00	−0.85	0.12	10 767	9908	p-AGB	130.7 ± 1.6	0.66	Uncertain	RSG[1]
20	J010247.72-740151.6^c	4762	0.00	−1.39	0.09	1211	1247	p-RGB	164.3 ± 2.0	0.41	Uncertain	–
21	J010333.93-724405.1^c	4621	0.00	−0.89	0.10	14 969	10 327	p-AGB	190.6 ± 1.7	0.67	Disc	O-AGB[1]
22	J011219.69-735125.9	6716	0.99	−1.11	0.03	12 334	3819	p-AGB	274.2 ± 7.7	0.56	Disc	x-AGB[1], EmO[4, 5]
23	J011222.88-715820.4^b	4691	0.00	−1.04	0.04	1445	1085	p-RGB	131.0 ± 5.3	0.40	Disc	–
					Candidates with assumed [Fe/H] = −1.00							
24	J004534.36-734811.8	5493	0.50	−1.00	0.25	700	787	p-RGB	137.5 ± 4.7	0.38	Disc	–
25	J004456.21-732256.6	13 931	2.50	−1.00	0.22	5173	22 243	p-AGB	97.9 ± 20.1	0.87	Uncertain	FIR[1], Em*[4, 5]
26	J004614.67-723519	8313	1.00	−1.00	0.08	1105	555	p-RGB	202.5 ± 13.9	0.36	Shell	–
27	J004629.29-731552.3	7640	1.00	−1.00	1.07	855	1679	p-RGB	108.0 ± 15.0	0.43	Disc	–
28	J004644.05-735944.7	16 910	3.00	−1.00	0.64	967	4742	p-AGB	254.5 ± 14.9	0.58	Shell	–
29	J004854.24-735651.9	5353	1.00	−1.00	0.08	331	223	p-RGB	127.0 ± 7.1	0.32	Disc	–
30	J005104.61-722058.5	5652	1.50	−1.00	0.40	346	542	p-RGB	164.1 ± 4.2	0.36	Disc	–
31	J005113.04-722227.0	5795	1.00	−1.00	0.17	311	327	p-RGB	48.5 ± 20.5	0.34	Disc	–
32	J005136.79-722818.0	10 615	2.00	−1.00	0.08	3026	5180	p-AGB	224.1 ± 8.8	0.58	Uncertain	–
33	J005310.47-732800.4	5240	0.50	−1.00	0.39	744	1160	p-RGB	112.5 ± 1.5	0.40	Uncertain	–
34	J005327.75-733339.6	7653	1.50	−1.00	1.17	149	854	p-RGB	239.0 ± 15.8	0.39	Disc	–
35	J005506.24-731347.6	11 000	2.50	−1.00	0.10	1814	3212	p-AGB	252.6 ± 11.6	0.55	Uncertain	RGB[1], Em[4]
36	J005553.75-720859.7	8268	1.00	−1.00	0.06	17 601	16 025	p-AGB	152.3 ± 5.5	0.77	Disc	RSG[1], Em*[4, 5]
37	J005908.99-710648.6	5410	0.00	−1.00	0.56	3178	8165	p-AGB	204.8 ± 8.8	0.63	Disc	–
38	J010342.34-721342.7	8265	1.00	−1.00	0.13	14 521	10 944	p-AGB	176.0 ± 4.9	0.68	Disc	x-AGB[1], C*[4]

Notes. ($L_{\rm obs}$/L$_\odot$) is the observed luminosity corrected for foreground extinction, ($L_{\rm phot}$/L$_\odot$) is the photospheric luminosity of the central star, Type is the estimated evolutionary status (p-RGB for a post-RGB star, p-AGB for a post-AGB star), M/M$_\odot$ is the derived mass of the post-AGB/RGB candidate (see Section 4). The superscripts '^{b}', '^{c}' and '^{d}' represent the methods used to estimate the $E(B-V)$ value. See the text for further details.
A positional matching was found with the following catalogues: [1]Boyer et al. (2011), [2]De Smedt et al. (2012), [3]Volk et al. (2011), [4]Meyssonnier & Azzopardi (1993), [5]Murphy & Bessell (2000). The results of the matching are listed in the last column. Catalogue identifications: C* – Carbon star; Em*, EmO – object with emission features; p-AGB – post-AGB star, [21] – 21 μm source. The following objects are defined in Boyer et al. (2011): RGB – red giant branch star, RSG – red supergiant, FIR – far-IR object, x-AGB – dusty AGB star with superwind mass-loss, aO-AGB – anomalous O-rich AGB star, O-AGB – O-rich AGB, C-AGB – C-rich AGB. Throughout this contribution, positional cross-matching was performed with the following catalogues: De Smedt et al. (2012), Volk et al. (2011), Oliveira et al. (2013), Bonanos et al. (2009), Groenewegen (2000), Loup et al. (1997), Trams et al. (1999), Kontizas et al. (2001), Lagadec et al. (2007), van Loon et al. (2010), Sanduleak (1978), Jacoby (1980), Jacoby & De Marco (2002), Morgan & Good (1985), Morgan (1995), Sanduleak & Pesch (1981), Meyssonnier & Azzopardi (1993), Murphy & Bessell (2000), Wilke et al. (2003)(12μm), Wilke et al. (2003)(25μm), Wilke et al. (2003)(60μm), Wilke et al. (2003)(100μm), Wilke et al. (2003)(170μm), Boyer et al. (2011), Simon et al. (2007).

a standard deviation of 0.20, whilst the YSO sample, peaks at a higher metallicity of [Fe/H] = −0.62 with a standard deviation of 0.18. Using the two-sided Kolmogorov–Smirnov test, we find that the post-AGB/RGB candidates are more metal poor than the YSOs with high confidence (probability of the two samples to be drawn from the same distribution $P \sim 10^{-4}$). The existence of this bimodal metallicity distribution supports our separation of post-AGB/RGB from the YSO candidates.

8 CLASSIFICATION OF SEDS

Post-AGB/RGB and YSO candidates consists of two components: the central star and the circumstellar environment associated with the central star.

In single optically visible post-AGB stars, there exists a circumstellar shell which corresponds to an optically thin expanding circumstellar envelope that is the remnant AGB mass-loss. The

Table 5. The observational and stellar parameters for the Q2 post-AGB/RGB candidates.

#	Name	$T_{\rm eff}$ (K)	log g	[Fe/H]	$E(B-V)$	($L_{\rm obs}$/L$_\odot$)	($L_{\rm phot}$/L$_\odot$)	Type	RV (km s^{-1})	M/M$_\odot$	SED	Catalogue
Candidates with [Fe/H] estimates from spectra												
39	J003611.06-730447	5392	0.50	−1.50	0.26	497	617	p-RGB	126.6 ± 9.4	0.37	Disc	–
40	J003818.36-731120.7	5150	1.48	−1.76	0.48	277	261	p-RGB	120.3 ± 12.4	0.32	Disc	–
41	J003946.58-730433.5[b]	4500	0.49	−1.10	0.04	670	588	p-RGB	141.0 ± 2.5	0.37	Uncertain	–
42	J004215.31-740219.1[c]	4827	0.50	−0.81	0.06	414	348	p-RGB	99.7 ± 4.5	0.34	Disc	–
43	J004431.23-730549.3[c]	4509	0.00	−1.49	0.10	1268	1250	p-RGB	151.5 ± 1.4	0.41	Uncertain	–
44	J005222.19-733537.6	4176	0.57	−1.03	0.09	967	949	p-RGB	187.0 ± 2.4	0.39	Uncertain	–
45	J005311.41-740621.2	4209	0.00	−0.58	0.89	3974	3861	p-AGB	215.3 ± 3.5	0.56	Disc	C-AGB[1]
46	J005447.59-740121.4[c]	4342	0.00	−0.90	0.13	1732	1510	p-RGB	133.3 ± 3.7	0.42	Uncertain	FIR[1]
47	J005515.71-712516.9	4695	1.33	−1.13	0.22	811	992	p-RGB	129.3 ± 4.0	0.40	Uncertain	–
48	J005526.37-723248.7	5136	0.84	−1.23	0.26	851	1064	p-RGB	136.8 ± 3.0	0.40	Uncertain	–
49	J005658.04-735059.7	5169	0.50	−1.36	0.30	384	536	p-RGB	135.6 ± 4.7	0.36	Uncertain	RGB[1]
50	J005925.13-741309.6	3951	0.00	−1.14	0.10	3167	3006	p-AGB	135.5 ± 2.6	0.55	Uncertain	aO-AGB[1]
51	J005941.66-742842.9	4983	1.50	−2.21	0.13	282	259	p-RGB	198.8 ± 14.2	0.33	Disc	–
52	J010021.78-730901.3	4834	0.00	−1.32	0.32	1067	954	p-RGB	174.7 ± 3.4	0.39	Disc	–
53	J010049.88-723459.7[c]	4564	0.00	−1.30	0.16	1174	1164	p-RGB	151.0 ± 2.4	0.41	Uncertain	–
54	J010254.90-722120.9[b]	4111	0.00	−1.08	0.04	1632	1114	p-RGB	116.6 ± 2.7	0.40	Disc	–
55	J010304.72-721245.3[c]	4578	0.62	−1.10	0.12	766	796	p-RGB	151.1 ± 3.3	0.38	Uncertain	RGB[1]
56	J010310.25-730602.7	5812	1.51	−0.65	0.18	493	540	p-RGB	221.6 ± 4.0	0.36	Disc	–
57	J010404.07-723521.5	5519	0.50	−1.00	0.50	751	1530	p-RGB	156.0 ± 1.9	0.42	Uncertain	RGB[1]
58	J010549.25-725028.9	5490	0.00	−1.31	0.44	1359	1620	p-RGB	191.1 ± 2.1	0.42	Disc	–
59	J010623.71-724413.5	4178	0.00	−0.79	0.11	1962	1291	p-RGB	193.9 ± 2.0	0.41	Disc	–
60	J010814.67-721306.2	6340	0.50	−0.63	1.14	1200	4707	p-AGB	157.0 ± 7.4	0.57	Disc	–
61	J011133.41-733300.6[b]	4444	0.00	−1.17	0.13	910	914	p-RGB	149.9 ± 2.3	0.39	Uncertain	–
62	J011149.89-720822.4	4366	0.00	−1.17	0.03	788	625	p-RGB	157.1 ± 4.4	0.37	Uncertain	–
Candidates with assumed [Fe/H] = −1.00												
63	J003549.26-740737.9	8250	1.00	−1.00	0.17	799	564	p-RGB	223.8 ± 10.1	0.36	Disc	–

Notes. As for Table 4. A positional matching was found with the following catalogues: [1]Boyer et al. (2011). Catalogue identifications: The following objects are defined in Boyer et al. (2011): RGB – red giant branch star, FIR – far-IR object, aO-AGB – anomalous O-rich AGB star, C-AGB – C-rich AGB.

shell continues to move outwards, gradually exposing the central star. This results in a double-peaked SED with one peak due to the stellar emission and the other due to circumstellar dust (Van Winckel 2003) which peaks greater than 10 μm (as shown from radiative transfer models of a well-known expanding shell source HD 161796, where the peak of the dust SED is at around 30 μm, see Min et al. 2013, for details). These objects are considered to be shell sources.

Some post-AGB/RGB stars have SEDs with a strong near-IR emission, indicating the presence of hot dust in the system. Some of the these stars have been found to reside in binary systems which have a stable circumbinary disc (Waters, Trams & Waelkens 1992; de Ruyter et al. 2006; Van Winckel 2007; Gielen et al. 2008; Van Winckel et al. 2009). It is assumed that all objects with such an SED have a circumbinary disc. A general characteristic of these sources is that the dust energy distribution peaks at relatively high temperatures and the peak of the dust SED lies around 10 μm and in some cases even bluer (de Ruyter et al. 2006; Gielen et al. 2011).

Based on a visual inspection of the position of the peak of the dust excess in the SEDs, for majority of the sources, we were able to identify whether the SEDs were representative of a shell or disc source.

To confirm whether these objects are indeed likely shell or disc sources, we used the J-[3.6] colour to check the presence of a near-IR excess due to hot dust surrounding the central star. This is indicative of a stable dust structure as these objects have photospheres too hot to be in a dust producing phase. We plot the post-AGB/RGB candidates on a J-[3.6] versus [3.6]–[8] colour–colour plot in the left-hand panel of Fig. 10. The cyan/grey symbols represent the post-RGB candidates and the red symbols represent the post-AGB candidates. We find that majority of the post-AGB/RGB candidates (27 sources in total) that we identified as disc sources based on the visual inspection of their SEDs, lie in the region $1.6 < [3.6]–[8] < 3.0$ of the J-[3.6] versus [3.6]–[8] colour–colour plot. These sources appear to have redder J-[3.6] colours, mostly with J-[3.6] ≥ 1.0, which is indicative of hot dust in the system. Therefore, we classify these 27 objects to be likely disc sources. In Fig. 10, we represent these disc sources with open circles. The two black solid lines mark the region where $1.6 \leq [3.6]–[8] \leq 3.0$.

We find that a small group of six post-AGB/RGB candidates that we identified to be shell sources based on the visual inspection of their SEDs, have a [3.6]–[8] excess with [3.6]–[8] > 3.0 which indicates cool dust in the system. The SEDs of these objects show a very strong double peaked feature indicating a detached cool dust shell surrounding the central star. Therefore, we classify these six objects to be likely shell sources. In Fig. 10, we represent these shell sources with filled circles. We find that all these sources show detections at 24 μm. We note that sources with a 24 μm detection are enclosed within an open square symbol in Fig. 10.

These classifications, 'disc' or 'shell', are given in the SED column of Tables 4 and 5.

The remaining 30 post-AGB/RGB candidates are found to lie in the region [3.6]–[8] < 1.6. Majority of these objects show a mild J-[3.6] excess with $0.8 < J$-[3.6] < 1.3, which indicates hot dust surrounding the central star, characteristic of disc sources. Based on the visual inspection of their SEDs, we were able to identify a few of these sources as likely shells or discs; however, for majority of these sources, such an identification was not possible since we

Table 6. The observational and stellar parameters for the Q1 YSO candidates.

#	Name	$T_{\rm eff}$ (K)	log g	[Fe/H]	$E(B-V)$	$(L_{\rm obs}/L_{\odot})$	$(L_{\rm phot}/L_{\odot})$	RV (km s^{-1})	Catalogue
				Candidates with [Fe/H] estimates from spectra					
1	J004927.26-724738.4	7596	2.46	−1.22	0.11	2175	2126	248.3 ± 9.7	RGB[1]
2	J004949.43-731327.3	5303	2.13	−0.61	0.37	761	1360	182.5 ± 2.4	RGB[1]
3	J010134.91-720605.4	5162	2.00	−0.81	0.24	1988	2572	193.1 ± 1.6	–
4	J010222.29-724502.6	5460	2.50	−0.97	0.27	842	1242	189.2 ± 3.7	RGB[1]
5	J010648.26-734305.4	7020	2.50	−0.16	0.10	2950	2860	248.1 ± 5.9	–
6	J011316.84-733130.9	4500	2.00	−0.56	0.18	762	854	161.8 ± 2.5	RGB[1]
				Candidates with assumed [Fe/H] = −1.00					
7	J003640.64-740747.2	5901	3.00	−1.0	0.50	401	794	208.1 ± 9.6	–
8	J004208.74-733108.4	16 000	3.36	−1.00	0.57	2327	6205	191.0 ± 16.3	IRAS60[2]
9	J004221.85-732417.5	7627	3.00	−1.00	0.38	1336	2813	198.4 ± 8.0	–
10	J004301.63-732050.9	7338	3.50	−1.00	0.12	400	238	189.9 ± 12.7	–
11	J004451.87-725733.6	7625	2.50	−1.00	1.14	6027	1193	273.9 ± 30.3	FIR[1], YSO[3], IRAS60[4, 5]
12	J004501.19-723321.0	7631	3.00	−1.00	0.15	846	966	274.0 ± 18.5	–
13	J004503.51-731627.4	7625	2.50	−1.00	0.31	3417	479	83.7 ± 15.0	FIR[1], IRAS25[6]
14	J004657.45-731143.4	6674	3.00	−1.00	0.39	613	335	149.1 ± 6.0	–
15	J004831.82-720535.7	7540	4.00	−1.00	0.12	129	75	144.8 ± 11.1	–
16	J004840.55-730101.3	6310	2.50	−1.00	0.01	2129	1651	153.7 ± 13.8	Ce*[7]
17	J004905.36-721959.9	5042	2.50	−0.50	0.41	867	1398	116.6 ± 2.8	RGB[1]
18	J004950.02-734011.5	5407	2.50	−1.00	0.04	757	692	65.1 ± 3.5	–
19	J005101.48-733100.4	7639	3.00	−1.00	1.11	1568	10 101	102.9 ± 2.0	–
20	J005112.29-722552.7	5481	2.00	−1.00	0.61	1080	2495	176.5 ± 3.0	o-AGB[1]
21	J005159.81-723511.1	7633	3.00	−1.00	0.00	993	783	182.9 ± 10.1	–
22	J005318.28-733528.7	7643	2.98	−1.00	0.12	356	325	116.6 ± 17.7	–
23	J005606.53-724722.7	6733	2.50	−1.00	0.20	2616	527	89.8 ± 9.3	YSO[3],Em*[7]
24	J005934.21-733025.2	7628	3.50	−1.00	0.64	197	501	184.2 ± 15.5	RGB[1]
25	J010242.25-720306.0	5797	3.00	−1.00	0.32	303	440	210.6 ± 7.4	–
26	J010309.59-715354.2	7661	3.00	−1.00	0.48	2428	2199	232.3 ± 20.0	FIR[1]
27	J010427.62-721037.0	7638	3.50	−1.00	0.20	464	334	204.1 ± 6.6	–

Notes. As for Table 4. A positional matching was found with the following catalogues: [1]Boyer et al. (2011), [2]Wilke et al. (2003) (60 μm), [3]Oliveira et al. (2013), [4]Loup et al. (1997), [5]van Loon et al. (2010), [6]Wilke et al. (2003) (25 μm), [7]Meyssonnier & Azzopardi (1993). Catalogue identifications: Ce* – Cepheid variable; Em* – object with emission features; IRAS25 – *IRAS* source at 25 μm; IRAS60 – *IRAS* source at 60 μm; Y*O – Young stellar object; RGB – red giant branch star; o-AGB – O-rich AGB; FIR – Far-IR object (defined in Boyer et al. 2011).

Table 7. The observational and stellar parameters for the Q2 YSO candidates.

#	Name	$T_{\rm eff}$ (K)	log g	[Fe/H]	$E(B-V)$	$(L_{\rm obs}/L_{\odot})$	$(L_{\rm phot}/L_{\odot})$	RV (km s^{-1})	Catalogue
				Candidates with [Fe/H] estimates from spectra					
28	J004423.32-733343.5	5928	0.25	−0.12	0.57	574	1422	182.7 ± 4.3	–
29	J004830.67-735428.0[b]	4643	3.00	−1.55	0.08	310	275	123.6 ± 10.2	
30	J004853.37-714952.5	4191	1.50	−0.68	0.06	736	655	150.3 ± 2.2	RGB[1]
31	J005143.07-721700.7	5288	2.50	−0.29	0.47	695	1140	189.6 ± 3.7	–
32	J005800.62-721439.8	5160	2.50	−0.54	0.32	598	854	134.1 ± 3.0	–
33	J010051.48-710844.9	5062	2.50	−0.60	0.10	929	932	117.5 ± 2.9	RGB[1]
34	J010441.50-734021.5	5919	2.44	−0.64	0.60	229	484	174.9 ± 4.1	–
				Candidates with assumed [Fe/H] = −1.00					
35	J004547.50-735331.7	6847	3.50	−1.00	0.12	177	81	224.1.0 ± 13.0	–
36	J004707.49-730259.2	6250	3.00	−1.00	0.51	744	463	179.1 ± 14.6	-
37	J010634.50-721505.0	7650	3.00	−1.00	0.17	907	986	234.3 ± 16.5	Em*[2]
38	J011109.79-714226.9	7634	2.85	−1.00	1.19	196	1008	231.3 ± 27.7	–
39	J011229.23-724511.6	7633	3.00	−1.00	0.12	1311	226	242.7 ± 22.9	–
40	J011302.68-724852.5	7532	3.00	−1.00	0.19	823	521	105.3 ± 17.1	–

Notes. As for Table 4. A positional matching was found with the following catalogues: [1]Boyer et al. (2011), [2]Meyssonnier & Azzopardi (1993). Catalogue identifications: Em* – object with emission features; RGB – red giant branch star.

do not have enough information beyond 10 μm for most of these sources. Studies at longer wavelengths to extend these SEDs will be needed to study the temperature distributions of the dust. Therefore, we classify these 30 sources as uncertain. In Fig. 10, we represent these 30 uncertain sources with cross symbols. We find that the majority of these objects are post-RGB stars which are believed to be formed as a result of the termination of RGB evolution by binary interaction, and hence, we expect these objects to have dusty

Table 8. Error estimates in $T_{\rm eff}$, $\log g$ and [Fe/H] as a function of the number of counts in the spectra.

Counts	$\Delta T_{\rm eff}$	$\Delta \log g$	Δ[Fe/H]
100	157	0.47	0.16
500	104	0.20	0.09
1500	52	0.15	0.05
3000	59	0.15	0.06

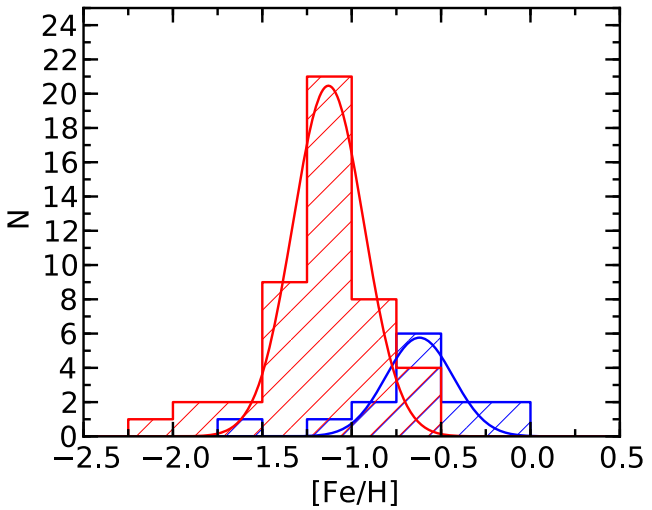

Figure 6. Histograms showing the [Fe/H] distribution for the post-AGB/RGB and YSO candidates in the sample. The red histogram corresponds to the post-AGB/RGB objects, and blue to the YSOs. The red and blue curves denote individual Gaussian fits to the histograms for the post-AGB/RGB and YSO candidates, respectively. See the text for further details.

discs. These objects are labelled as 'uncertain' in the SED column of Tables 4 and 5. Figs 7–9 show examples of post-RGB/AGB candidates that we classified as discs, shells and uncertain.

We conclude that out of the 63 post-AGB/RGB candidates, 27 are disc sources, 6 are shell sources and 30 are uncertain. As expected, majority of the sources classified as discs are post-RGB candidates and majority of the sources classified as shells are post-AGB candidates. In Tables 4 and 5, we list the nature of the SEDs (shell, disc or uncertain) for the Q1 and Q2 post-AGB/RGB candidates, respectively.

In the right-hand panel of Fig. 10, we also plot the YSO candidates (as blue filled circles) though the classification scheme for YSOs are different compared to that of post-AGB/RGB candidates. Sources with a 24 μm detection are enclosed within an open square symbol. For our YSO candidates, their SEDs are limited to 8 μm in most cases and an SED-based YSO classification is beyond the scope of this study.

Typically, YSOs in their early stages of evolution are bright at 70 μm while for evolved YSOs, the peak of the SED is bluer than 70 μm except when the disc is strongly flared. We inspected the individual 70 μm MIPS images (Rieke et al. 2004) of all the Q1 and Q2 YSO candidates. We looked for point source detections as well as evidence for resolved ISM dust-emission coming from star-forming regions. We find that 10 of the 40 YSO candidates (Q1 candidates: J004208.74-733108.4, J004451.87-725733.6, J004503.51-731627.4, J004657.45-731143.4, J004301.63-732050.9, J005606.53-724722.7; Q2 candidates: J004547.50-735331.7, J004707.49-730259.2, J011229.23-724511.6 and J011302.68-724852.5) show a detection in the 70 μm MIPS images. The SEDs of these objects are representative of a strongly flared disc (see Figs C3, C4 in Appendix C). The majority of the 70 μm images for the remaining YSO candidates show emission from dusty resolved nebulosity which might be evidence for a star-forming region.

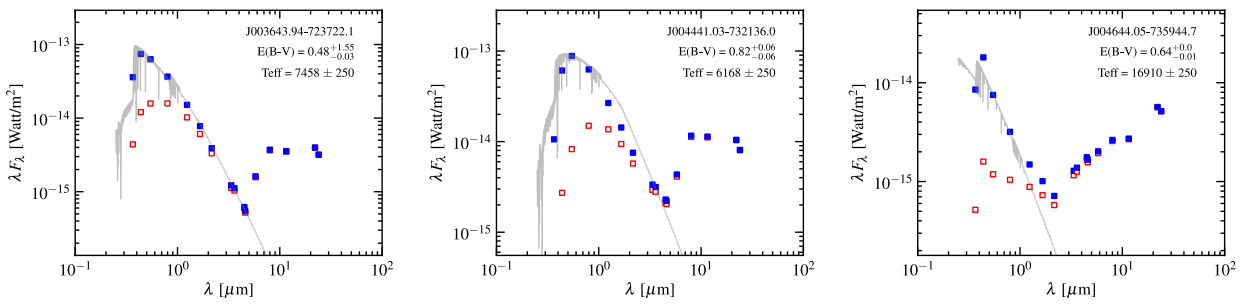

Figure 7. Example SEDs of the post-AGB/RGB candidates classified as shell sources.

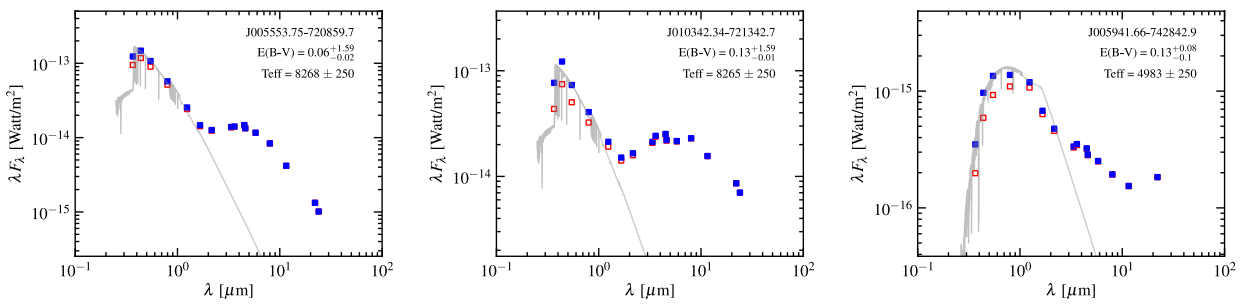

Figure 8. Example SEDs of the post-AGB/RGB candidates classified as disc sources.

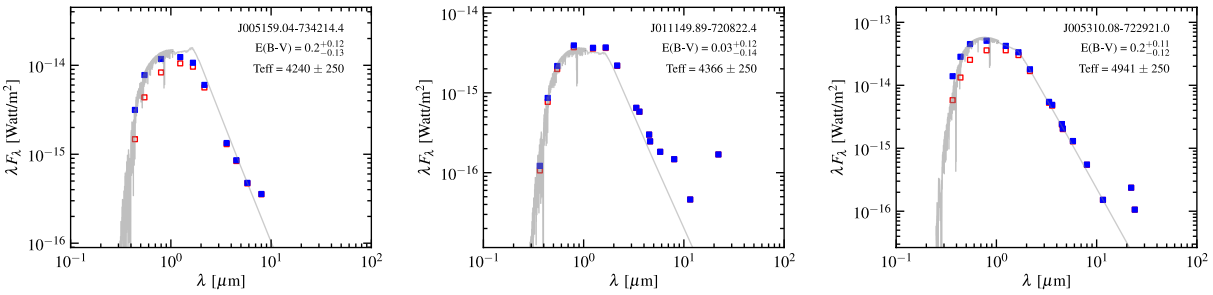

Figure 9. Example SEDs of the post-AGB/RGB candidates that are classified as 'uncertain'.

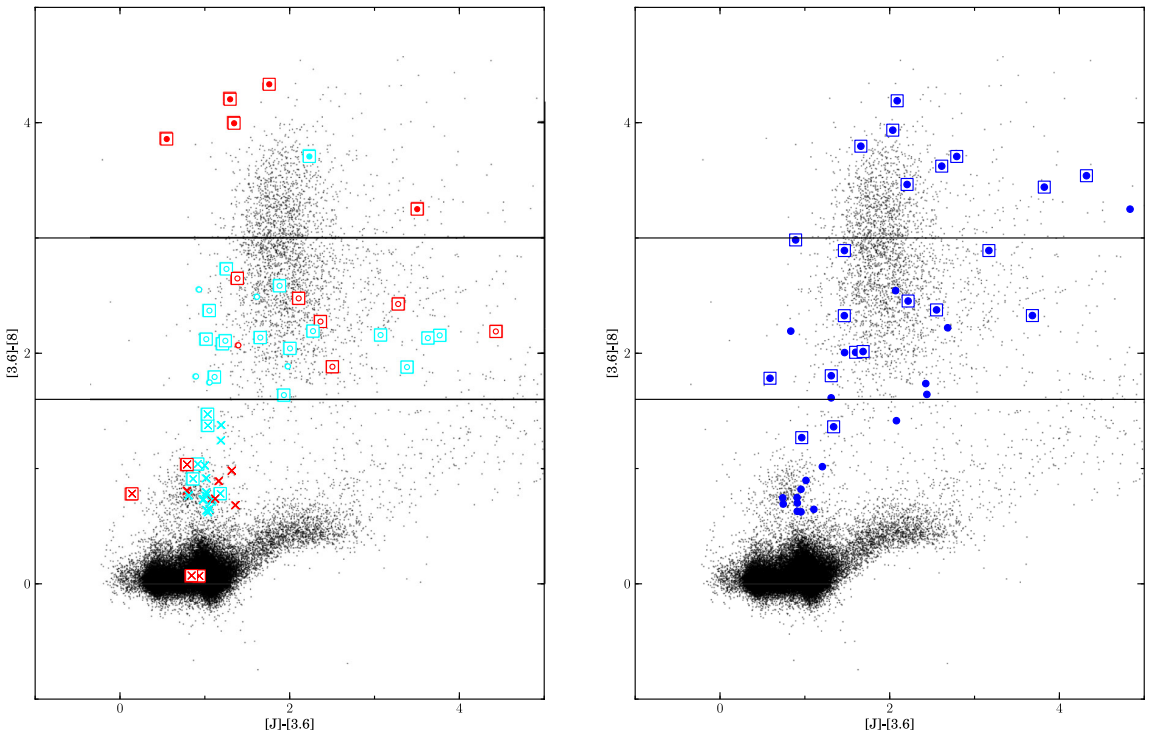

Figure 10. The left-hand panel shows the $J-[3.6]$ versus [3.6]–[8] colour–colour plot for the post-AGB/RGB candidates. The red symbols denote the post-AGB candidates and the cyan symbols denoted the post-RGB candidates. Disc sources are represented as open circles, shells as filled circles and uncertain sources as crosses. Those candidates that show the presence of a [24] μm excess are enclosed in an open square. The region $1.6 < [3.6]–[8] < 3.0$ is where the majority of the post-AGB/RGB discs sources lie. The right-hand panel shows the $J-[3.6]$ versus [3.6]–[8] colour–colour plot for the YSO candidates, represented as blue filled circles. Those candidates that show the presence of a [24] μm excess are enclosed in an open square. The discs source region is transferred from the left-hand panel to the right-hand panel for comparison purposes only.

We note that the presence of a detection at 70 μm or diffuse emission from the local environment does not necessarily confirm the YSO status of the candidates since we find that a few post-AGB/RGB candidates in our sample also appear bright at 70 μm and for some the local environment shows diffuse emission. We find that three (J004614.67-723519.0, J004644.05-735944.7 and J010814.67-721306.2) out of 63 post-AGB/RGB candidates show a detection in the 70 μm MIPS images. The SEDs of J004614.67-723519.0 and J004644.05-735944.7 (see Fig. C1 in Appendix C) represent that of a disc source with a strongly flared disc and therefore they are bright at 70 μm. The SED of J010814.67-721306.2 (see Fig. C2 in Appendix C) represents a shell source with cold circumstellar dust surrounding the central star with emissions at 70 μm. Furthermore, for some sources, including J004441.03-732136.0, the confirmed *s*-process rich post-AGB star (from this study and also from De Smedt et al. 2012), the local environment shows diffuse emission.

Based on the inspection of the 70 μm MIPS images, we conclude that it is likely that early age YSOs show a detection at 70 μm and also most YSOs show a local environment full of diffuse emission characteristic of a star formation region although this criterion is not exclusive to YSOs.

9 FEATURES IN THE STELLAR SPECTRUM

A wealth of information can be obtained from the spectrum of each candidate. In Figs C5–C8 (Appendix C), we show the optical spectra of the sample of Q1 and Q2 post-AGB/RGB and YSO candidates. The individual spectral fits files are available as Supporting Information online. Also, in Appendix C, we have summarized some of the most prominent features observable in the spectra of the final sample of post-AGB/RGB and YSO candidates (Tables C1–C4).

On analysing the spectra of the Q1 and Q2 post-AGB/RGB and YSO candidates we find that, in some cases, the hydrogen lines, the forbidden lines of oxygen ([O III]), sulphur ([S II]), nitrogen ([N II]), the He I lines, the CaT line and the Paschen lines are in emission, indicating either that the star is of an early spectra type capable of exciting circumstellar gas, or that there is unassociated nebulosity in line of sight to the candidate. We also find that in many cases, the lines show the presence of emission cores, indicating the presence of strong stellar winds or inflows or the presence of an accretion disc. Furthermore, among the spectra of the 40 YSO candidates, there are 27 that show a strong Hα emission line. Hα emission and forbidden line emission indicate disc accretion in YSOs (Jayawardhana et al. 2002; Natta et al. 2002).

The presence of enhanced Ba lines in the stellar spectrum indicates an *s*-process enriched post-AGB object. For low-to-intermediate mass stars, a significant amount of *s*-process nucleosynthesis takes place prior to the post-AGB phases of stellar evolution. Therefore, we expect to detect the presence of *s*-process elements. However, chemical analysis studies of a sample of supposed Galactic post-AGB stars show that the abundance pattern in these stars is more diverse than expected (Van Winckel & Reyniers 2000; Reyniers et al. 2007, and references therein), with only some objects showing an enhancement of *s*-process elements, whilst others are either mildly or not enhanced at all. We suggest that the unenhanced Galactic objects could be post-RGB stars as well since the luminosities of our objects clearly shows that post-RGB stars are as common as post-AGB stars.

On visually inspecting the spectra of the post-AGB/RGB candidates, we were unable to identify Barium in the majority of the candidates. This could be due to the low resolution of our spectra. However, for strongly *s*-process enriched stars, we were able to detect the presence of the strong Ba II line at 4554.03 Å. We found that 6 out of 63 stars (J003643.94-723722.1, J004114.10-741130.1, J004441.03-732136.0, J005107.19-734133.3, J005941.66-742842.9 and J010247.72-740151.6) showed the presence of the Ba II line at 4554.03 Å. J004441.03-732136.0 has been previously identified, from abundance studies with high-resolution spectra, as an *s*-process-enriched post-AGB star by De Smedt et al. (2012).

Another element of interest is lithium, which can be detected by the presence of the Li I line at 6708 Å. Lithium is abundant in the parent molecular cloud but it is destroyed in the stellar interior at relatively low temperatures ($\sim 2 \times 10^6$ K). If these interior temperatures are reached when the star is convective, Li will be depleted at the stellar surface during the PMS phase. During the evolution beyond the main sequence, lithium is further decreased owing to the first- and second-dredge-up processes that occur during the red giant phase of evolution and the early-AGB phase of evolution (Karakas & Lattanzio 2003). However, in massive stars (>4 M$_\odot$) during the thermally pulsing AGB phase, lithium can be created by hot bottom burning (Boothroyd, Sackmann & Wasserburg 1995; Lattanzio et al. 1996). We searched for the presence of lithium in the stellar photospheres of both the post-AGB/RGB and YSO candidates by visually inspecting the spectra. We detected the presence of the Li I (6708 Å) line in absorption in 7 out of the 63 post-AGB/RGB candidates. These seven candidates with Li I detections are low-luminosity post-RGB candidates. Current evolutionary models for these mass ranges do not predict an enhanced Li abundance.

We also detected the Li I (6708 Å) line in absorption in 3 of the 40 YSO candidates, indicating that these latter objects are probably early stage YSOs or massive YSOs. We note again that the low resolution of the spectra could possibly affect the number of identifications.

10 HR DIAGRAMS

To understand the evolutionary stage of the post-AGB/RGB and YSO candidates, we show their positions in the HR diagram in Fig. 11. The left-hand panel shows the post-AGB/RGB population. The post-AGB candidates are represented as red symbols and post-RGB candidates are represented as cyan symbols. The open circles represent the disc sources, the filled circles represent the shell sources and the crosses represent those sources classified as uncertain. The right-hand panel shows the YSO population denoted using blue filled circles. We note that the $T_{\rm eff}$ values are those derived from the spectral fitting and the luminosities plotted are the photospheric luminosities ($L_{\rm phot}$).

Each plot shows the main sequence as a cyan cross-hatched region. Evolutionary tracks starting from the main sequence and continuing up to the AGB-tip according to the tracks of Bertelli et al. (2008, 2009) are shown as black solid lines. Note that these tracks use a synthetic AGB calculation adopting unusual mass-loss rates, and almost certainly terminate at too low a luminosity. The plots also show the PISA PMS evolutionary tracks (black dotted lines; Tognelli et al. 2011) up to the maximum computed mass of 7 M$_\odot$. A metallicity $Z = 0.004$ was selected for both sets of evolutionary tracks. The masses of the evolutionary tracks are marked on the plots with the PMS and main-sequence masses marked on the left-hand side of the plots and RGB-tip masses marked on the right-hand side of the plots. The positions of the RGB and AGB are also marked.

In the figure showing the post-AGB/RGB candidates, post-AGB and post-RGB evolutionary tracks are shown schematically (black dashed arrows). The masses for the post-AGB evolutionary tracks are from Vassiliadis & Wood (1994) for $Z = 0.004$. The post-RGB evolutionary track masses are estimated from the RGB luminosity–core mass relation of the Bertelli et al. (2008) tracks with $Z = 0.004$.

In the HR diagram of the post-AGB/RGB candidates, the blue vertical lines show the empirical OGLE instability strip for the Population II Cepheids (Soszynski et al. 2008), since post-AGB/RGB evolutionary tracks cross the Population II Cepheids instability strip. In the HR diagram showing the YSO candidates, the green vertical lines on this plot denotes the Cepheid instability strip from Chiosi, Wood & Capitanio (1993). Also shown in the HR diagram showing the YSO candidates, is the birthline (thick black dashed line in right-hand panel of Fig. 11), which may be considered as the dividing line between the obscured protostellar and observable PMS stage of stellar evolution. The location of the birthline depends highly on the mass accretion rate, with higher accretion rates shifting the line to the right. A mass accretion rate of 10^{-5} M$_\odot$ yr^{-1} (used for the birthline in right-hand panel of Fig. 11) represents the typical value for stars in the mass range from few tenths of a solar mass to about 10 M$_\odot$ (Stahler 1983; Palla & Stahler 1993).

We find that most of the post-AGB/RGB and YSO candidates have $T_{\rm eff} <$ 10 000 K. The HR diagram suggests that the post-AGB/RGB candidates are of $\sim$0.3–0.8 M$_\odot$ and that the post-RGB candidates are mostly disc sources (and therefore inferred to be binaries).

In the case of the YSO candidates, we find that the masses derived from the HR diagram lie in the range $\sim$3–10 M$_\odot$. We also find that the majority of YSOs lie to the right of the birthline so they should not be visibly detectable. This discrepancy may be due to the assumption of symmetric and spherical dust shells in the birthline modelling (with asymmetries, it may be possible to see the central

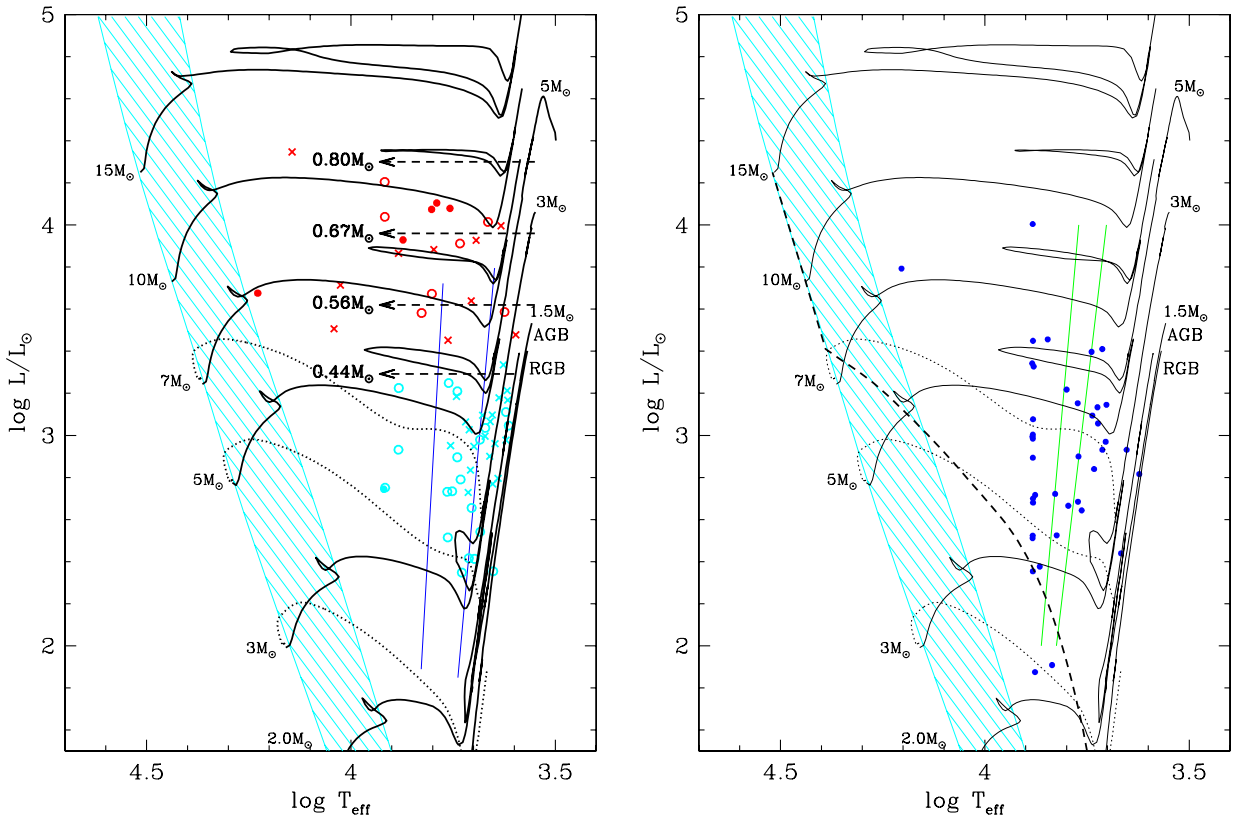

Figure 11. The HR diagram for the sample of the post-AGB/RGB candidates (left-hand panel) and YSO candidates (right-hand panel). In the left-hand panel, the red symbols represent the post-AGB candidates and the cyan symbols represent the post-RGB candidates. The open circles represent disc sources and the filled circles represent the shell sources. The crosses represent those post-AGB/RGB candidates for which the nature of the SED is uncertain. In the right-hand panel, the blue filled circles represent the YSO candidates. Each plot shows the main sequence as a cyan cross-hatched region. In both the plots, the black solid lines represent evolutionary tracks starting from the main sequence and the black dotted lines represent PMS evolutionary tracks. The black dashed arrows on the HR diagram for the post-AGB/RGB candidates schematically represents the post-AGB/RGB evolutionary tracks. Also shown on this plot is the empirical OGLE instability strip for the Population II Cepheids represented with blue vertical lines. In the right-hand panel, the thick black dashed line in right-hand panel is the birthline and the green vertical lines represent the Cepheid instability strip. See the text for further details.

star through a region of low extinction), or too high and assumed accretion rate since the birthline depends on the mass-accretion rates (Palla & Stahler 1993). A low mass accretion rate could move the birthline to lower values of $T_{\rm eff}$ so that our stars could become visible. A group of massive PMS stars similar to the Galactic Herbig AeBe stars was found in the LMC by Lamers, Beaulieu & de Wit (1999), and these are also located above the traditional birthline used for the Galactic sources. Lamers et al. (1999) suggested that this could be due to either a shorter accretion time-scale for Galactic Herbig AeBe stars due to lower metallicity in the LMC, or a lower dust-to-gas ratio in the LMC, again owing to the lower metallicity. Therefore, for the SMC, a higher birthline for YSOs could be expected in the HR diagram. We note that the those candidates that were identified to have TiO emission features, within our survey, also lie to the right of the birthline (Wood et al. 2013).

11 VARIABILITY OF POST-AGB STARS

The variability of the final sample of post-AGB/RGB and YSO candidates was examined by using the light curves from MACHO (Alcock et al. 1992) and/or the OGLE II and OGLE III experiments (Udalski et al. 1997; Szymanski 2005; Soszynski et al. 2009, 2011). Light curves exist for 38 of the 63 post-AGB/RGB candidates and 20 of the 40 YSO candidates (Figs 12–14). In Fig. 15, we show the phased light curves for those stars that show a continuous periodic variability.

Of the 38 post-AGB/RGB candidates with light curves, 21 objects show no detectable periodicity. One of these 21 objects, J010623.71-724413.5, brightened by about 0.5 mag over a period of about 2500 d. This could be attributed to rapid changes in circumstellar dust obscuration.

13 stars, J004114.10-741130.1, J004441.03-732136.0, J004534.36-734811.8, J004614.67-723519.0, J004909.72-724745.4, J005113.04-722227.0, J005159.04-734214.4, J005310.8-722921.0, J005803.08-724405.1, J005447.59-740121.4, J005925.13-741309.6, J010021.78-730901.3 and J010254.90-722120.9 display semiregular variability with periods from ∼20–500 d. Their periods are listed in Table 9 when they could be determined.

J005803.08-732245 is also found to have a long secondary period (LSP) of 3700 d. LSPs are common in red giants (Wood et al. 1999; Percy & Bakos 2003; Soszyński 2007; Fraser, Hawley & Cook 2008). Two other candidates J004456.21-732256.6 and J003611.06-730447.0 exhibit LSPs of about 1800 and 1900 d, respectively. Stars with LSPs, also known as Sequence-D variables, are known to exhibit a mid-IR excess due to circumstellar dust (Wood et al. 1999; Wood & Nicholls 2009). The three stars: J005803.08-732245, J004456.21-732256.6 and J003611.06-730447.0 could be higher temperature analogues of the Sequence-D variables.

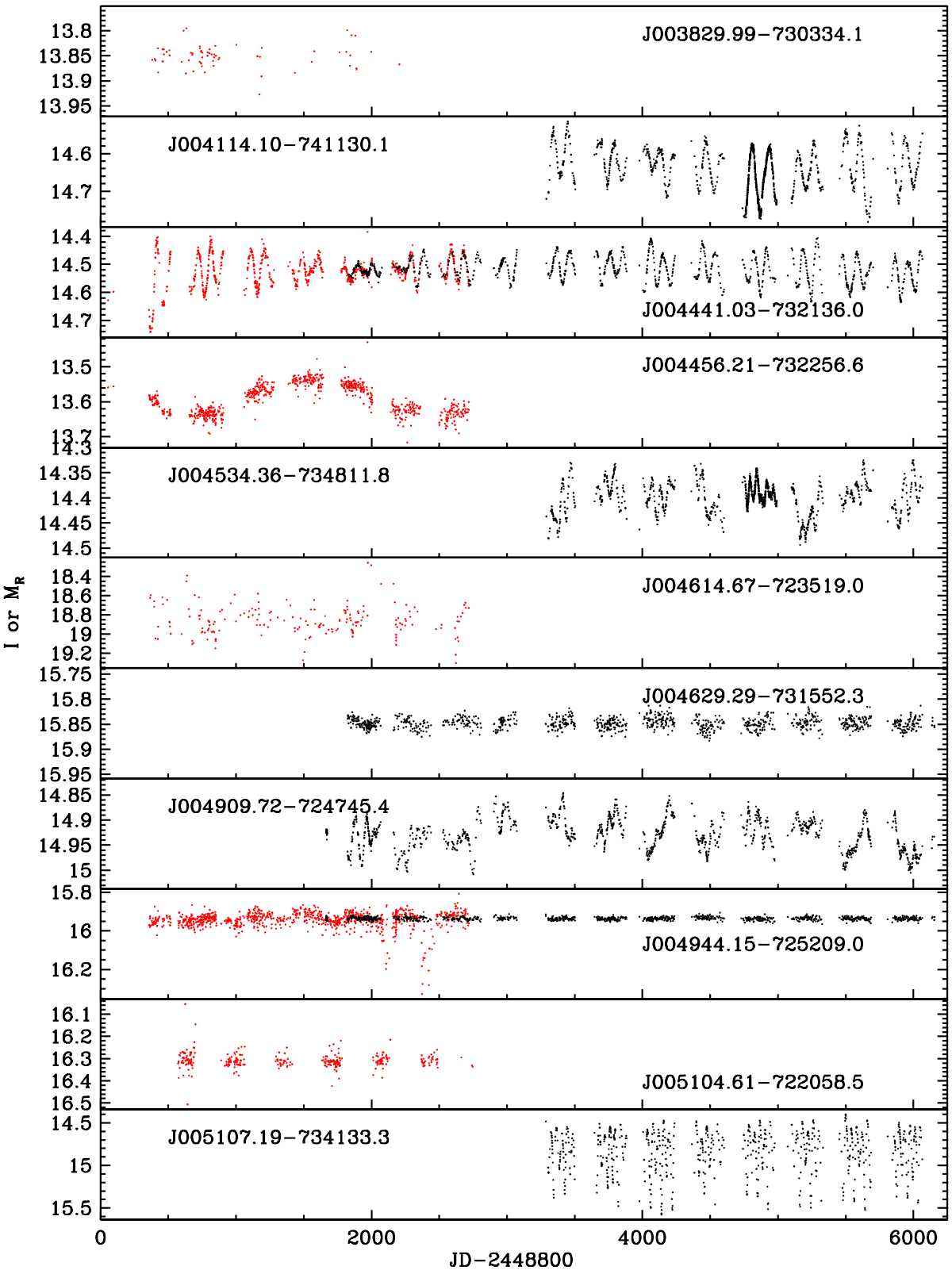

Figure 12. Light curves for the post-AGB/RGB Q1 candidates. The black light curves for dates later than JD−244 8800 > 3250 are from OGLE III, the black curves with 1700 < JD−244 8800 < 3250 are from OGLE II while the red curves with 0 < JD−244 8800 < 2800 are MACHO red magnitudes normalized to the OGLE *I* magnitudes over the interval 2000 < JD−244 8800 < 3250. The light curves are ordered by RA.

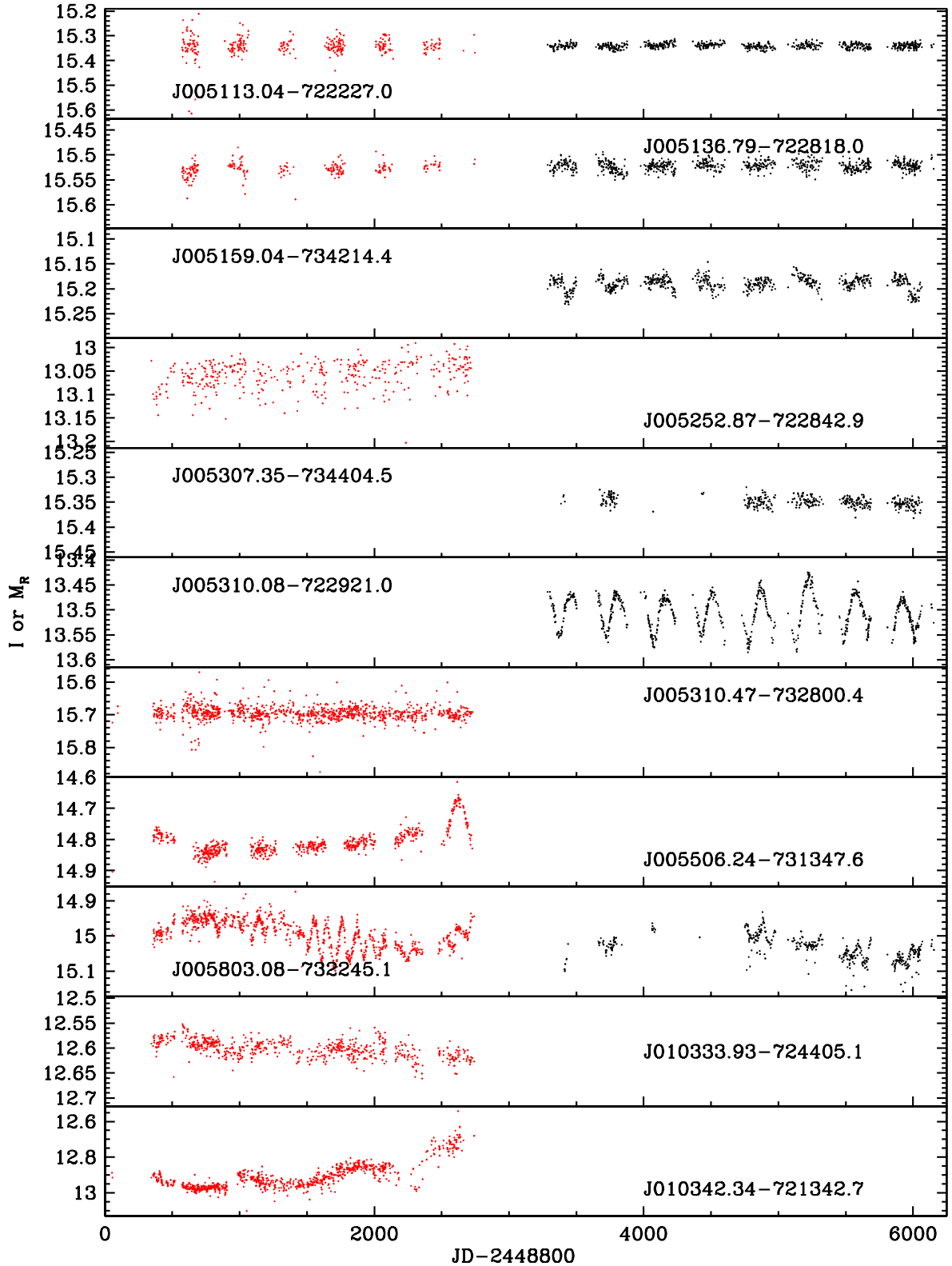

Figure 12 – *continued*

J005107.19-734133.3 shows smooth oscillations. From the phased light curve for this star (see Fig. 15), it is clear that these oscillations look RV-Tauri like with alternating deep and shallow minima and a period between alternating minima of 78.99 d. Based on the SED, J005107.19-734133.3 is classified as a disc source (see Section 8). RV-Tauri stars with circumstellar dust are mainly associated with circumbinary discs (Van Winckel et al. 1999; Gielen et al. 2008). Furthermore, visual inspection of the spectra of J005107.19-734133.3 indicates *s*-process enrichment (see Section 9), similar to MACHO47.2496.8 which is an *s*-process-rich RV-Tauri star in the

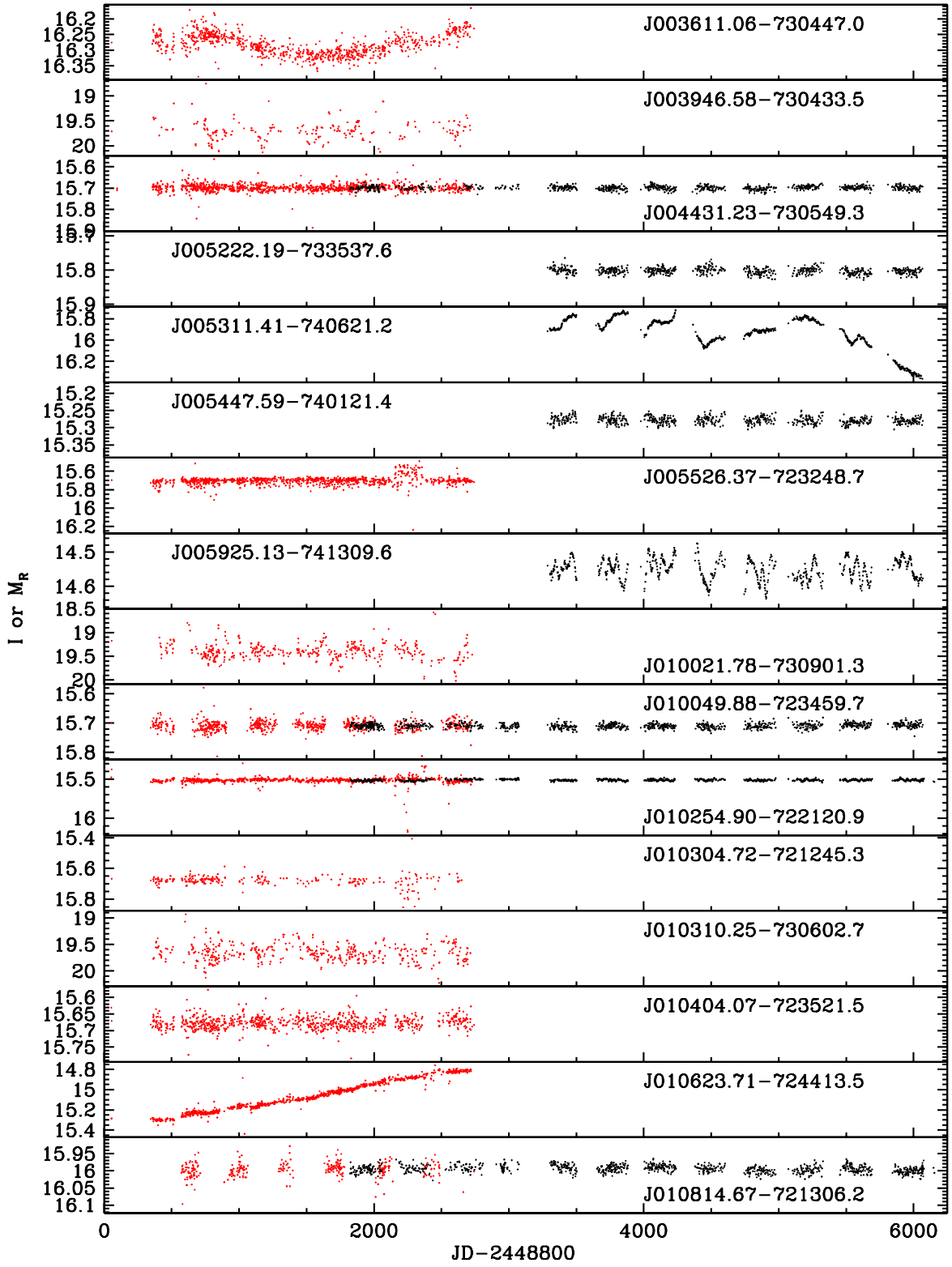

Figure 13. Same as Fig. 12, but for the high-probability quality 2 post-AGB/RGB candidates.

LMC (Reyniers et al. 2006), suggesting that J005107.19-734133.3 is a newly discovered RV-Tauri star in the SMC. High-resolution chemical abundance studies of J005107.19-734133.3 are required to confirm the *s*-process enrichment of this object.

The star J005310.08-722921.0 displays a slow regular oscillations with a slight hint of alternation in minima and maxima as shown in the phased light curve of this object (see Fig. 15). The time between alternate minima is about 350.9 d. For J005310.08-722921.0, the period seems too long to classify is as an RV Tauri star. The maximum period for RV Tauri stars in the SMC was found to be close to 100 d (Soszyñski et al. 2010). The more likely scenario is that this star is in a binary system.

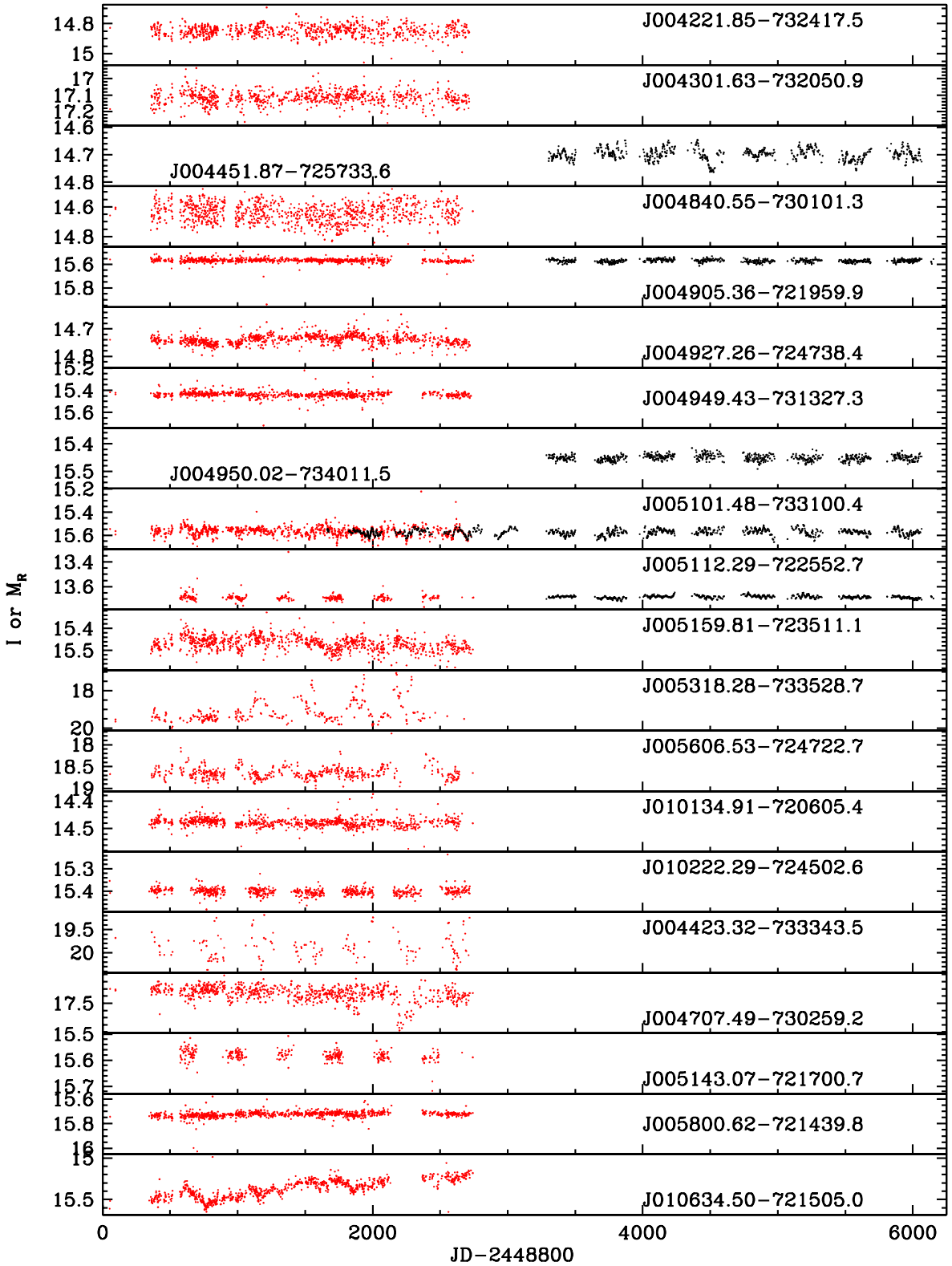

Figure 14. Same as Fig. 12 but for quality 1 (top 15 light curves) and quality 2 (bottom 5 light curves) YSO candidates.

J005311.41-740621.2 shows a fading in magnitude combined with a variation with a variable period between minima of 200–400 d. The fading could be due to an LSP of ∼3000 d.

Finally, J010342.34-721342.7 is another star with a combination of a slow brightening and a long period of about 900 d. This may be attributed to slow changes in dust obscuration or changes in the accretion rate.

20 of the YSO candidates have light curves. Amongst these candidates, six (J004301.63-732050.9, J004927.26-724738.4, J005159.81-723511.1,J005606.53-724722.7, J005800.62-

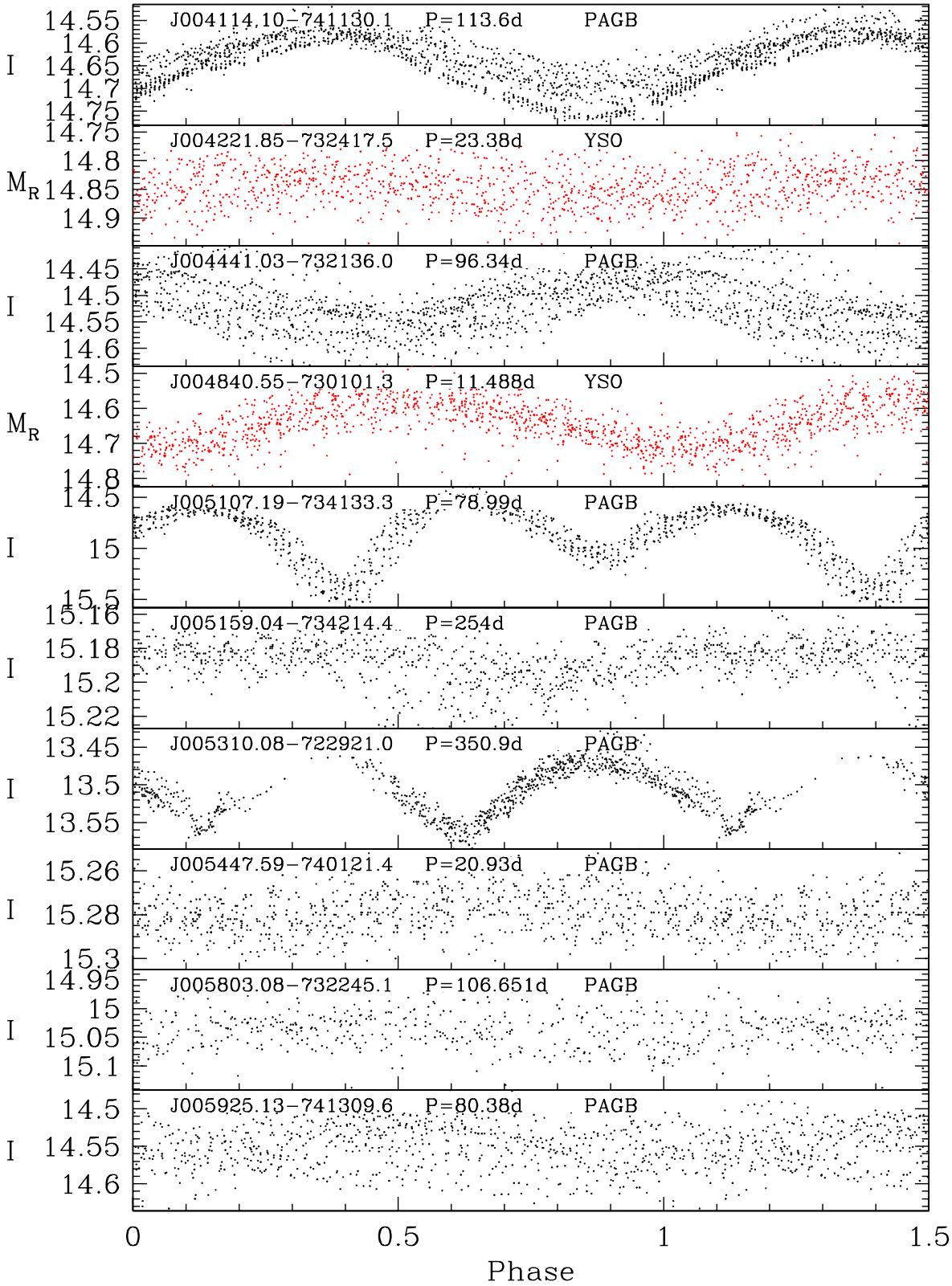

Figure 15. The phased light curves for those stars that show a continuous periodic variability. The object names, the periods and whether the object is estimated to be a post-AGB/RGB star or YSO is indicated in each panel. Phase zero is taken to be at JD = 244 8800. Only MACHO or OGLE data are used for a given object as indicated by the label on the magnitude axis and point colour (M_R and red points for MACHO data, I and black points for OGLE data). The RV Tauri star J005107.19-734133.3 is phased with the period between deep minima. The star J005310.08-722921.0 is also phased using the period between alternate minima although the evidence for an alternating depth of minima is marginal (the star could be an ellipsoidal binary).

Table 9. The sample of post-AGB/RGB and YSO candidates with MACHO and/or OGLE light curves. Periods are given when they could be determined.

Object Post-AGB/RGB Q1	*P* (d)	Object Post-AGB/RGB Q2	*P* (d)	Object YSO Q1	*P* (d)	Object YSO Q2	*P* (d)
J003829.99-730334.1	–	J003611.06-730447.0	1900→	J004221.85-732417.5	23.38	J004423.32-733343.5	–
J004114.10-741130.1	113.601	J003946.58-730433.5	–	J004301.63-732050.9	–	J004707.49-730259.2	–
J004441.03-732136.0	96.338	J004431.23-730549.3	–	J004451.87-725733.6	22.5,	J005143.07-721700.7	–
J004456.21-732256.6	1800:	J005222.19-733537.6	–	J004840.55-730101.3	11.488	J005800.62-721439.8	–
J004534.36-734811.8	59, 130	J005311.41-740621.2	200-400, 2972→	J004905.36-721959.9	–	J010634.50-721505.0	–
J004614.67-723519.0	87:	J005447.59-740121.4	20.926	J004927.26-724738.4	–	–	–
J004629.29-731552.3	–	J005925.13-741309.6	80.380	J004949.43-731327.3	–	–	–
J004909.72-724745.4	97	J010021.78-730901.3	–	J004950.02-734011.5	–	–	–
J004944.15-725209.0	–	J010049.88-723459.7	–	J005101.48-733100.4	30:	–	–
J005104.61-722058.5	–	J010254.90-722120.9	40:	J005112.29-722552.7	–	–	–
J005107.19-734133.3	78.990	J010304.72-721245.3	–	J005159.81-723511.1	–	–	–
J005113.04-722227.0	20	J010310.25-730602.7	–	J005318.28-733528.7	–	–	–
J005136.79-722818.0	–	J010404.07-723521.5	–	J005606.53-724722.7	–	–	–
J005159.04-734214.4	254	J010623.71-724413.5	–	J010134.91-720605.4	–	–	–
J005252.87-722842.9	–	J010814.67-721306.2	–	J010222.29-724502.6	–	–	–
J005307.35-734404.5	–	–	–	–	–	–	–
J005310.08-722921.0	89, 120	–	–	–	–	–	–
J005310.47-732800.4	–	–	–	–	–	–	–
J005506.24-731347.6	–	–	–	–	–	–	–
J005803.08-732245.1	106.651, 3700	–	–	–	–	–	–
J010333.93-724405.1	–	–	–	–	–	–	–
J010342.34-721342.7	900:	–	–	–	–	–	–

Note. Uncertain periods are denoted by ':'. → denotes that the true period is increasing from the estimated period with time.

721439.8 and J010634.50-721505.0) show erratic or secular long-term variations consistent with variations in dust obscuration by the circumstellar environment. J005318.28-733528.7 shows apparent variability which is probably not real but caused by an annual variation of about 365 d. Four stars, J004221.85-732417.5, J004451.87-725733.6, J004840.55-730101.3 and J005101.48-733100.4, show small oscillations with periods of 23.38, 22.5, 11.48 and 30 d, respectively. These small oscillations are similar to the ultrasmall amplitude oscillations displayed by stars that lie close to the Cepheid instability strip (Buchler, Wood & Soszyński 2009). This indicates that the four YSO candidates with small-amplitude oscillations could be crossing the Cepheid instability strip on their way to the main sequence.

12 COMPLETENESS OF THE SURVEY

This study is aimed at identifying optically visible post-AGB and RGB candidates in the SMC. However, the survey obviously has its limitations and does not catalogue all the post-AGB/RGB candidates in the SMC. In this section, we have listed the limitations that govern this survey and also provided the extent of the completeness of our survey.

The selection criteria used to identify the post-AGB/RGB candidates in this study requires a detection at 8 μm. The presence of a valid 8 μm detection and our selection criteria restrict our search to post-AGB/RGB candidates with an excess at 8 μm. Older post-AGB/RGB stars with expanding shells for which the excess starts redder than 8 μm will not be selected, for instance, the SMC counterparts of the hot Galactic post-AGB stars studied by Gauba & Parthasarathy (2004) will not be selected if the photospheric 8 μm detection is below the threshold. Furthermore, we require that all the selected candidates have a $V < 20$, which only selects those post-AGB/RGB stars that are optically visible, therefore omitting those that are heavily dust enshrouded.

Based on our selection criteria, we selected a sample of 1194 objects, out of which 150 objects were given a priority 1, 303 were given a priority 2 and 741 were given a priority 3. We note that the priorities were assigned based on the selection criteria used and the likelihood of finding post-AGB/RGB candidates with that selection criteria (see Section 1). We performed a low-resolution optical survey that covered the SMC, as shown in Fig. 2. From the initial selected sample of 1194 objects, we obtained spectra of 801 objects. Excluding the faint objects that had a low signal (<200 counts) and therefore a poor quality spectra, we were left with a sample of 621 unique spectra. In Table 10, we give a summary of the evolution of the number of post-AGB/RGB stars and YSO candidates as the analysis has proceeded. In Table 11, we give a breakdown of the number of objects with respect to their assigned priorities as the analysis has proceeded. Taking into consideration the candidates for which we did not obtain the low-resolution optical

Table 10. A summary of the evolution of the number of post-AGB/RGB stars and YSO candidates as analysis has proceeded.

Stage	Numbers of objects at various stage analysis
Initial photometric selection	1194
Objects with usable optical spectra	621
Final sample of post-AGB/RGB and YSO candidates with confirmed SMC membership and with stellar parameters derived from their spectra	103 (63 post-AGB/RGB, 40 YSOs)

Table 11. A breakdown of the number of objects with respect to their assigned priorities, as analysis has proceeded.

Stage	Total objects	Priority 1 objects	Priority 2 objects	Priority 3 objects
Initial photometric selection	1194	150	303	741
Objects with optical spectra	801	133	248	420
Objects rejected due to poor spectra	180	13	19	148
Objects retained with good optical spectra	621	120	229	272
Objects classified as M stars	20	9	8	3
Objects classified as C stars	140	12	126	2
Objects classified as PN	46	24	10	12
Objects classified as redshifted galaxies	204	1	13	190
Objects classified as QSOs	36	0	3	33
Objects with TiO in emission	9	8	1	0
Objects with strong emission lines and a UV continuum (probable hot post-AGB/RGB or luminous YSO candidates)	63	39	19	5
Sample of probable post-AGB/RGB and YSO candidates for which we carry out detailed spectral analysis	103	27	49	27
Final number of post-AGB/RGB candidates	63	19	30	14
Final number of YSO candidates	40	8	18	14

spectra and the objects that we rejected from the spectral analysis due to poor quality of their spectra, we estimate the completeness of the survey to be ≈50 per cent. However, when only considering the priority 1 objects, we find that we were able to study and assign candidature for 120 out of the 150 objects, resulting in ≈80 per cent completeness. Similarly, we estimate the completeness of the study of the priority 2 and priority 3 objects to be ≈76 and ≈37 per cent, respectively.

We can provide a rough estimate of the number of post-AGB/RGB candidates we expect to find in the unstudied sample (the sample of objects whose spectra were not obtained and those objects that were rejected due to poor spectra, see Table 11). 19 out of the 120 priority 1 objects turned out to be post-AGB/RGB candidates. So from the remaining unstudied sample of 30 priority 1 post-AGB/RGB candidates, we can expect ≈5 more likely post-AGB/RGB candidates. 30 out of the 230 priority 2 objects turned out to be post-AGB/RGB candidates. So from the remaining unstudied sample of 73 priority 2 candidates, we can expect ≈10 more likely post-AGB/RGB candidates. Similarly, from the group of 469 unstudied priority 3 post-AGB/RGB candidates, we can expect ≈24 more likely post-AGB/RGB candidates. This implies that it might be possible to identify a further group of ≈39 optically visible post-AGB/RGB candidates from the total unstudied group of initially selected candidates. Based on the ratio of post-AGB to post-RGB candidates in our current final sample, we can expect to find around 13 additional post-AGB candidates and 26 additional post-RGB candidates.

As part of the future work, we intend to complete the survey by obtaining the optical spectra for the objects that were not observed, and by re-observing those targets that had poor-quality spectra.

13 ESTIMATING POST-AGB/RGB EVOLUTIONARY RATES

The post-AGB/RGB phase of evolution is a very short lived phase. To be able to estimate the evolutionary rate, a complete sample of post-AGB stars is required. Furthermore, during the post-AGB/RGB phase, $T_{\rm eff}$ is determined by the mass of the hydrogen envelope (Schönberner 1981; Vassiliadis & Wood 1994). The rate of evolution in $T_{\rm eff}$ is therefore determined by the luminosity (which determines the rate of consumption of the hydrogen envelope by nuclear burning) and by the mass-loss rate (in the case of single post-AGB stars) and the mass re-accretion rate (in the case binary of post-AGB/RGB stars). This mass-loss rate/mass accretion rate is essentially completely unknown. Based on the available sample of post-AGB/RGB candidates from this study, we now try to estimate this mass-loss/accretion rate by determining the numbers of stars in a given $T_{\rm eff}$ interval along the post-AGB/RGB track and comparing those numbers to the number of stars in the top magnitude of the RGB, where the duration of evolution is known.

To estimate the lifetime on the top 1 mag of the RGB, we used the Bertelli et al. (2008) evolutionary tracks. They show that stars in the mass range 1.0–1.8 $M_{\odot}$ and SMC-like metallicity ($Z = 0.004$) take $\sim 3 \times 10^6$ years to traverse the top magnitude of the RGB. Subsequent AGB evolution through the same luminosity range takes $\sim 1 \times 10^6$ yr. Hence, the total time spent by a low-mass star in the luminosity range corresponding to the top 1 mag of the RGB is $\sim 4 \times 10^6$ yr.

In order to estimate the observed number of stars on the top magnitude of the RGB in the four fields SMC1–4, we followed the prescriptions in Nie, Wood & Nicholls (2012). Stars in the SAGE-SMC catalogue (Gordon et al. 2011) were plotted in the J, J-[3.6] diagram and those in a parallelogram coinciding with the top 1 mag of the RGB were selected. The parallelogram has sides $J = 13.9$, $J = 14.9$, J-[3.6] = 3.25–0.17J and J-[3.6] = 3.75–0.17J. We find that the numbers of stars $n1$, $n2$, $n3$ and $n4$ in each of SMC1, SMC2, SMC3 and SMC4 are 6861, 9540, 5217 and 5343, respectively, with an error of approximately 5 per cent (Nie et al. 2012). The total number of stars in the magnitude interval corresponding to the top mag of the RGB in all four SMC fields is thus 26 961.

Next, we estimated the lifetimes of the stars in the early part of the post-AGB/RGB phase. If we assume that post-AGB stars, whether they leave the AGB by single star mass-loss or binary interaction, have all passed through the top magnitude of the RGB, then we can easily derive their average post-AGB lifetime. If there are $N_{\rm AGB}$ post-AGB stars ($\log L \gtrsim 3.4$) in all four SMC fields in a certain evolutionary phase (say from the AGB to $T_{\rm eff}$= 6000 K, i.e. $\sim 3.6 < \log T_{\rm eff} < \sim 3.8$), then the lifetime of these stars in that evolutionary phase is $4 \times 10^{6*} N_{\rm AGB}/26\,961$ years. From our analysis, we find a total of $N_{\rm AGB} = 21$ which results in a post-AGB lifetime of 3115 yr. We note that the estimated lifetime assumes that the sample of in the fields SMC1–4 is complete.

For post-RGB stars, the calculation is not so easy. Nie et al. (2012) find that ∼4 per cent of red giants evolving up the RGB produce post-RGB stars when they fill their Roche lobes before reaching the RGB tip. The Nie et al. (2012) calculations were done for the LMC but we assume they also apply for the SMC. Most of the post-RGB stars are produced during the top 2 mag of the RGB where most of our post-RGB stars are observed. The median luminosity of these stars is log $L/L_{\odot} \sim 2.8$. In this case, if $N_{\rm RGB}$ post-RGB stars are observed, then their average lifetime is $4 \times 10^{6*}(N_{\rm RGB}/0.04)/26\,961$ yr. From our analysis, we find a total of $N_{\rm RGB} = 42$ post-RGB candidates, which results in a post-RGB lifetime of 155 780 yr.

We need to compare the above lifetimes to those of post-AGB/RGB stars without external mass-loss during the post-AGB life. The evolutionary track of Bertelli et al. (2008) with $M = 1.2$ M$_{\odot}$ and metallicity $Z = 0.004$ was used as the starting point. The core mass at a number of luminosities on the RGB and AGB was extracted. Then static models were made with varying envelope masses and hence $T_{\rm eff}$values in order to simulate stars that have left the RGB or AGB at these luminosities (the static model code used was that of Fox & Wood (1982), with updated physics as described in Soszyński & Wood 2013). Post-RGB and post-AGB stars evolve at constant luminosity to higher $T_{\rm eff}$ values and, in the absence of mass-loss, the rate of evolution is determined by the rate at which the hydrogen-rich envelope is consumed by the H-burning shell. Most of our observed post-RGB stars (which have log $L/L_{\odot} <$ 3.4) have log $T_{\rm eff} < 3.8$ so we estimate the time Δt it takes for a post-RGB star to traverse from log $T_{\rm eff}$(RGB) + 0.05 to log $T_{\rm eff} =$ 3.8 by consuming the hydrogen-rich envelope. A helium mass fraction $Y = 0.25$ was assumed and the H-burning shell was assumed to provide all the surface luminosity. Similarly, we compute the time Δt for a post-AGB star to traverse the interval $3.7 <$ log $T_{\rm eff} < 3.9$ where most of the observed post-AGB stars lie. These times are given in Table 12.

We find that for the post-AGB stars, the observational lifetime = 3115, and the lifetime for post-AGB evolution without post-AGB mass-loss from log $T_{\rm eff} =$ 3.7–3.9 and for an intermediate-luminosity star (log $L/L_{\odot} = 3.8$) is 9300 yr. Formally, these numbers suggest that some mass-loss is required to hasten the evolution. This mass-loss rate is $M_{\odot} = 7 \times 10^{-8}$ M$_{\odot}$ yr^{-1} but the uncertainties are very large. For the RGB stars, the observational lifetime = 155 780, and the lifetime for post-AGB evolution without mass-loss from log $T_{\rm eff}$(RGB) + 0.05 to log $T_{\rm eff} = 3.8$ and for an intermediate-luminosity star (log $L/L_{\odot} = 3.0$) is 101 000 yr. The agreement is good. Formally, the numbers suggest that a small amount of mass accretion is required in the post-RGB phase to match the observed and predicted numbers of post-RGB stars. Overall, these results suggest that the numbers of post-AGB and post-RGB stars that we have found are in reasonable agreement with stellar evolution models that have some mass-loss in the post-AGB phase and a very low amount of re-accretion in the lower luminosity RGB phase.

We note that the estimated lifetime assumes that the sample of stars in the fields SMC1–4 is complete. However, as mentioned in Section 12, our survey is not entirely complete and we can expect to find an additional sample of 13 post-AGB candidates and 26 post-RGB candidates. To illustrate the impact of this addition, we recalculated the lifetimes and we estimate a post-AGB lifetime of 5044 yr and a post-RGB lifetime of 252 216 yr. These lifetimes are not greatly different from the lifetimes we have estimated from the current sample so that our conclusions on the estimated lifetimes for the post-AGB and post-RGB phases remain valid.

Table 12. Evolutionary rates for post-AGB/RGB stars of different core-mass ($M_{\rm core}/$ M$_{\odot}$).

Stage	log $L/L_{\odot}$	$M_{\rm core}/$ M$_{\odot}$	Δt (yr)
RGB	2.6	0.347	139 000
RGB	3.0	0.396	101 000
RGB	3.4	0.463	163 000
AGB	3.4	0.536	17 400
AGB	3.8	0.598	9300

14 SUMMARY AND CONCLUSIONS

We have identified a sample of 63 high-probability post-AGB/RGB candidates in the SMC with spectral types between A and K. Of these 63 objects, 42 are post-RGB candidates and 21 are post-AGB candidates. Being an evolved class of objects, they have a lower metallicity ([Fe/H] = −1.14) than the mean present-day SMC metallicity. The J-[3.6] versus [3.6]–[8] colour–colour plot and the SEDs allowed us to distinguish between single (shell sources) and binary (mostly discs) post-AGB/RGB populations, resulting in 6 shell sources and 27 disc sources. For the remaining 30 sources, we were unable to establish their nature. However, majority of these sources are post-RGB candidates which are known to be binaries and therefore likely disc sources. Detailed studies are required to confirm the true nature of all these sources. The low-resolution spectra of these objects revealed the definite presence of barium for six candidates and lithium for seven candidates, both of which are expected products of the nucleosynthesis during the AGB phase of evolution. Variability is displayed by 38 of the 63 post-AGB/RGB candidates with the most common variability types being the Population II Cepheids (including RV-Tauri stars) and semiregular variables. This study has resulted in the discovery of a new RV-Tauri star, J005107.19-734133.3, which shows signs of *s*-process enrichment, based on visual inspection of the low-resolution spectrum. We also used the reliable numbers of these objects, to study the evolutionary rates and mass-loss/mass accretion rates. We found that the numbers of post-AGB require stellar evolution models with some mass-loss and the number of RGB stars suggests a very small amount of re-accretion of gas.

This study has also resulted in a new sample of YSOs, since YSOs also display a large IR excess and are present in the luminosity range occupied by post-AGB stars. We identified a sample of 40 high-probability YSO candidates. The high-probability population has temperatures ranging between 4000 and 9000 K, high surface gravities, and a mean metallicity [Fe/H] = −0.62, which agrees well with the average present-day SMC metallicity. From the position of these YSO candidates on the HR diagram, we were able to infer that they have masses of ∼3– 10 M$_{\odot}$. An interesting finding is that most of these YSO candidates lie to the right of the birthline where previous studies have shown that the objects are not visible. Both groups of YSO candidates showed Hα emission and forbidden line emission indicative of disc accretion in YSOs. We were also able to identify the presence of Li in three candidates. Four of the YSO candidates with light curves show low-amplitude periodicity which is probably associated with Cepheid-like pulsations as the stars cross the instability strip. Slow variations in the obscurations by circumstellar matter are seen in both post-AGB/RGB stars and YSOs but they are more common in the latter.

We have also identified a group of 63 hot objects whose spectra show emission lines and in some cases, a significant UV continuum. These objects are likely to be either hot post-AGB/RGB or luminous YSO candidates (presented in Appendix A). Based on a visual inspection of their spectra and SEDs, we were able to establish the most probable nature of the objects, resulting in 40 probable hot post-AGB/RGB candidates and 23 probable YSO candidates.

This study has also resulted in the discovery of a significant number contaminants. They are: M-stars, C-stars and PNe (presented in Appendix B), a group of QSOs and redshifted galaxies (to be presented in a following publications), and a group of stars with TiO band emission (Wood et al. 2013).

We note that, due to limitations introduced by the selection criteria, our study is restricted to optically visible post-AGB/RGB stars of spectral type A–K, in the SMC. The completeness of this survey is ≈50 per cent since we were not able to obtain spectra all of the candidates from within the initially selected sample of candidates and some of the candidates with optical spectra were rejected as their spectra were of poor quality due to the faintness of the targets combined with the low resolution of our spectra (≈1300). Based on the current final sample of post-AGB/RGB candidates (of A–K) in the SMC, we expect to find approximately an additional 39 such candidates (13 post-AGB and 26 post-RGB candidates).

ACKNOWLEDGEMENTS

DK would like to thank Professor Martin Asplund for his valuable discussions and advice throughout the project. DK would also like to thank George Zhou for his help while developing the STP and Dr Rob Sharp for his useful tips during data reduction of the AAOmega spectra

We thank the Australian Astronomical Observatory for allowing us to use the observatory facilities and our AAT support astronomer, Dr Paul Dobbie, who was very helpful during our observing run. We thank the AAO Service Program, especially Dr Sarah Brough and Dr Daniel Zucker, our service observers, for observing one of the SMC fields.

We would also like to thank the referee for his/her comments and suggestions.

PRW was partly supported during this work by Australian Research Council Discovery Project grant DP1095368.

DK acknowledges support of the FWO grant G.OB86.13. HVW and DK acknowledge support of the KU Leuven contract GOA/13/012.

REFERENCES

Alcock C. et al., 1992, in Filippenko A. V., ed., ASP Conf. Ser. Vol. 34, Robotic Telescopes in the 1990s. Astron. Soc. Pac., San Francisco, p. 193
Belczyński K., Mikołajewska J., Munari U., Ivison R. J., Friedjung M., 2000, A&AS, 146, 407
Bertelli G., Girardi L., Marigo P., Nasi E., 2008, A&A, 484, 815
Bertelli G., Nasi E., Girardi L., Marigo P., 2009, A&A, 508, 355
Blum R. D. et al., 2006, AJ, 132, 2034
Bolatto A. D. et al., 2007, ApJ, 655, 212
Bonanos A. Z. et al., 2009, AJ, 138, 1003
Boothroyd A. I., Sackmann I.-J., Wasserburg G. J., 1995, ApJ, 442, L21
Boyer M. L. et al., 2011, AJ, 142, 103
Buchler J. R., Wood P. R., Soszyński I., 2009, ApJ, 698, 944
Cardelli J. A., Clayton G. C., Mathis J. S., 1989, ApJ, 345, 245
Castelli F., Kurucz R. L., 2003, in Piskunov N., Weiss W. W., Gray D. F., eds, Proc. IAU Symp. 210, Modelling of Stellar Atmospheres. Astron. Soc. Pac., San Francisco, p. 20P
Chiosi C., Wood P. R., Capitanio N., 1993, ApJS, 86, 541
Cioni M. R., Habing H. J., Loup C., Groenewegen M. A. T., Epchtein N. DENIS Consortium, 1999, in Whitelock P., Cannon R., eds, Proc. IAU Symp. 192, The Stellar Content of Local Group Galaxies. Astron. Soc. Pac., San Francisco, p. 65
De Propris R., Rich R. M., Mallery R. C., Howard C. D., 2010, ApJ, 714, L249
de Ruyter S., Van Winckel H., Maas T., Lloyd Evans T., Waters L. B. F. M., Dejonghe H., 2006, A&A, 448, 641
De Smedt K., Van Winckel H., Karakas A. I., Siess L., Goriely S., Wood P. R., 2012, A&A, 541, A67
Dermine T., Izzard R. G., Jorissen A., Van Winckel H., 2012, preprint (arXiv:e-prints)
Epchtein N., 1998, in McLean B. J., Golombek D. A., Hayes J. J. E., Payne H. E., eds, Proc. IAU Symp. 179, New Horizons from multiWavelength Sky Surveys. Kluwer, Dordrecht, p. 106
Field G. B., 1973, Science, 179, 991
Fox M. W., Wood P. R., 1982, ApJ, 259, 198
Fraser O. J., Hawley S. L., Cook K. H., 2008, AJ, 136, 1242
Frew D. J., Parker Q. A., 2010, Publ. Astron. Soc. Aust., 27, 129
Frogel J. A., Cohen J. G., Persson S. E., 1983, ApJ, 275, 773
Gauba G., Parthasarathy M., 2004, A&A, 417, 201
Gielen C., Van Winckel H., Min M., Waters L. B. F. M., Lloyd Evans T., 2008, A&A, 490, 725
Gielen C. et al., 2009, A&A, 508, 1391
Gielen C. et al., 2011, in Kerschbaum F., Lebzelter T., Wing R. F., eds, ASP Conf. Ser. Vol. 445, Why Galaxies Care about AGB Stars II: Shining Examples and Common Inhabitants. Astron. Soc. Pac., San Francisco, p. 281
Gordon K. D. et al., 2011, AJ, 142, 102
Gray D. F., 1992, Science, 257, 1978
Groenewegen M. A. T., 2000, A&A, 363, 901
Habing H. J., Olofsson H., 2003, Asymptotic Giant Branch Stars. Springer-Verlag, Berlin
Han Z., Podsiadlowski P., Eggleton P. P., 1995, MNRAS, 272, 800
Heiter U. et al., 2002, A&A, 392, 619
Iben I., Jr, Tutukov A. V., Yungelson L. R., 1996, ApJ, 456, 750
Jacoby G. H., 1980, ApJS, 42, 1
Jacoby G. H., De Marco O., 2002, AJ, 123, 269
Jayawardhana R., Mohanty S., Basri G., 2002, ApJ, 578, L141
Karakas A. I., Lattanzio J. C., 2003, Publ. Astron. Soc. Aust., 20, 279
Keller S. C., Wood P. R., 2006, ApJ, 642, 834
Kirkpatrick J. D. et al., 1999, ApJ, 519, 802
Kontizas E., Dapergolas A., Morgan D. H., Kontizas M., 2001, A&A, 369, 932
Kraemer K. E., Sloan G. C., Bernard-Salas J., Price S. D., Egan M. P., Wood P. R., 2006, ApJ, 652, L25
Kučinskas A., Vansevičius V., Sauvage M., Tanabé T., 2000, A&A, 353, L21
Kwok S., 1993, ARA&A, 31, 63
Lagadec E. et al., 2007, MNRAS, 376, 1270
Lamers H. J. G. L. M., Beaulieu J. P., de Wit W. J., 1999, A&A, 341, 827
Lattanzio J., Frost C., Cannon R., Wood P. R., 1996, Mem. Soc. Astron. Ital., 67, 729
Lewis I. J. et al., 2002, MNRAS, 333, 279
Loup C., Zijlstra A. A., Waters L. B. F. M., Groenewegen M. A. T., 1997, A&AS, 125, 419
Luck R. E., Moffett T. J., Barnes T. G., III, Gieren W. P., 1998, AJ, 115, 605
Meixner M. et al., 2006, AJ, 132, 2268
Men'shchikov A. B., Schertl D., Tuthill P. G., Weigelt G., Yungelson L. R., 2002, A&A, 393, 867
Meyssonnier N., Azzopardi M., 1993, A&AS, 102, 451
Min M., Jeffers S. V., Canovas H., Rodenhuis M., Keller C. U., Waters L. B. F. M., 2013, A&A, 554, A15
Miszalski B., Shortridge K., Saunders W., Parker Q. A., Croom S. M., 2006, MNRAS, 371, 1537
Morgan D. H., 1995, A&AS, 112, 445
Morgan D. H., Good A. R., 1985, MNRAS, 213, 491
Munari U., Sordo R., Castelli F., Zwitter T., 2005, A&A, 442, 1127
Murphy M. T., Bessell M. S., 2000, MNRAS, 311, 741

Natta A., Testi L., Comerón F., Oliva E., D'Antona F., Baffa C., Comoretto G., Gennari S., 2002, A&A, 393, 597
Nie J. D., Wood P. R., Nicholls C. P., 2012, MNRAS, 423, 2764
Oliveira J. M. et al., 2013, MNRAS, 428, 3001
Paczyiński B., Sienkiewicz R., 1972, Acta Astron., 22, 73
Palla F., Stahler S. W., 1993, ApJ, 418, 414
Percy J. R., Bakos A. G., 2003, in Gray R. O., Corbally C. J., Philip A. G. D., eds, The Garrison Festschrift. Davis Press, Schenectady, NY, p. 49
Reyniers M., Abia C., Van Winckel H., Lloyd Evans T., Decin L., Eriksson K., 2006, Mem. Soc. Astron. Ital., 77, 949
Reyniers M., van de Steene G. C., van Hoof P. A. M., Van Winckel H., 2007, A&A, 471, 247
Rieke G. H. et al., 2004, ApJS, 154, 25
Sanduleak N., 1978, ApJ, 221, 586
Sanduleak N., Pesch P., 1981, PASP, 93, 431
Schlegel D. J., Finkbeiner D. P., Davis M., 1998, ApJ, 500, 525
Schönberner D., 1981, A&A, 103, 119
Schönberner D., 1983, ApJ, 272, 708
Sharp R. et al., 2006, in McLean I. S., Iye M., eds, Proc. SPIE Conf. Ser. Vol. 6269, Ground-based and Airborne Instrumentation for Astronomy. SPIE, Bellingham, p. 62690G
Sharp R., Brough S., Cannon R. D., 2013, MNRAS, 428, 447
Simon J. D. et al., 2007, ApJ, 669, 327
Skrutskie M. F. et al., 2006, AJ, 131, 1163
Soszyński I., 2007, ApJ, 660, 1486
Soszyński I., Wood P. R., 2013, ApJ, 763, 103
Soszyński I. et al., 2008, Acta Astron., 58, 293
Soszyński I. et al., 2009, Acta Astron., 59, 335
Soszyński I., Udalski A., Szymański M. K., Kubiak M., Pietrzyński G., Wyrzykowski Ł., Ulaczyk K., Poleski R., 2010, Acta Astron., 60, 91
Soszyński I. et al., 2011, Acta Astron., 61, 285
Stahler S. W., 1983, ApJ, 274, 822
Szczerba R., Siódmiak N., Stasińska G., Borkowski J., 2007, A&A, 469, 799
Szymanski M. K., 2005, Acta Astron., 55, 43
Tognelli E., Prada Moroni P. G., Degl'Innocenti S., 2011, A&A, 533, A109
Tonry J., Davis M., 1979, AJ, 84, 1511
Trams N. R. et al., 1999, A&A, 346, 843
Udalski A., Szymanski M., Kubiak M., Pietrzynski G., Wozniak P., Zebrun K., 1997, Acta Astron., 47, 431
van Aarle E., Van Winckel H., Lloyd Evans T., Ueta T., Wood P. R., Ginsburg A. G., 2011, A&A, 530, A90
van Aarle E., Van Winckel H., De Smedt K., Kamath D., Wood P. R., 2013, A&A, 554, A106
van Loon J. T., Oliveira J. M., Gordon K. D., Sloan G. C., Engelbracht C. W., 2010, AJ, 139, 1553
Van Winckel H., 2003, ARA&A, 41, 391
Van Winckel H., 2007, Balt. Astron., 16, 112
Van Winckel H., Reyniers M., 2000, A&A, 354
Van Winckel H., Waelkens C., Fernie J. D., Waters L. B. F. M., 1999, A&A, 343, 202
Van Winckel H. et al., 2009, A&A, 505, 1221
Vanden Berk D. E. et al., 2001, AJ, 122, 549
Vassiliadis E., Wood P. R., 1993, ApJ, 413, 641
Vassiliadis E., Wood P. R., 1994, ApJS, 92, 125
Volk K. et al., 2011, ApJ, 735, 127
Wallerstein G., Knapp G. R., 1998, ARA&A, 36, 369
Waters L. B. F. M., Trams N. R., Waelkens C., 1992, A&A, 262, L37
Whitelock P. A., Feast M. W., Menzies J. W., Catchpole R. M., 1989, MNRAS, 238, 769
Wilke K., Stickel M., Haas M., Herbstmeier U., Klaas U., Lemke D., 2003, A&A, 401, 873
Wood P. R., Nicholls C. P., 2009, ApJ, 707, 573
Wood P. R., Zarro D. M., 1981, ApJ, 247, 247
Wood P. R. et al., 1999, in le Bertre T., Lèbre A., Waelkens C., eds, Proc. IAU Symp. Vol. 191, Asymptotic Giant Branch Stars. Astron. Soc. Pac., San Francisco, p. 151
Wood P. R., van Aarle E., Van Winckel H., Lloyd Evans T., Ueta T., 2011, in ZijlstraA A., Lykou F., McDonald I., Lagadec E., eds, Asymmetric Planetary Nebulae 5 Conf., Infrared-selected post-AGB star candidates in the LMC and SMC. Jodrell Bank Centre for Astrophysics, p. 73P
Wood P. R., Kamath D., Van Winckel H., 2013, MNRAS, 435, 355
Wright E. L. et al., 2010, AJ, 140, 1868
Zaritsky D., Harris J., Thompson I. B., Grebel E. K., Massey P., 2002, AJ, 123, 855

APPENDIX A: CANDIDATES WITH STRONG EMISSION FEATURES: HOT POST-AGBs

In this section, we present the 63 objects that have strong emission features and a significant UV continuum. Based on their spectra, we find that, these objects can either be hot post-AGB candidates or YSO candidates with a strong UV continuum. Table A1 lists the important spectral features that we were able to identify. We also provide positional cross-matchings for those objects found in previous studies and the estimated observed luminosity ($L_{\rm obs}$) for each of the objects. $L_{\rm obs}$ is computed by integrating under the flux distribution at observed wavelengths, is a lower limit to the real luminosity of the object because of the large amount of flux beyond 24 μm and for hot photospheres the luminosity contribution from the region blueward of the *B* filter. Fig. A1 shows the spectra of these 63 objects. Fig. A2 shows the same stars but the plots have been scaled to show the continuum. The observed SEDs of these 63 candidates are shown in Fig. A3. Based on a visual inspection of their spectra and SEDs, we have tried to establish the most probable nature of the object (either hot post-AGB/RGB or YSO). Hot-post AGB/RGB stars are likely to have an emission-line spectrum characterized by weak recombination lines of hydrogen and helium and various collisionally excited forbidden lines of heavier elements (e.g. Van Winckel 2003). The spectra of YSO candidates are likely to show a broad Hα line profile owing to the disc accretion in YSOs (Jayawardhana et al. 2002; Natta et al. 2002). Furthermore, the YSO objects show a flared SED peaking at longer wavelengths (mostly >100 μm). This classification results in 40 probable hot post-AGB/RGB candidates and 23 probable YSOs. In Table A1, we list the probable nature of each of these objects.

Table A1. The list of candidates with emission lines and a UV continuum. In this table, 'a' represents absorption, 'e' represents emission, '0' indicates that the feature is not observed. ':' indicates that there is some line blending that has taken place or there is an absorption line with an emission core or the line indicates signs of strong winds and therefore mass-loss. '?' represents that the nature of the spectral line is uncertain.

Name	Previous identification	$L_{\rm obs}$/ $L_\odot$	Type	Hα	Hβ	Hγ	[O III]	[O III]	He I	He I	[S II]	[S II]	[N II]	[N II]	Ca II	Ca II	Ca II	Li	Ba	Pa
Wavelength (Å)		minimum		6563	4861	4341	4659	5007	4471	5876	6717	6731	6548	6584	8498	8542	8662	6708	4554	–
J002810.39-725844.5	IR[1],PN[2, 3] I25[4], I100[5], FIR[6]	15 128	YSO	e	e	e	0	e	0	0	e	e	0	0	0	0	0	0	0	0
J003543.47-732110.7	I25[4], FIR[6], I60[7]	7009	hot pA/R	e	e	e	0	0	0	0	e	e	0	0	e	e	e	a?	0	e
J003717.72-730020.8	RGB[6]	1135	YSO	e	e	e	0	e	0	0	e	e	0	0	0	0	0	0	0	0
J004419.98-725205.8	–	1972	hot pA/R	e:	e	e:	0	0	e:	0	0	0	0	0	a?	a	a	0	0	a?
J004535.80-731412.2	–	21 252	hot pA/R	0	a	a	0	0	a	a	0	0	0	0	0	0	0	0	0	a

Table A1 – *continued*

Name	Previous identification	$L_{obs}/L_{\odot}$	Type	Hα	Hβ	Hγ	[O III]	[O III]	He I	He I	[S II]	[S II]	[N II]	[N II]	Ca II	Ca II	Ca II	Li	Ba	Pa
Wavelength (Å)		minimum		6563	4861	4341	4659	5007	4471	5876	6717	6731	6548	6584	8498	8542	8662	6708	4554	–
J004607.42-731124.6	–	2868	hot pA/R	e	e	a:	0	e?	a	0	0	0	0	0	a	a	a	0	0	0
J004654.98-730833.6	FIR[6], SB[8, 9]	28 202	hot pA/R	e	e	e	e?	e?	0	0	e	e	0	0	0	0	0	0	0	e
J004655.70-733158.4	–	1161	YSO	e	e	e	0	e	0	e?	e	e	0	0	0	0	0	0	0	0
J004706.19-730759.2	–	2277	YSO	e	e	e	0	e	0	0	e	e	0	0	0	0	0	0	0	e
J004752.33-731711.5	FIR[6]	10 649	YSO	e	e	e	0	e	0	0	e	e	0	0	0	0	0	0	0	0
J004805.74-731743.3	FIR[6]	2553	YSO	e	e	e	0	e	0	0	e	e	e?	e?	0	0	0	0	0	e
J004830.60-730353.1	Em[8]	1811	hot pA/R	e	e	e	0	e	e?	e?	e	e	0	0	0	0	0	0	0	e
J004842.90-730311.0	Em[8]	1129	hot pA/R	e	e	e	0	e	e?	e?	e	e	0	0	0	0	0	0	0	e
J004849.01-731123.2	–	783	hot pA/R	e	e	e:	0	e	0	e?	e	e	e?	e?	0	0	0	0	0	e
J004929.11-723532.2	Em[10]	3633	hot pA/R	e	e	e	0	e	0	e?	e	e	0	e?	0	0	0	0	0	e
J004934.21-724855.1	–	667	YSO	e	e	e:	0	e	0	e?	e	e	0	0	0	0	0	0	0	e
J005047.44-721019.6	Em*[8, 9]	2159	hot pA/R	e	e	a	0	0	a	a	e	e	0	0	a	a	a	a	0	a
J005131.58-730911.7	–	745	hot pA/R	e	e	a	0	e	0	0	e	e	0	0	a	a	a	e?	0	0
J005157.72-731421.8	Em[3, 8, 11]	822	hot pA/R	e	e	e	0	e	0	e?	e	e	0	0	0	0	0	0	0	e
J005246.33-724244.5	Em*[8]	8465	hot pA/R	e	e	e:	0	e	a	e	e	e	0	0	e	e	e	0	0	e
J005252.48-731833.9	Em*[8]	3134	hot pA/R	e	e	e	e	e	a	0	e	e	0	0	e	e	e	0	0	e
J005309.86-731141.9	–	3084	hot pA/R	e:	a:	a	0	e	a	a	e	e	0	0	0	0	0	a	0	0
J005339.94-725218.6	x-AGB[6]	11 425	hot pA/R	e	e	e:	e?	e	e?	e	e	e	0	0	0	0	0	0	0	0
J005344.56-731237.1	Em[8, 9]	6425	hot pA/R	e	e	e	0	e	0	e?	0	0	0	0	0	e	e	a?	0	e
J005409.46-724143.1	x-AGB[6], Be[8]	25 304	hot pA/R	e	e	e	e	e	e	e	e	e	0	0	0	0	0	0	0	e
J005439.09-722923.1	Em*[8]	6891	hot pA/R	e	e	e	e	e	0	e	0	0	0	0	e	e	e	0	0	e
J005444.94-724109.8	–	3671	hot pA/R	e	e	e	0	e	a	0	e	e	0	0	0	0	0	0	0	e
J005648.54-724820.4	–	2062	hot pA/R	e	e	a:	0	0	a	a	e	e	0	0	0	0	0	0	0	e?
J005734.23-722654.6	–	12 117	hot pA/R	a	a	a	0	0	a	?	0	0	0	0	0	0	0	0	0	a
J005753.72-723317.5	–	1878	hot pA/R	e	e	e	0	e	a	0	0	0	0	0	e	e	e	0	0	e
J005809.94-721102.0	–	15 088	hot pA/R	e	e	0	0	e	a	0	e	e	0	0	e	e	e	0	0	e
J005929.09-720104.6	Em[8, 9]	42 499	hot pA/R	e	e	e	0	e?	0	0	0	0	0	0	e	e	e	0	0	e
J005942.38-714445.6	–	1040	YSO	e	e	e	0	e	0	e?	e	e	0	0	0	0	0	0	0	e
J010053.80-714649.1	–	1263	YSO	e	e	e:	0	e	e?	0	e?	e?	0	0	0	0	0	0	0	0
J010138.43-715655.5	HII[3, 8, 11]	1194	hot pA/R	e	e	e	e	e	e	e	e	e	0	0	0	e	e	0	0	e
J010229.46-720153.3	RGB[6]	495	YSO	e	e	e	0	e	0	e?	e	e	0	0	0	0	0	0	0	e?
J010246.58-715127.5	–	404	hot pA/R	e	e	e	e?	e	0	0	e	e	0	0	0	0	0	0	0	a?
J010250.06-724022.1	Em[8]	1623	hot pA/R	e	e	e	0	e	0	0	e	e	0	0	e	e	e	0	0	e
J010318.52-721213.4	FIR[6], I60[7]	4081	YSO	e	e	e:	0	e	0	0	e	e?	e?	0	0	0	0	0	0	e:?
J010505.75-715942.8	G [12]	745	YSO	e	e	e	0	e	0	e?	e	e	0	e?	0	0	0	0	0	e?
J010525.79-715858.5	–	221	hot pA/R	e	e	e	0	e	0	e?	e	e	e	e	0	0	0	0	0	0
J010528.61-715942.7	–	987	YSO	e	e	e	e	e	e	e	e	e	e?	e?	0	0	0	0	0	e
J010546.40-714705.2	21 μm source[13]	4106	hot pA/R	e	e	e	e	e	e	e	e	e	0	0	e	e	e	0	0	e
J010603.22-724931.3	–	3485	hot pA/R	e	e	e	0	0	a?	0	e?	e?	0	0	0	0	0	0	0	e
J010619.56-715559.4	–	1396	YSO	e	e	e:	0	e	0	0	e	e	0	0	0	0	0	0	0	0
J010640.30-731024.6	Em [8, 9]	14 998	hot pA/R	e	e	a	0	0	a	0	0	0	0	0	e	e	e	0	0	e
J010710.99-723503.7	–	271	hot pA/R	e	e	e	0	e	0	e?	e	e	0	0	0	0	0	0	0	0
J010722.82-723334.0	Em[8]	1267	YSO	e	e	e	0	e?	0	0	e	e	0	0	0	0	0	0	0	e
J010832.86-715941.2	Em[8]	2716	YSO	e	e	e	0	e	0	e?	e	e	0	0	0	0	0	0	0	e
J010834.02-715900.5	Em[8]	1503	hot pA/R	e	e	e	e	e	e	e	e	e	0	0	0	e	0	0	0	e
J011029.10-725338.2	Em[3, 8]	766	hot pA/R	e	e	e	0	e	0	0	e	e	e	e	0	0	0	0	0	e
J011045.12-722137.5	Em[8]	3699	hot pA/R	e	e	e	0	e	0	e	e?	e?	0	0	0	0	0	0	0	e
J011341.19-725049.8	Em[8]	3171	hot pA/R	e	e	e	0	e?	0	0	0	0	0	0	0	0	0	0	0	e
J011404.66-731658.3	FIR[6]	20 140	YSO	e	e	e	0	e	0	0	e	e	e?	e?	0	0	0	0	0	e
J011417.81-731210.6	–	567	hot pA/R	e	e	a:?	0	e	0	0	e	e	0	e?	0	0	0	0	0	e
J011542.86-730959.3	FIR[6], Em[8]	5125	hot pA/R	e	e	e	0	e	0	0	e?	e?	0	0	0	0	0	0	0	e
J011545.85-732040.3	–	2241	hot pA/R	e	e	e	0	e	0	e?	0	0	0	0	0	0	0	0	0	e
								Previously identified YSOs												
J004456.37-731010.8	FIR[6], IR[12], YSO[14] I60[7], H II[8, 12], I12[19]	28 083	YSO	e	e	e	e	e	e	e	e	e	e	e	o	0	0	0	0	e
J005043.26-724656.0	YSO[14]	5634	YSO	e	e	e	0	e	0	e	e	e	e	e	0	0	0	0	0	e
J005058.10-730756.6	Em[8],YSO[14]	1936	YSO	e	e	e:	0	e	0	0	e	e	0	0	0	0	0	0	0	e
J005238.82-732623.9	YSO[14]	6105	YSO	e	e	e	0	e	0	e	e	e	e	e	0	0	0	0	0	e
J005606.40-722827.9	Em[8],YSO[14]	2267	YSO	e	e	e	0	e	e?	e?	e?	e?	0	0	0	0	0	0	0	e
J010549.29-715948.4	I25[4], FIR[6], YSO[14]	11 423	YSO	e	e	e	0	e	0	0	e	e	e?	e?	0	0	0	0	0	e?

Notes. In the table, 'hot pA/R' represents hot post-AGB/RGB candidates; $L_{obs}/L_{\odot}$ is computed by integrating under the flux distribution at observed wavelengths. A positional cross-matching was performed with all the catalogues mentioned in Table 4. A positional matching was found with the following catalogues: [1]Loup et al. (1997), [2]Morgan & Good (1985), [3]Morgan (1995), [4]Wilke et al. (2003) (25 μm), [5]Wilke et al. (2003) (100 μm), [6]Boyer et al. (2011), [7]Wilke et al. (2003) (60 μm), [8]Meyssonnier & Azzopardi (1993), [9]Murphy & Bessell (2000), [10]Lagadec et al. (2007), [11]Jacoby & De Marco (2002), [12]van Loon et al. (2010), [13]Volk et al. (2011), [14]Oliveira et al. (2013). Catalogue identifications: PN – planetary nebula; Em*,EmO – object with emission features; G – Galaxy; H II – H II region; IR – Infrared source; I12 – IRAS12 μm source; I25 – IRAS25 μm source; I60 – IRAS60 μm source; I100 – IRAS100μ source, YSO – Young stellar object. The following objects are defined in Boyer et al. (2011): FIR – far-IR object, RGB – red giant branch star, x-AGB – dusty AGB star with superwind mass-loss.

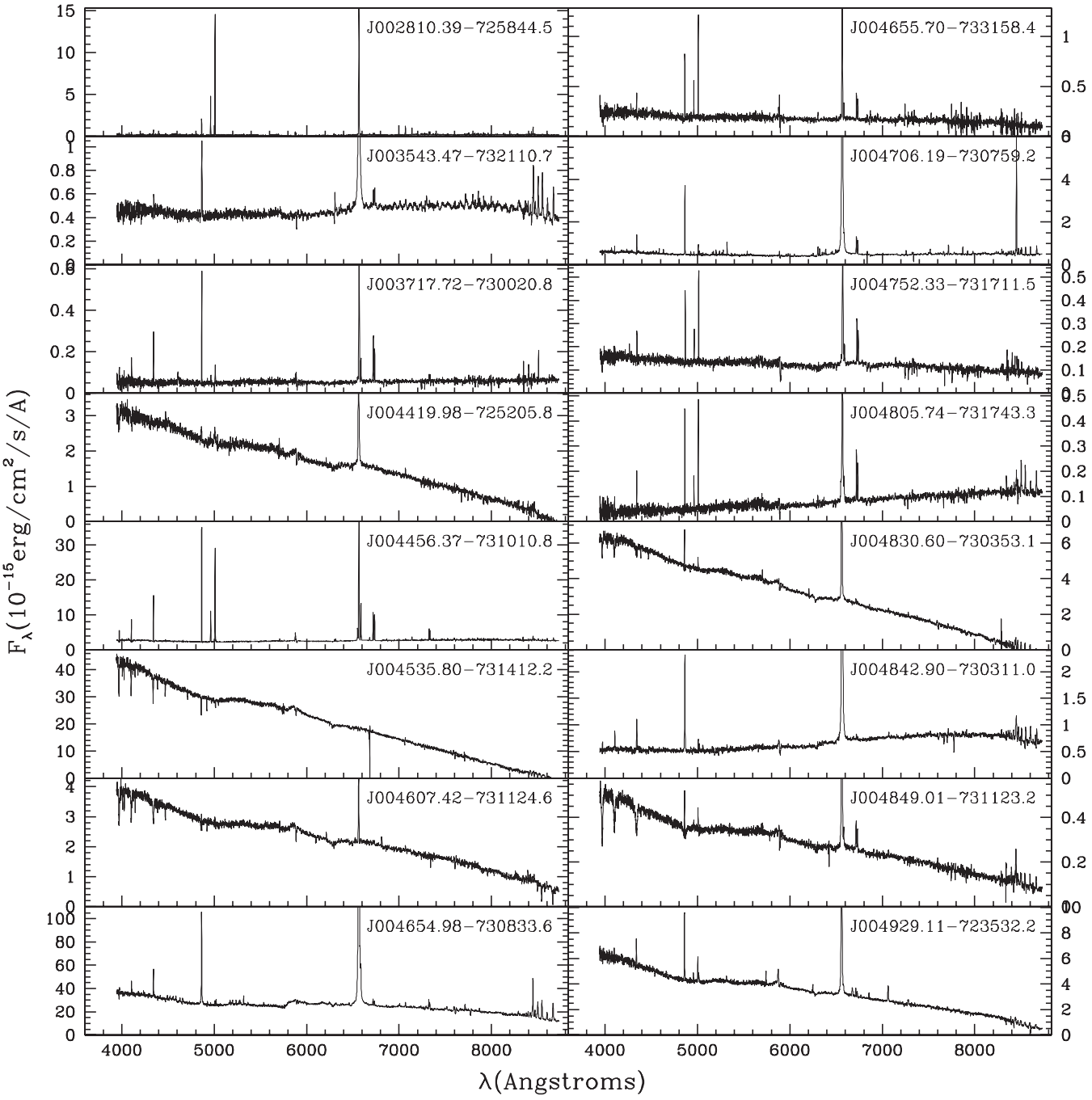

Figure A1. The low resolution AAOmega optical spectra for the sample of probable hot post-AGB/RGB and YSO candidates with emission features and a UV continuum. The spectra are ordered by RA.

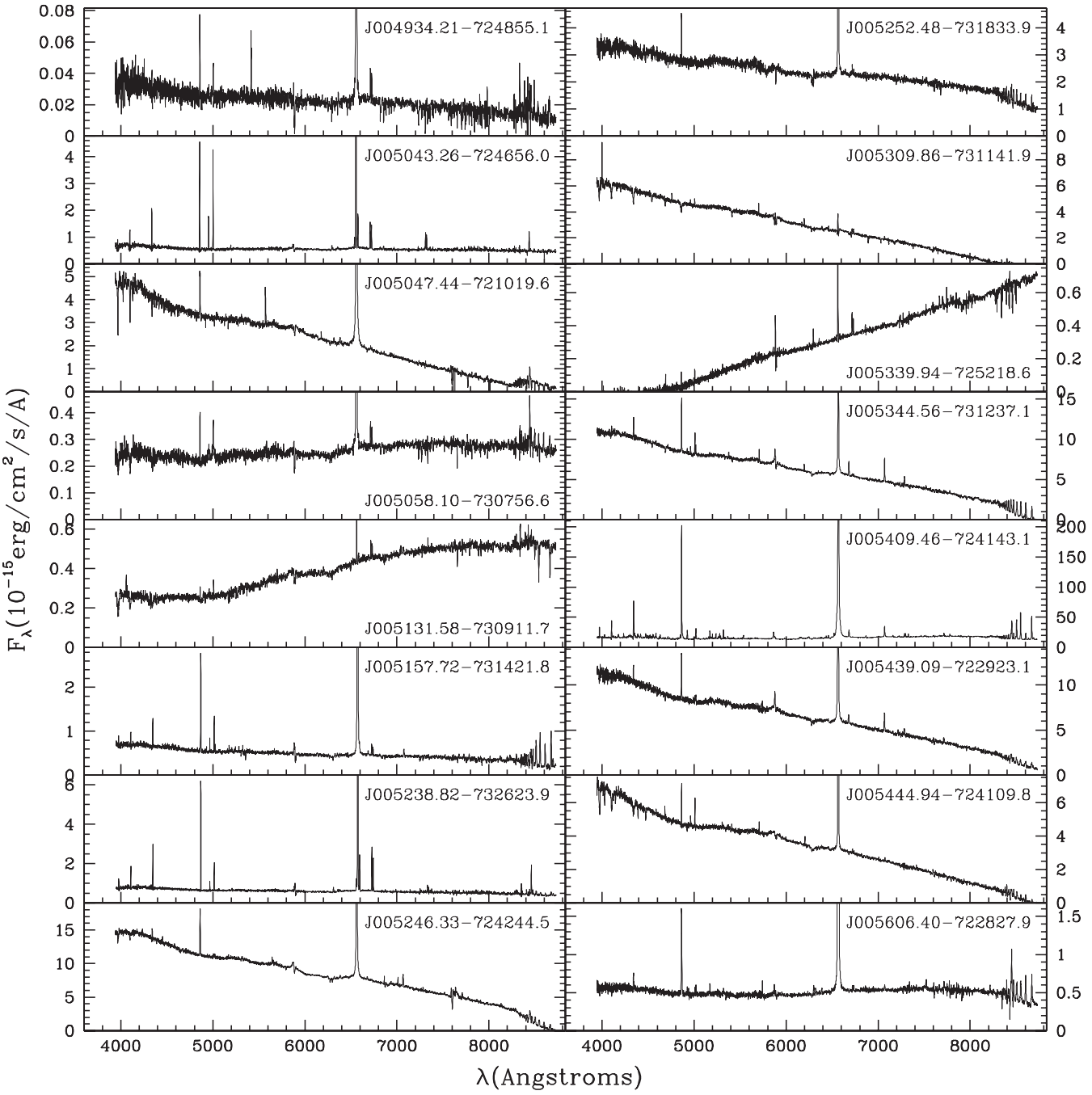

Figure A1 – *continued*

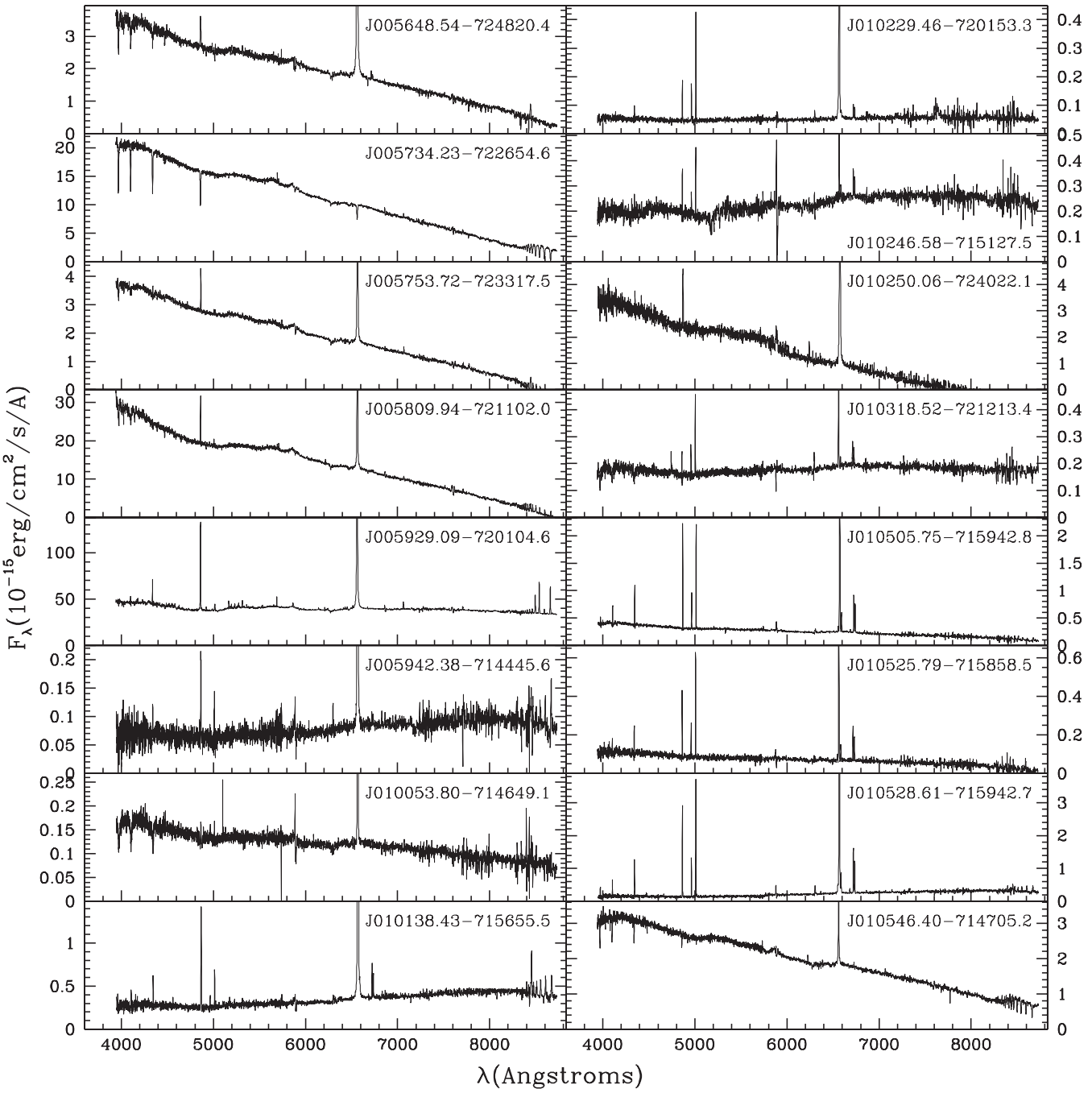

Figure A1 – *continued*

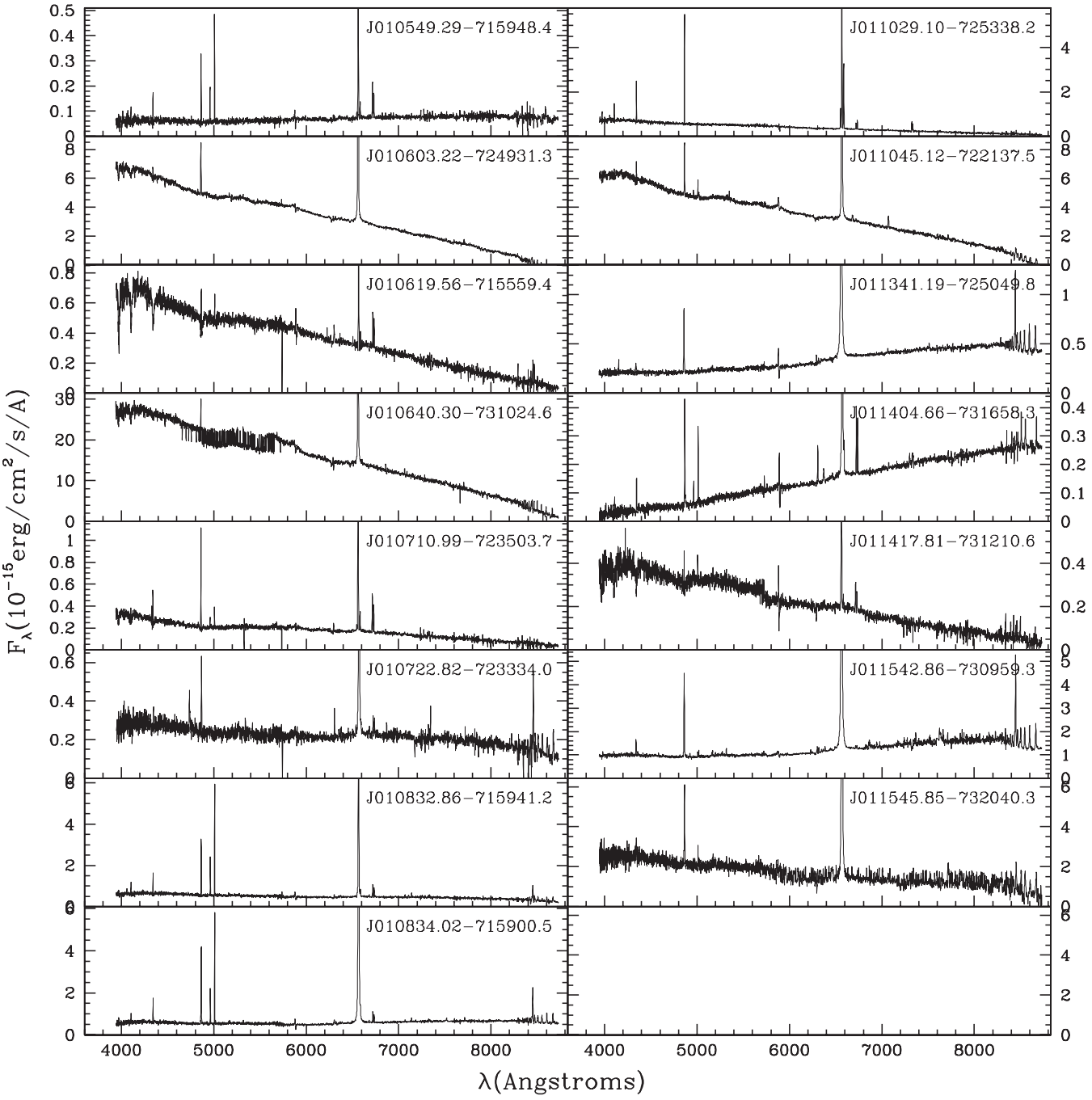

Figure A1 – *continued*

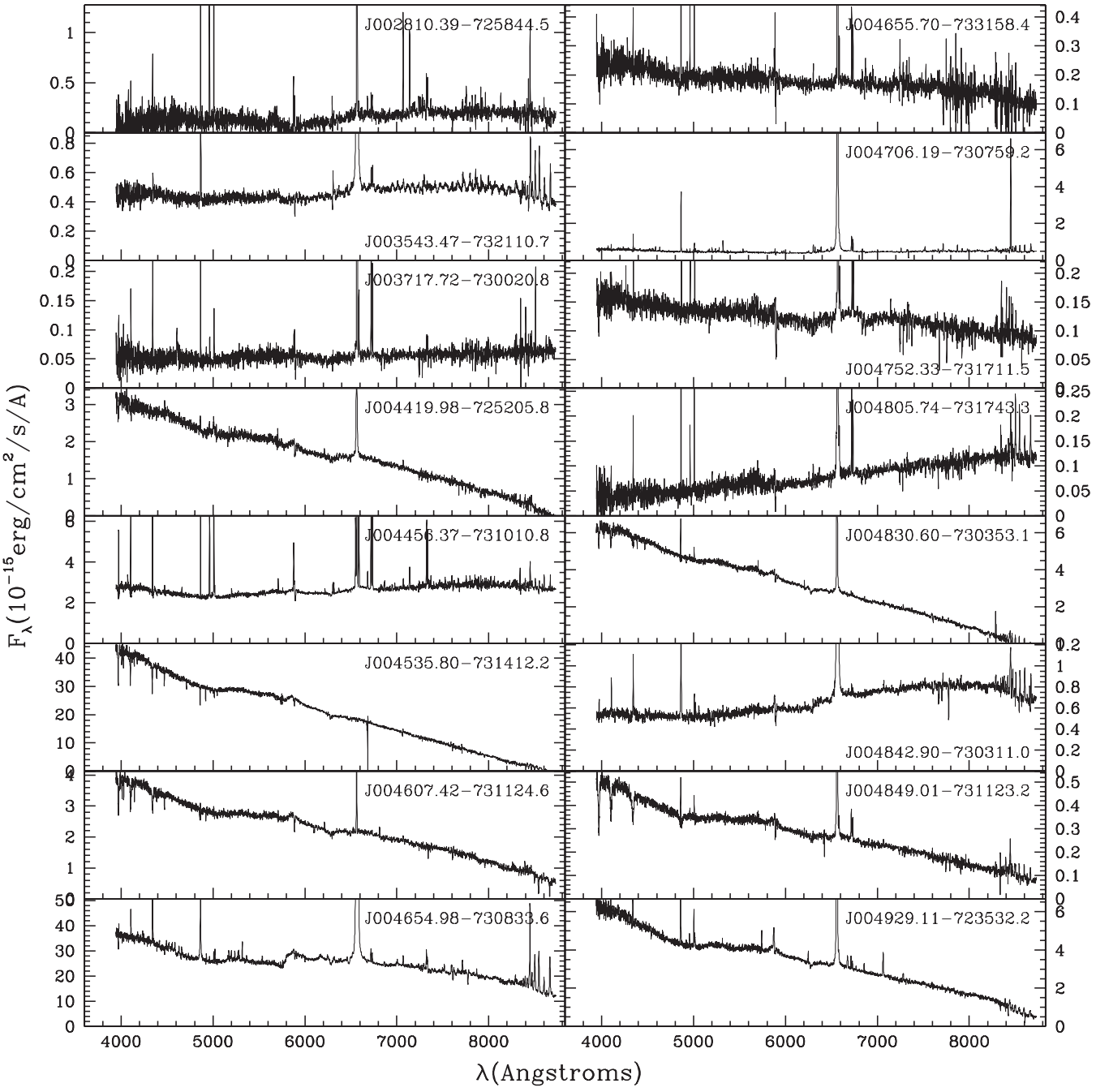

Figure A2. Same as Fig. A1 but scaled to show the continuum. Note that for some objects the spectra of the region >7000 Åis dominated by noise introduced during sky subtraction. The emission feature near the sodium doublet is an artefact of the data reduction process resulting from poor sky subtraction of the sodium doublet emission from the SMC, Galaxy and the night sky.

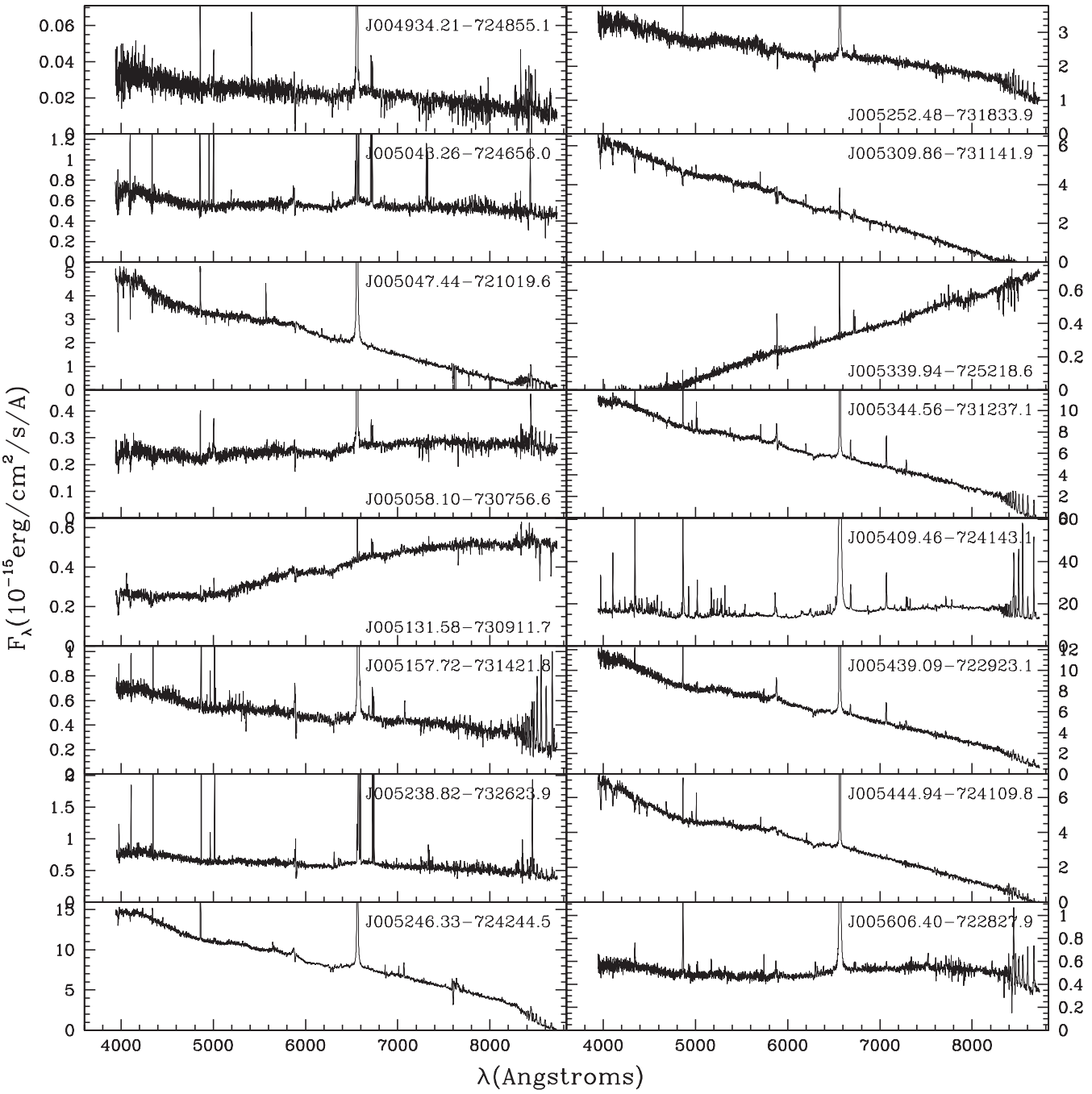

Figure A2 – *continued*

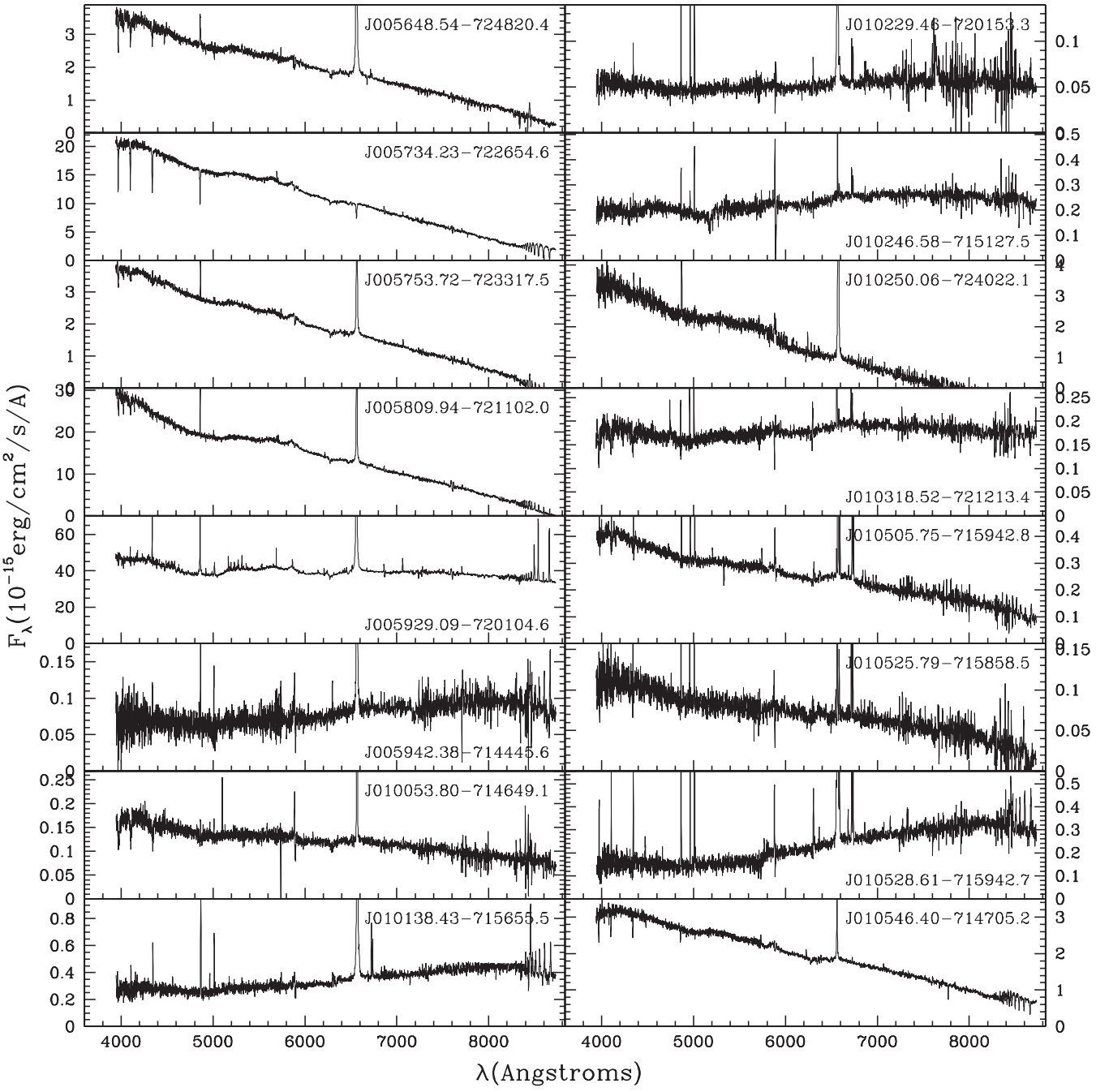

Figure A2 – *continued*

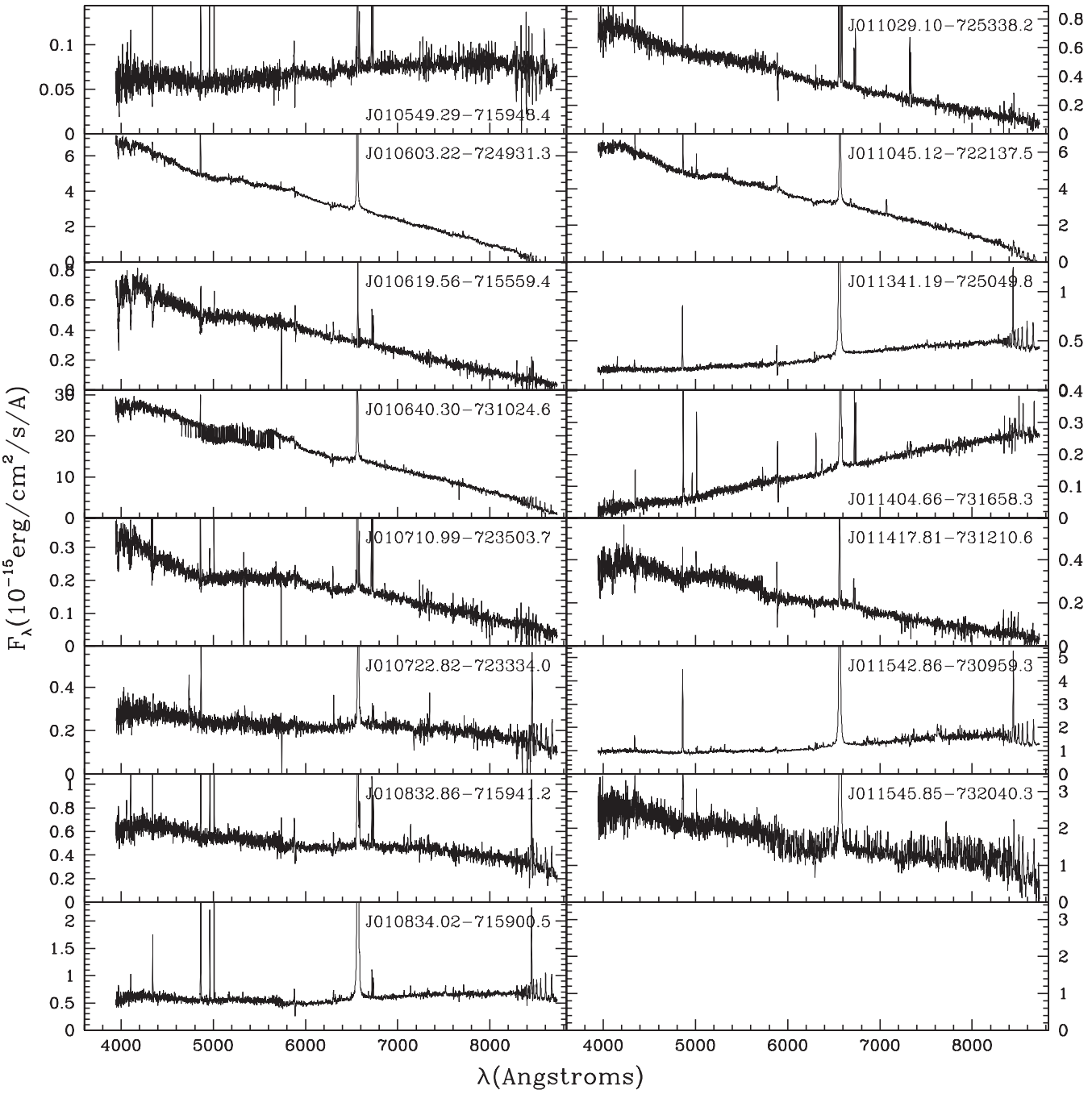

Figure A2 – *continued*

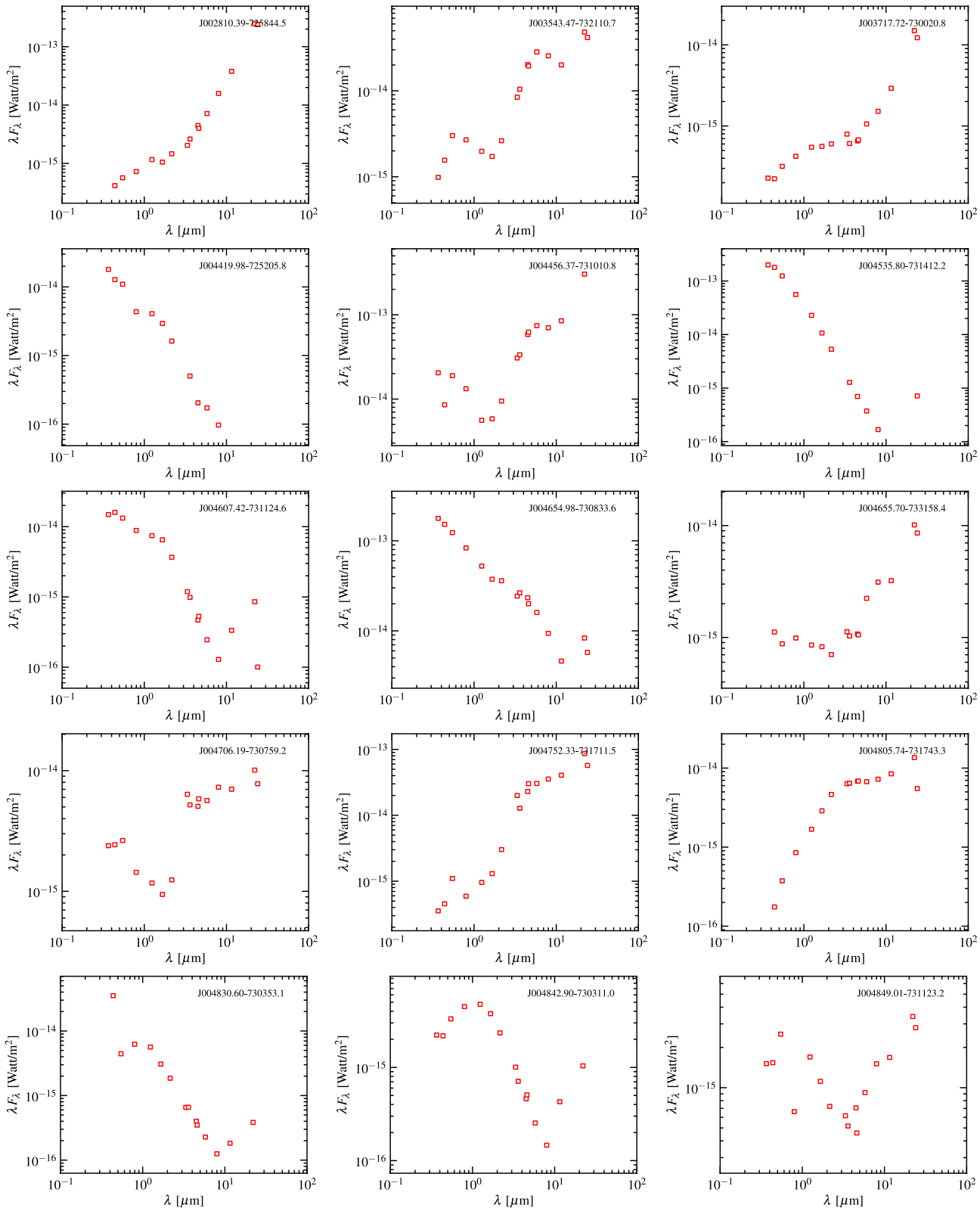

Figure A3. SEDs of the hot post-AGB/RGB and YSO candidates with strong emission lines and in some cases a significant UV continuum. The red open squares represent the original broad-band photometry. The SED plots also show the name of the individual object. The SEDs are ordered by RA.

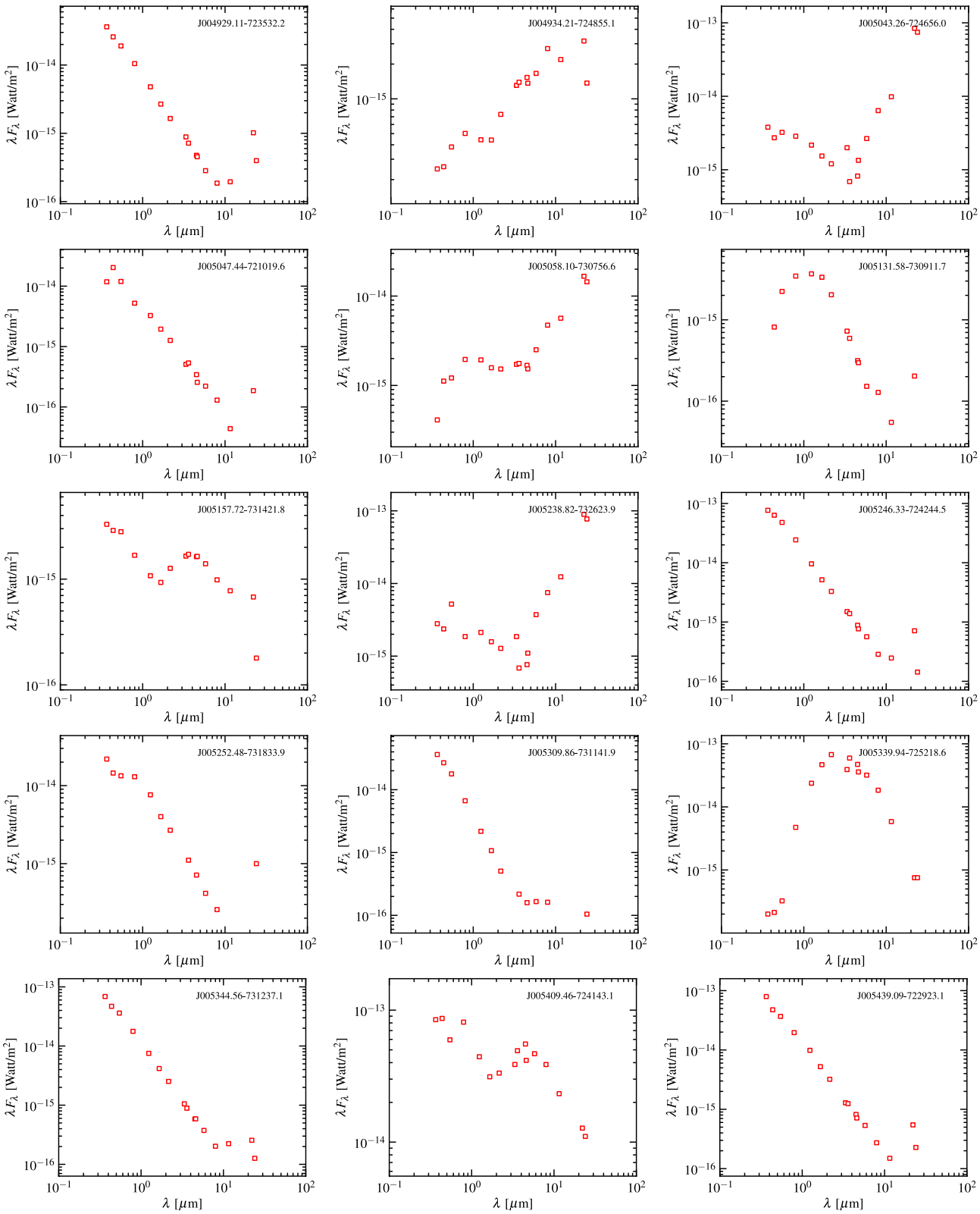

Figure A3 – *continued*

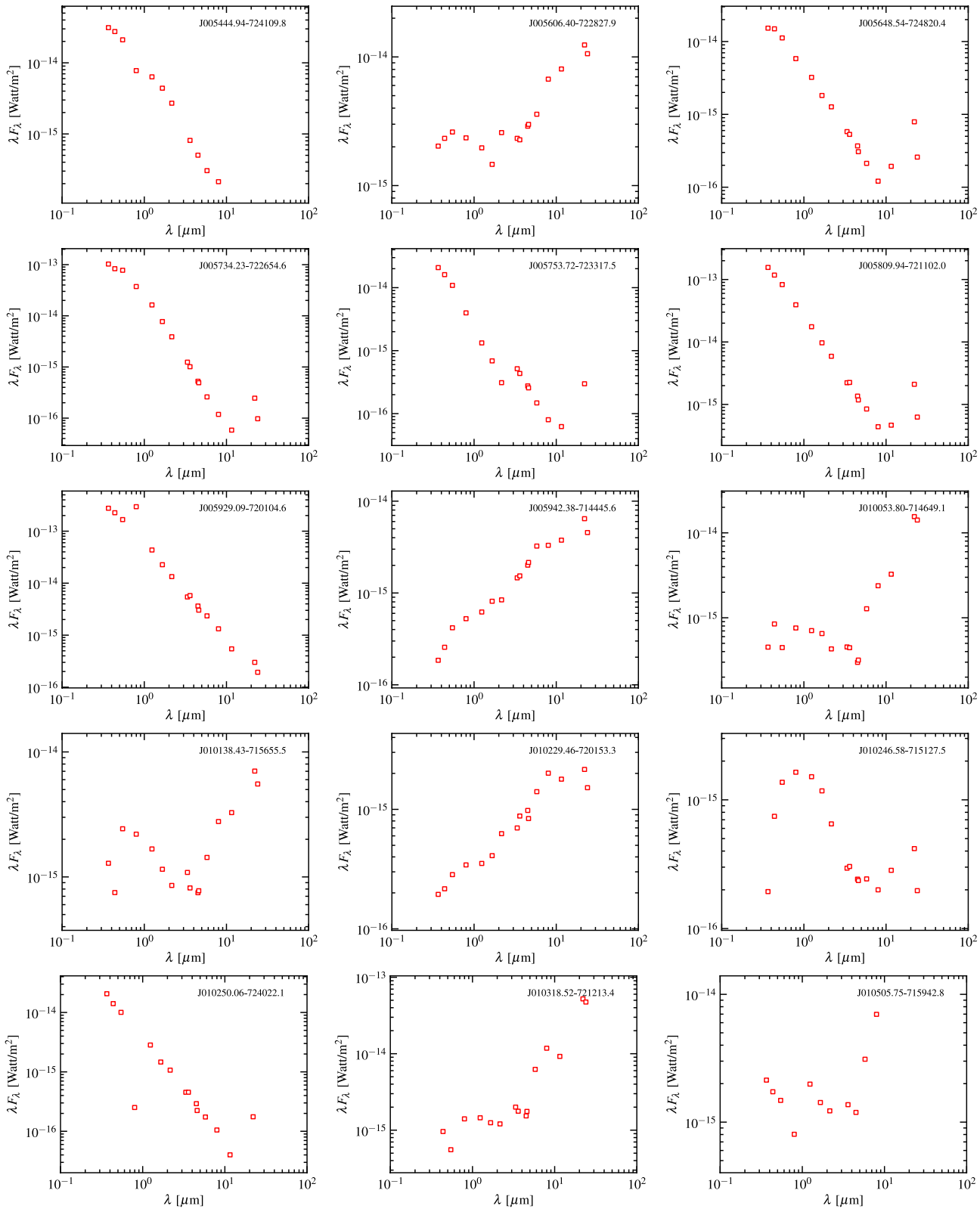

Figure A3 – *continued*

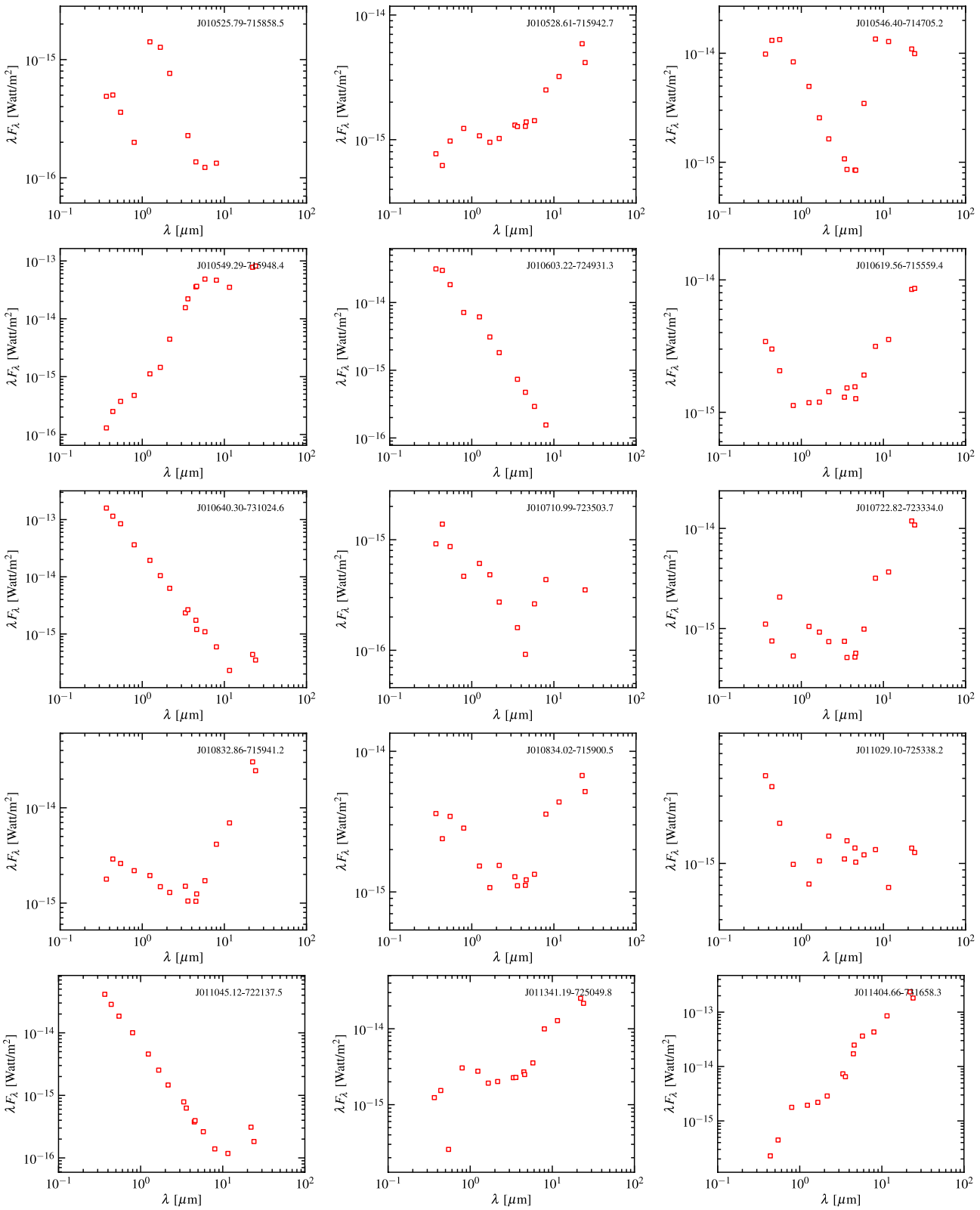

Figure A3 – *continued*

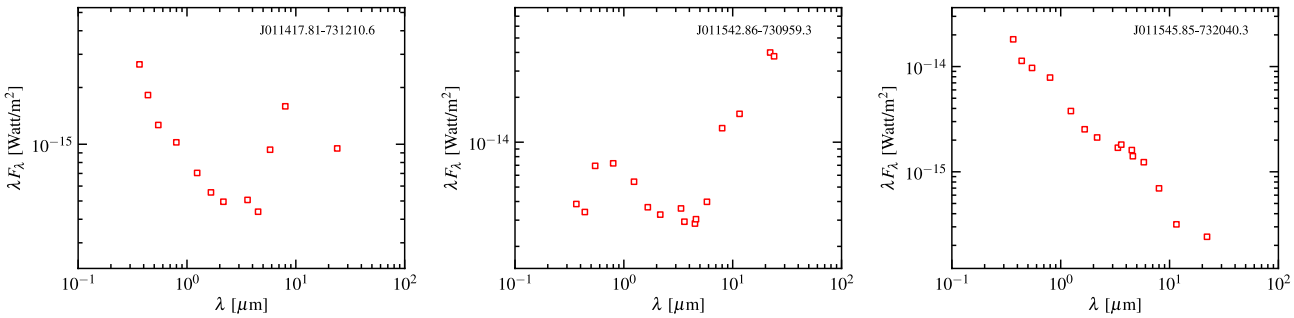

Figure A3 – *continued*

APPENDIX B: TABLES OF THE PN, C-STARS AND M-STARS IN OUR SAMPLE

Table B1. The M-stars in our sample.

Name	Name	Name	Name
J003152.34-721801.0	J003953.87-725124.2	J004121.40-725015.1	J004345.89-722337.5
J004348.97-733110.8	J004451.17-715557.0	J004535.62-721036.7	J004546.33-733104.2
J004709.37-721050.5	J004715.12-723338.8	J005219.88-721046.2	J005606.25-722452.4
J005754.95-731646.9	J005841.03-742459.6	J010411.22-731825.6	J010808.85-735943.9
J010817.42-722024.7	J010902.22-712410.2	J011321.97-724520.1	J011516.49-731143.4

Table B2. The C-stars in our sample.

Name	Name	Name	Name
J003552.00-725834.2	J004702.94-740032.3	J005442.40-742746.1	J010146.23-731125.3
J003633.21-735040.9	J004705.26-723430.4	J005448.70-720153.5	J010149.96-734032.0
J003635.58-733552.2	J004713.71-732153.2	J005449.07-723430.5	J010225.78-735034.2
J003647.96-731830.7	J004714.54-732327.2	J005454.11-725117.0	J010233.40-735754.7
J003744.45-741223.8	J004718.08-723704.4	J005459.64-733958.6	J010241.01-723900.0
J003755.00-721852.0	J004744.15-731643.9	J005505.65-711431.3	J010252.47-725418.9
J003819.73-735811.4	J004816.89-724859.3	J005515.82-725749.1	J010308.49-731717.9
J003830.89-733113.9	J004822.93-734104.7	J005526.57-724514.2	J010315.06-732307.9
J003905.60-724715.8	J004859.45-733538.6	J005530.74-732754.0	J010337.61-714939.1
J003913.22-735705.9	J004903.79-730519.6	J005544.42-725440.7	J010404.96-715325.1
J004010.18-730039.6	J004931.46-730715.5	J005559.90-723025.4	J010419.07-734014.4
J004024.50-742424.8	J005016.58-732517.6	J005606.14-720431.8	J010442.50-720154.8
J004035.42-741120.1	J005023.29-740735.4	J005617.49-722704.2	J010449.69-723706.1
J004100.00-722528.1	J005031.25-722913.0	J005635.44-713233.2	J010525.11-743213.4
J004152.00-730827.4	J005044.35-723739.0	J005645.11-712623.2	J010532.11-720141.4
J004156.75-730728.9	J005101.97-725925.3	J005705.78-741316.4*	J010613.22-742420.4
J004210.62-735003.5	J005108.11-731342.4	J005710.92-723059.9	J010617.23-722424.5
J004216.95-733850.5	J005109.23-731933.2	J005720.49-731245.9	J010653.02-734600.1
J004221.72-722405.6	J005113.84-721714.4	J005732.74-722005.1	J010716.65-731724.8
J004239.07-724642.8	J005116.18-713855.1	J005742.47-723718.5	J010720.13-724359.1
J004248.70-734522.4	J005222.26-730944.6	J005748.96-730521.5	J010740.35-721537.5
J004308.69-734825.1	J005229.38-722557.7	J005758.16-725620.6	J010812.94-725243.8
J004325.12-721851.1	J005233.40-725409.5	J005809.47-725023.4	J010828.25-723643.6
J004339.51-731457.0	J005234.70-720826.9	J005835.16-725935.6	J010828.79-720807.9
J004345.74-742215.2	J005235.32-731749.3	J005900.39-730021.7	J010925.78-722031.0
J004417.52-733441.2	J005241.15-731220.4	J005936.60-722716.9	J010928.89-722821.2
J004456.97-730555.4	J005310.07-721154.6	J005941.63-731018.7	J010935.05-731459.4
J004522.31-741620.9	J005313.97-731517.3	J005951.31-732712.6	J011014.44-731415.9
J004534.30-722809.9	J005338.82-733318.9	J005958.75-720300.9	J011053.17-721446.0
J004608.33-734725.9	J005353.50-733323.5	J010010.43-713613.8	J011123.43-724318.6
J004614.25-732137.4	J005353.54-734402.8	J010020.83-730648.4	J011136.36-724726.6
J004617.88-720006.0	J005354.98-722631.9	J010021.17-741958.3	J011140.46-731539.7
J004626.21-730136.1	J005402.65-725330.4	J010024.23-714926.4	J011246.96-720758.1
J004641.36-725125.3	J005408.46-721420.3	J010111.31-722827.9	J011451.00-730127.2
J004658.55-724407.4	J005410.74-730303.0	J010144.14-731742.1	J011914.67-733240.1

Notes. *J005705.78-741316.4 has been previously identified as a symbiotic C-star by Belczyński et al. (2000) which is confirmed by our low-resolution spectrum showing a photosphere of a C-star with strong emission lines.

Table B3. The new and previously known PN candidates in our sample. In this table, 'a' represents absorption, 'e' represents emission, '0' indicates that the feature is not observed.:' indicates that there is some line blending that has taken place or there is an absorption line with an emission core or the line indicates signs of strong winds and therefore mass-loss. '?' represents that the nature of the spectral line is uncertain. 'p' indicates a P-Cygni line profile. Note: the low-resolution of the spectra could possibly affect the identification of a given line.

Name	Previous identification	Hα	Hβ	Hγ	[O III]	[O III]	He I	He I	[S II]	[S II]	[N II]	[N II]	Ca II	Ca II	Ca II	Li	Ba	Pa
Wavelength (Å)		6563	4861	4341	4659	5007	4471	5876	6717	6731	6548	6584	8498	8542	8662	6708	4554	–
Previously uncatalogued PNe																		
J004538.33-730438.0	–	e	e	e	0	e	0	e	e	e	e	e	0	0	0	0	0	0
J004641.35-730613.1	FIR[1]	e	e	e	0	e	0	e	e	e	e	e	0	0	0	0	0	e
J004825.75-730556.4	YSO[2], Em[3, 4]	e	e	e	0	e	0	e	e	e	e	e	0	0	0	0	0	e
J004836.45-725800.6	FIR[1], I25[5], I60[6]	e	e	e	e	e	e	e	e	e	e	e	0	0	0	0	0	e
J005027.18-725254.6	Em[7]	e	e	e	0	e	e	e	e	e	e	e	0	0	0	0	0	e?
J005058.49-735141.3	I60[6],FIR[1]	e?	e?	e?	0	e?	e?	e	e	e	e	e	0	0	0	0	0	0
J005422.23-724329.7	x-AGB[1]	e	e	e	0	e	0	e	e	e	e	e	0	0	0	0	0	0
J005610.87-721851.4	–	e	e	e	0	e	0	e	e	e	e	e	0	0	0	0	0	0
J005617.17-721756.1	–	e	e	e	0	e	e	e	e	e	e	e	0	0	0	0	0	e
J005706.16-733349.7	–	e	e	e	0	e	e?	e	e	e	e	e	0	0	0	0	0	e?
J005856.88-720954.3	YSOp[8]	e	e	e	0	e	e	e	e	e	0	0	e	e	e	0	0	0
J005905.38-721035.5	FIR[1],I25[5]	e	e	e	e?	e	e	e	e	e	e	e	0	0	0	0	0	e
J005905.81-721127.1	x-AGB[1],Em*[7]	e	e	e	e	e	e	e	e	e	e	e	0	0	0	0	0	e
J005912.20-720958.4	RGB[1],YSOd?[8]	e	e	e	0	e	e	e	e	e	e	e	0	0	0	0	0	e
J010115.32-721637.4	–	e	e	e	e	e	e	e	e	e	e	e	0	0	0	0	0	0
J010155.63-722948.0	–	e	e	e	0	e	e?	e	e	e	e?	e?	0	0	0	0	0	e:?
J010248.21-720615.9	–	e	e	e	0	e	e?	e	e	e	e	e	0	0	0	0	0	e
J010258.73-720347.5	–	e	e	e	0	e	e	e	e	e	e	e	0	0	0	0	0	e?
J010307.48-720218.1	–	e	e	e	0	e	e	e	e	e	e	e	0	0	0	0	0	0
J010322.32-720411.1*	–	e	e	e	0	e	e	e	e	e	e	e	a	a	a	0	0	0
J010336.26-720404.2*	–	e	e	e	0	e	e?	e	e	e	e?	e?	a?	a?	a?	0	0	0
J010405.71-720700.3*	–	e	e	e	0	e	0	e	e	e	e	e	a?	a?	a?	0	0	0
J010442.52-721007.4*	–	e	e	e	e	0	e	0	e	e	e?	e	a?	a?	a?	0	0	0
J010455.13-720055.0	–	e	e	e	e	e	e	e	e	e	e	e	a?	a?	a?	0	0	0
J010458.98-715429.9	–	e	e	e	e	e	e	e	e	e	e	e	0	0	0	0	0	0
J010529.27-720830.6	–	e	e	e	0	e	0	e	e	e	e	e	0	0	0	0	0	0
J010659.66-725042.8	RGB,FIR[1], YSO[2, 9] Em[7]	e	e	e	0	e?	e?	0	e	e	e?	e?	0	0	0	0	0	e
J011347.56-731710.1	–	e	e	e	e	e	e	e	e	e	e	e	0	0	0	0	0	e
J011358.02-731747.4	FIR[1],Em*[7]	e	e	e	0	e	0	e	e	e	0	0	0	0	0	0	0	e
J011447.02-732058.8	RSG[1]	e	e	e	e?	e	e?	e?	e	e	e?	e?	0	0	0	0	0	e?
Previously identified PNe																		
J003238.86-714159.5	PN[10, 11, 12]	e	e	e	0	e	e	e	e	e	e	e	0	0	0	0	0	e
J003421.94-731321.5	PN[10, 12]	e	e	e	e	e	e	e	e	e	e	e	0	0	0	0	0	e
J004121.62-724516.4	PN[7, 10, 12]	e	e	e	e	e	e	e	e	e	e	e	0	0	0	0	0	e
J004127.73-734706.5	FIR[1], PN[7, 10, 12, 13]	e	e	e	e	e	e	e	e	e	e	e	0	0	0	0	0	e
J004325.27-723818.4	PN[7, 10, 12, 14]	e	e	e	e	e	e	e	e	e	e	e	0	0	0	0	0	e
J004353.84-725514.1	PN[7, 11]	e	e	e	0	e	e	e	e	e	e	e	0	0	0	0	0	e
J004947.48-741440.0	PN[11]	e	e	e	0	e	0	e	e	e	e?	e	0	0	0	0	0	e?
J005035.04-734257.9	PN[7, 10, 14]	e	e	e	e	e	e	e	e	e	e	e	0	0	0	0	0	e
J005127.12-722611.6	PN[3, 7, 10, 12, 14]	e	e	e	e	e	e	e	e	e	e	e	0	0	0	0	0	e
J005136.55-732016.9	PN[3, 7, 11, 12, 14]	e	e	e	e	e	e	e	e	e	0	e?	0	0	0	0	0	e
J005142.17-725027.4*	PN[14]	e	e	e	e	e	e	e	e	e	e	e	a	a	a	0	0	0
J005156.30-712444.3	PN[7, 10, 12]	e	e	e	e	e	e	e	e	e	e	e	0	0	0	0	0	e
J005311.04-724507.4	PN[3, 7, 10, 12, 13, 14,	e	e	e	e	e	e	e	e	e	e	e	0	0	0	0	0	e
J005619.40-720658.3	PN[5, 7, 11],I25[15]	e	e	e	e	e	e	e	e	e	e	e	0	0	0	0	0	e
J005639.30-723907.1	PN[3, 7, 11, 14]	e	e	0	0	e	0	0	e	e	0	0	0	0	0	0	0	e
J005842.84-722716.6	PN[7, 12, 14, 15]	e	e	e	e	e	e	e	e	e	e	e	0	0	0	0	0	e

Notes. '*' – indicates that these objects are likely to be symbiotic stars as their spectra show a photosphere of a cool star with a red continuum and strong emission lines.

Previous identifications: YSOd – Definite YSO; YSOp – Probable YSO; Em*, EmO – object with emission features; I25 – I 25 μm source; I60 – I 60 μm source; PN – Planetary nebula; FIR – far-IR object; RGB – red giant branch star; RSG – red supergiant, x-AGB – dusty AGB star with superwind mass-loss [defined in Boyer et al. (2011)].

A positional cross-matching was performed with all the catalogues mentioned in Table 4. A positional matching was found with the following catalogues: [1]Boyer et al. (2011), [2]Oliveira et al. (2013), [3]Jacoby (1980), [4]Sanduleak & Pesch (1981), [5]Wilke et al. (2003) (25 μm), [6]Wilke et al. (2003) (60 μm), [7]Meyssonnier & Azzopardi (1993), [8]Simon et al. (2007), [9]van Loon et al. (2010), [10]Sanduleak (1978), [11]Morgan (1995), [12]Murphy & Bessell (2000), [13]Loup et al. (1997), [14]Jacoby & De Marco (2002), [15]Morgan & Good (1985).

APPENDIX C: THE FINAL SAMPLE OF HIGH PROBABILITY POST-AGB/RGB AND YSO CANDIDATES

Figs C1–C4 show the SEDs of the objects before and after de-reddening. Figs C5–C8 show the optical spectra of the sample of Q1 and Q2 post-AGB/RGB and YSO candidates. We have summarized some of the most prominent features in Tables C1–C4.

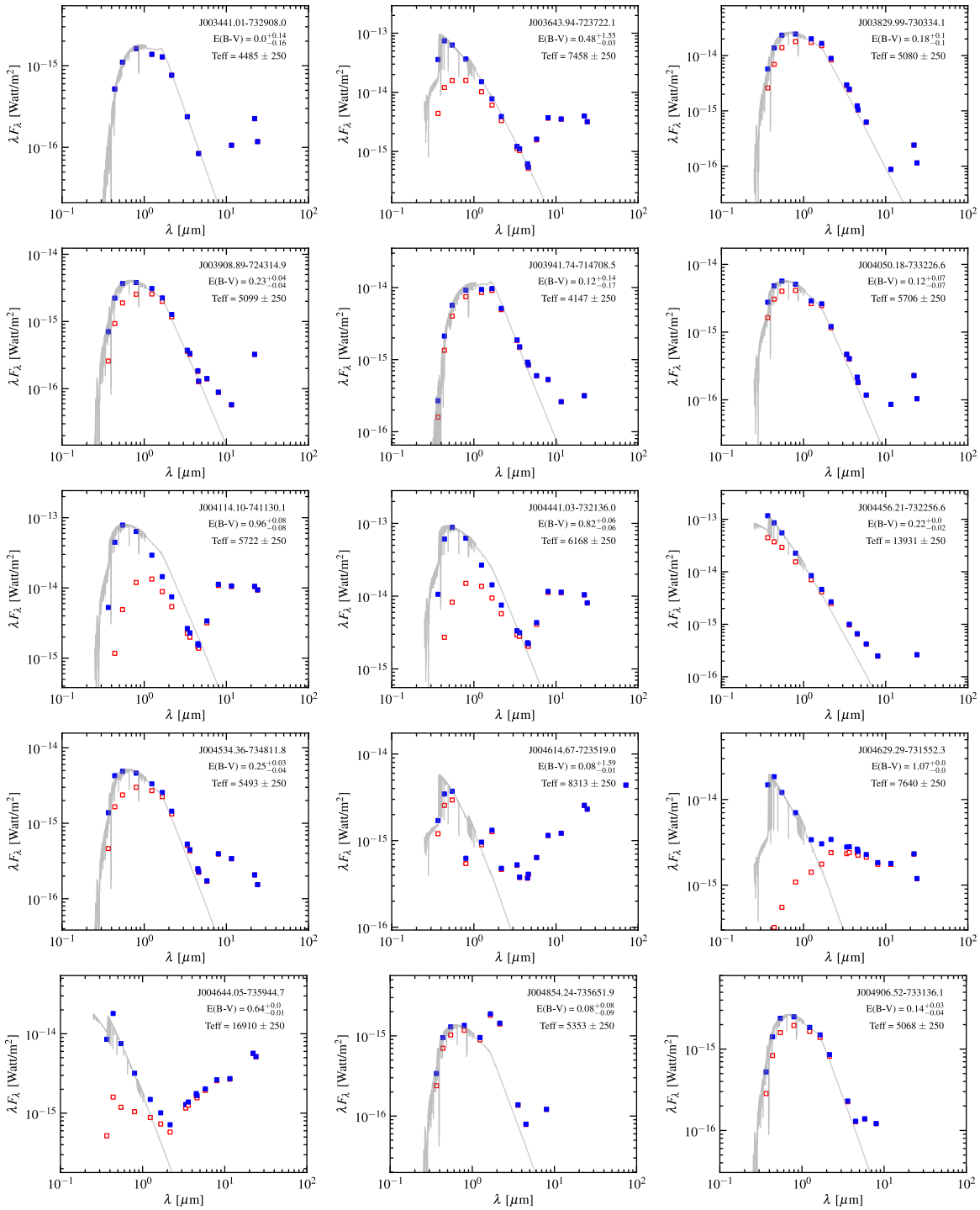

Figure C1. SEDs of Q1 post-AGB/RGB candidates. The red open squares represent the original broad-band photometry. The blue filled squares represent the dereddened broad-band photometry. Up to a wavelength of 10 500 Å, we overplot the Munari synthetic spectrum which is estimated to have the best fit to the observed spectra. The SED distribution in the IR is represented with the corresponding Kurucz atmospheric model take from Castelli & Kurucz (2003). The SED plots also show the name of the individual object, the estimated $E(B-V)$ value with error bars (see Section 5) and the estimated $T_{\rm eff}$ value (see Section 4).

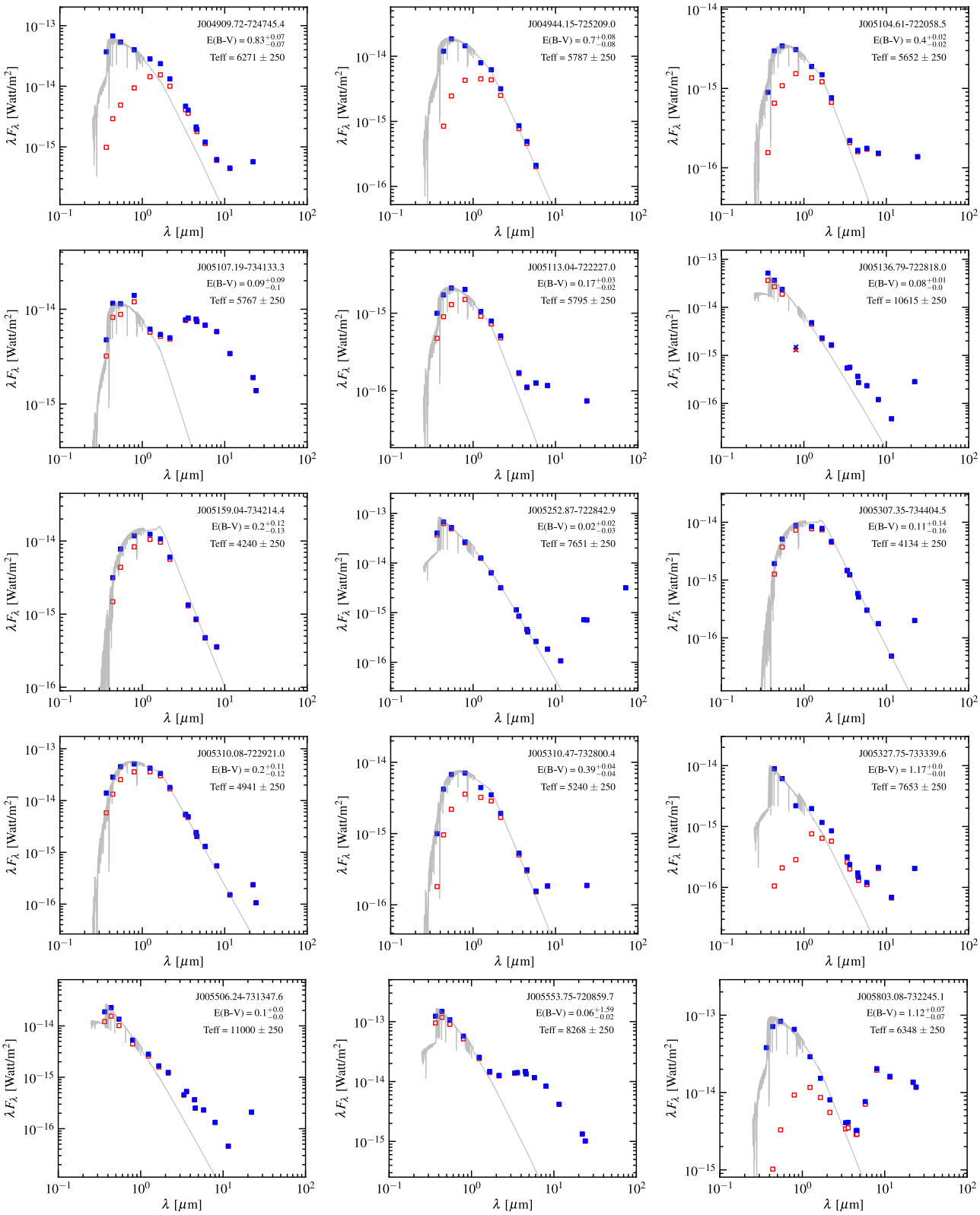

Figure C1 – *continued*

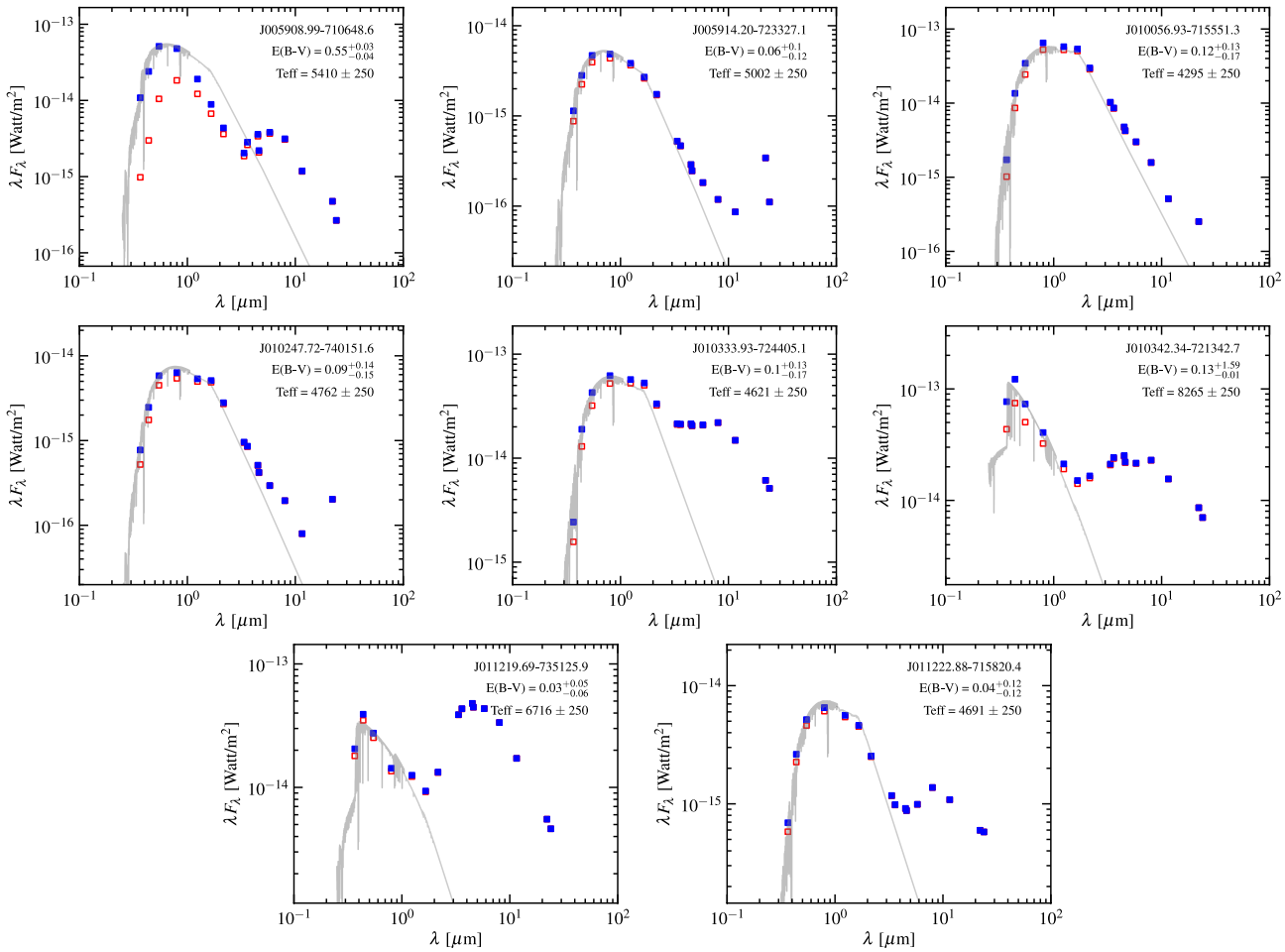

Figure C1 – *continued*

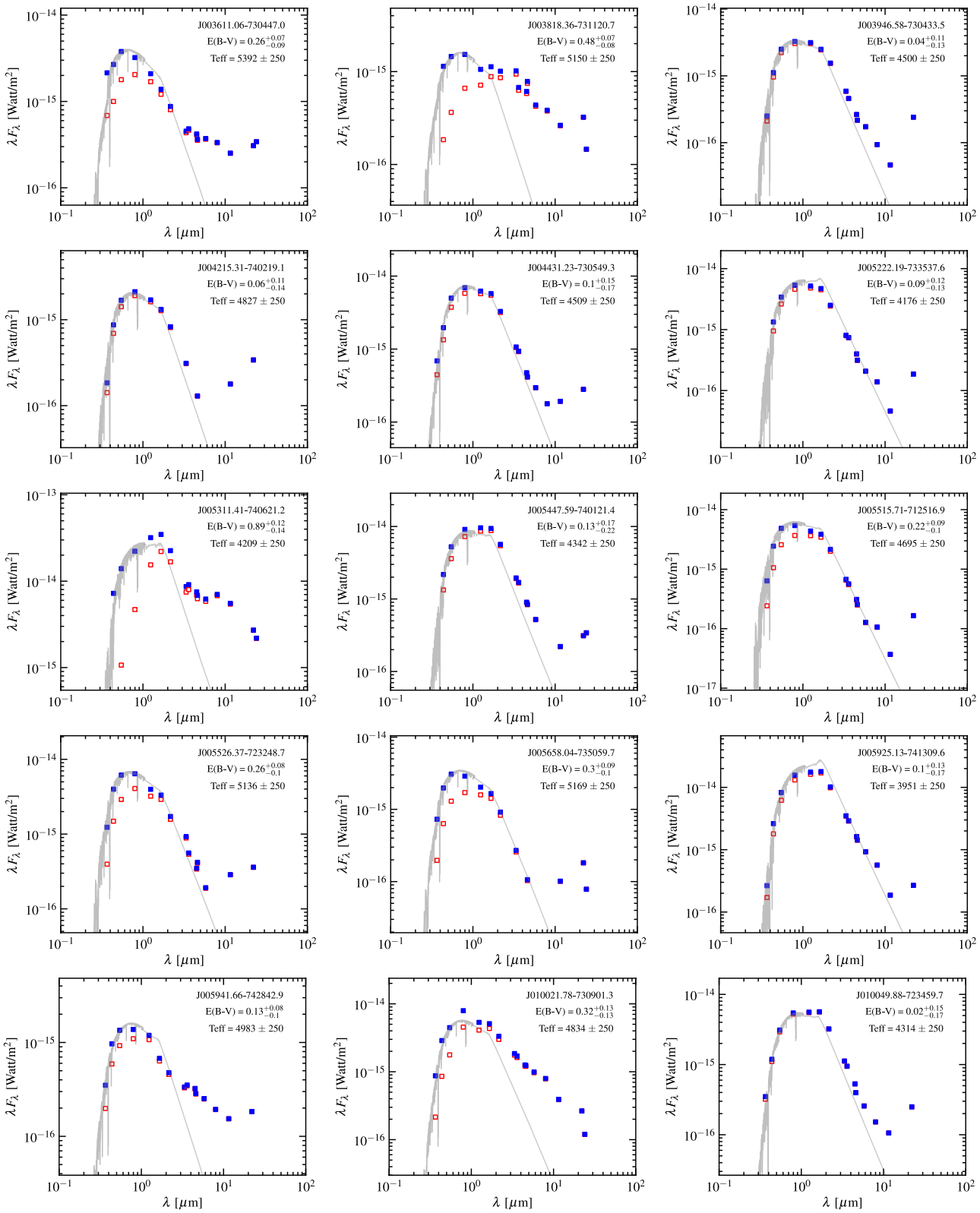

Figure C2. Same as Fig. C1, but for the Q2 post-AGB/RGB candidates.

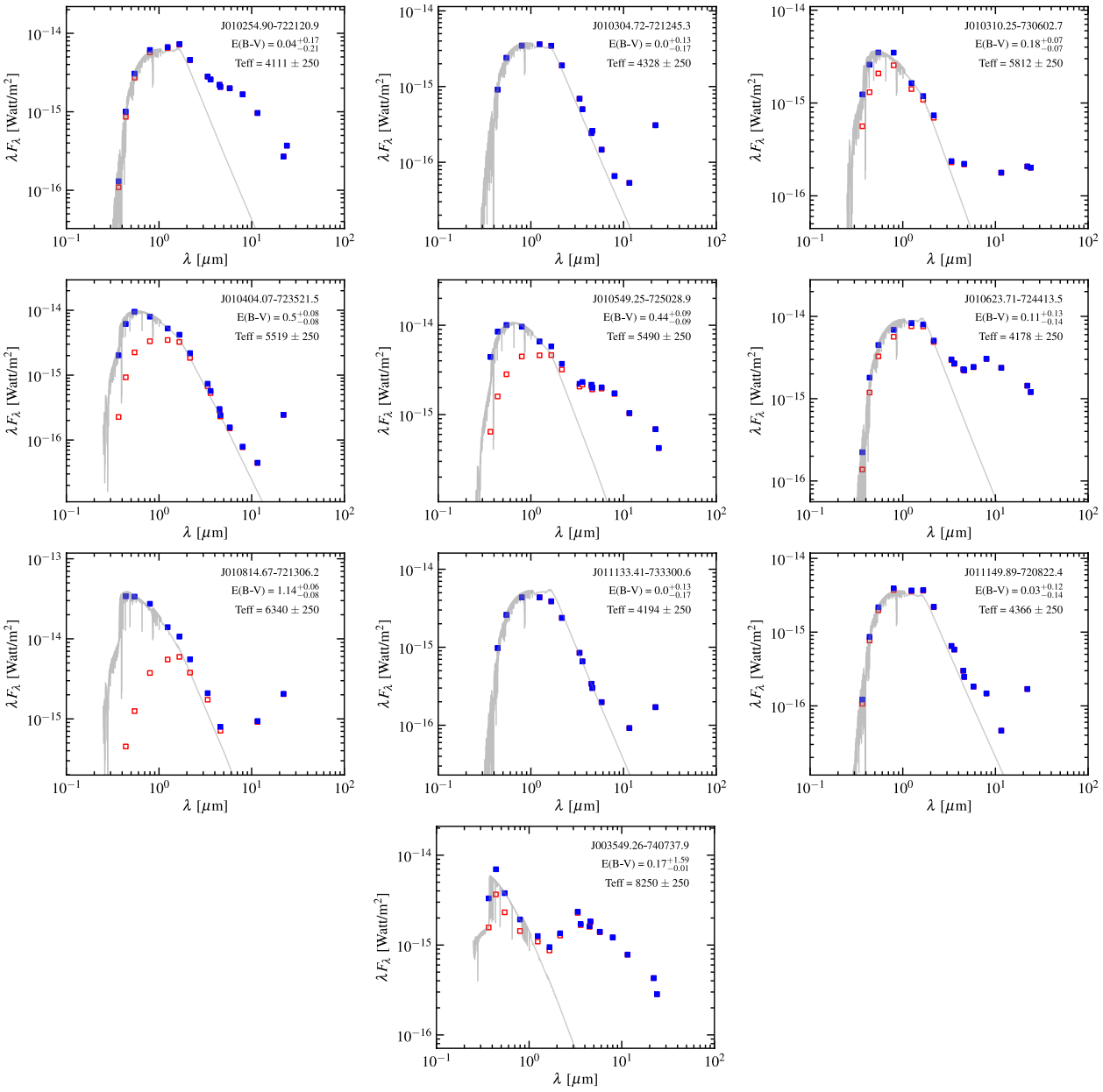

Figure C2 – *continued*

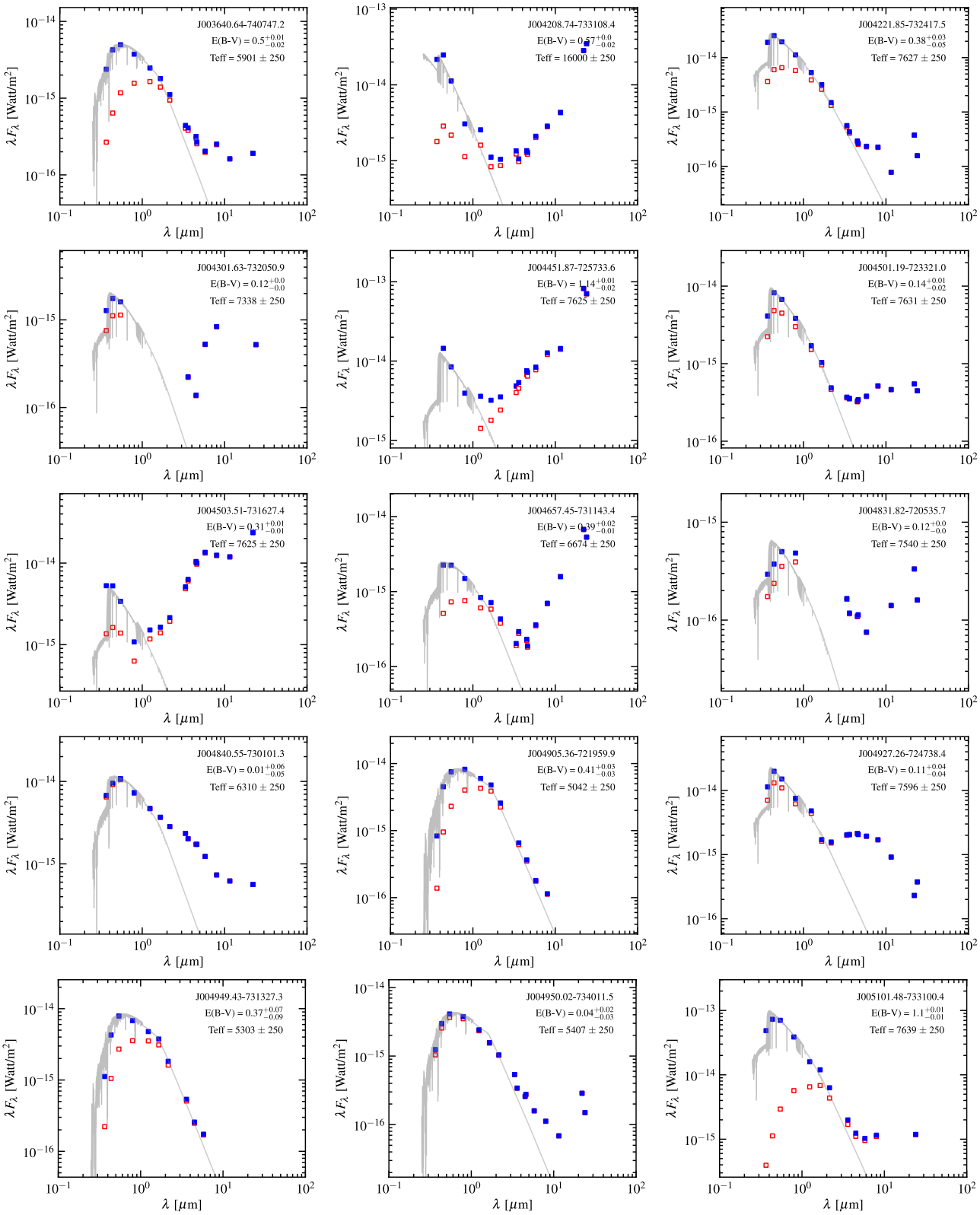

Figure C3. Same as Fig. C1, but for the Q1 YSO candidates.

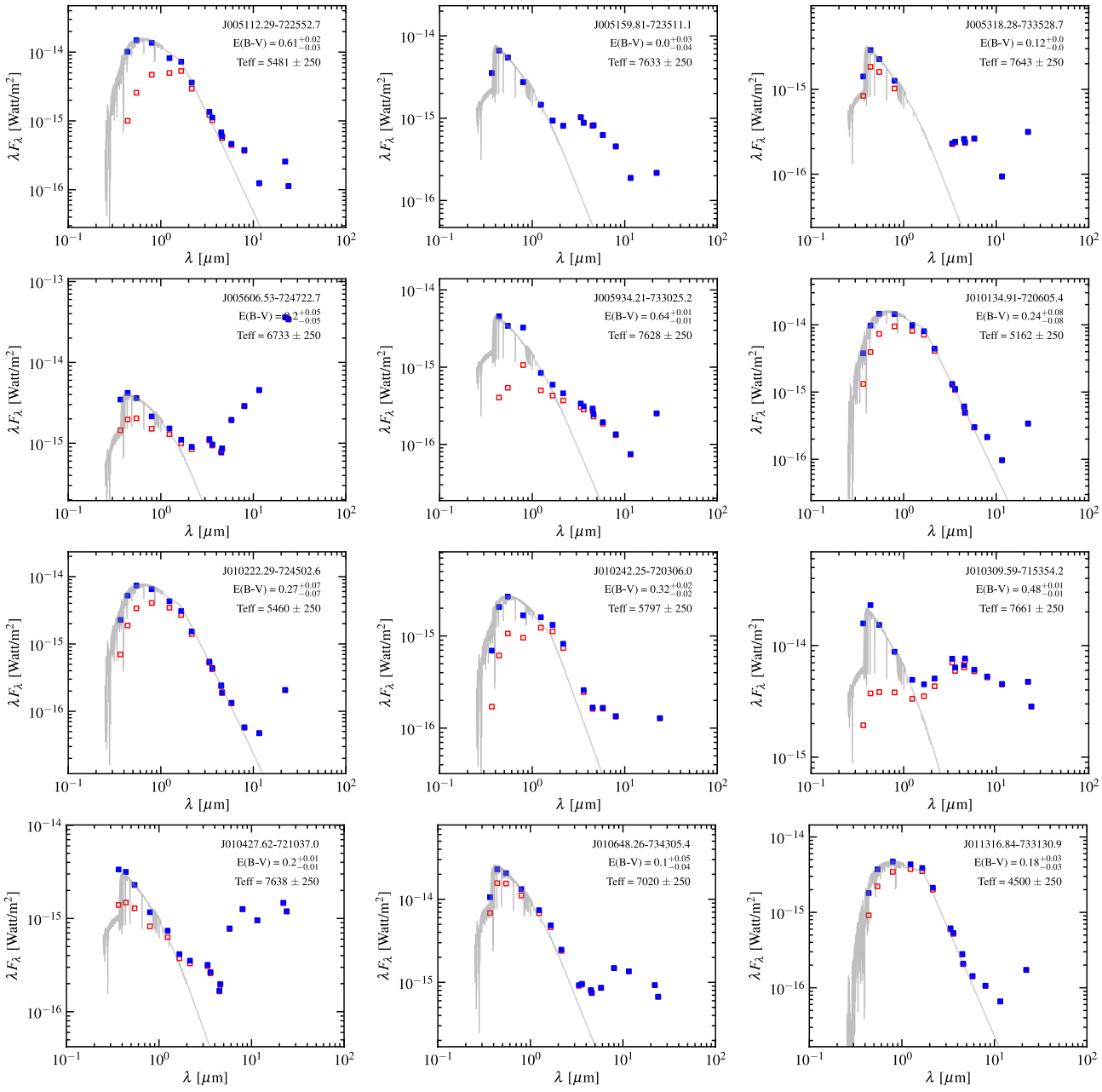

Figure C3 – *continued*

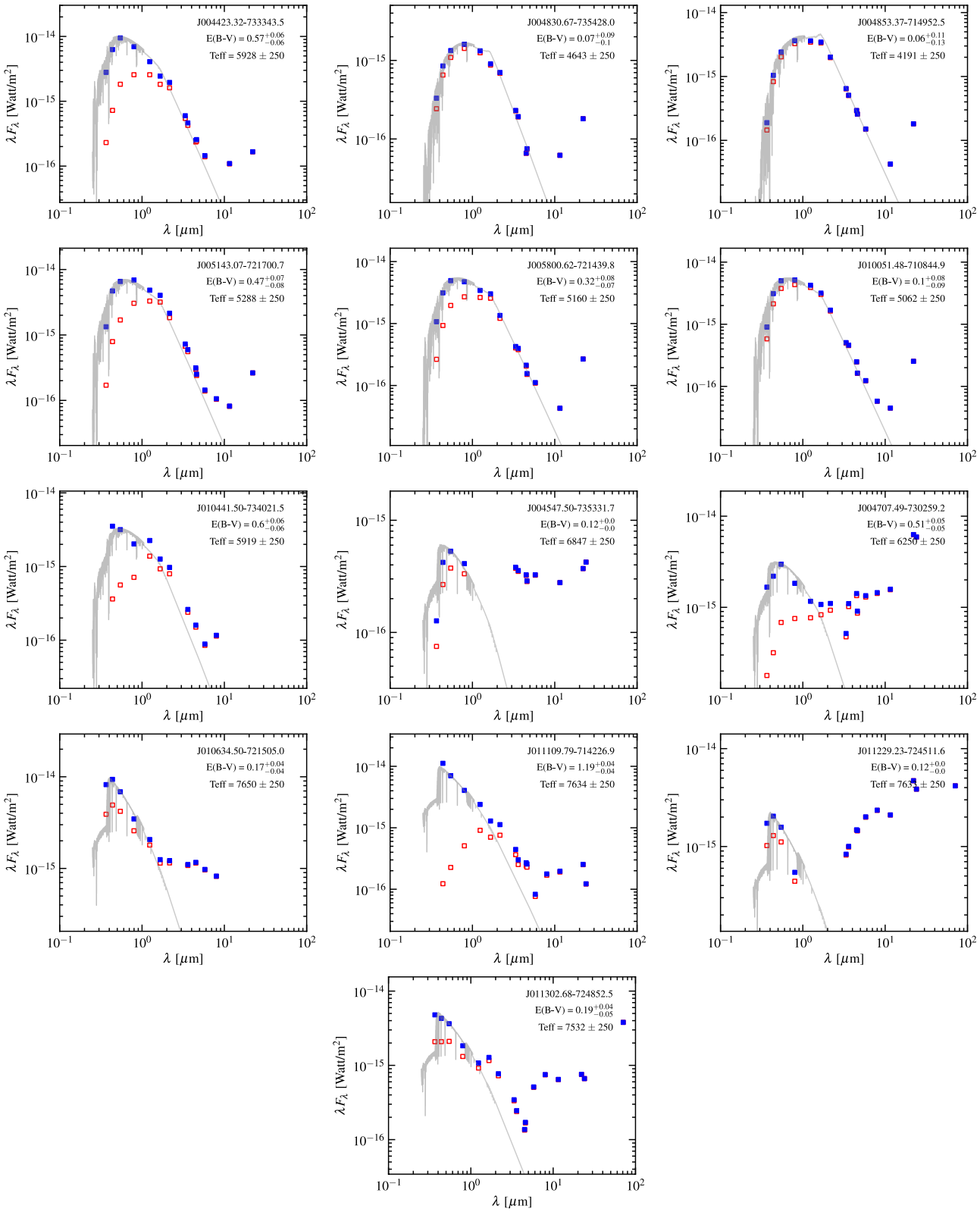

Figure C4. Same as Fig. C1, but for the Q2 YSO candidates.

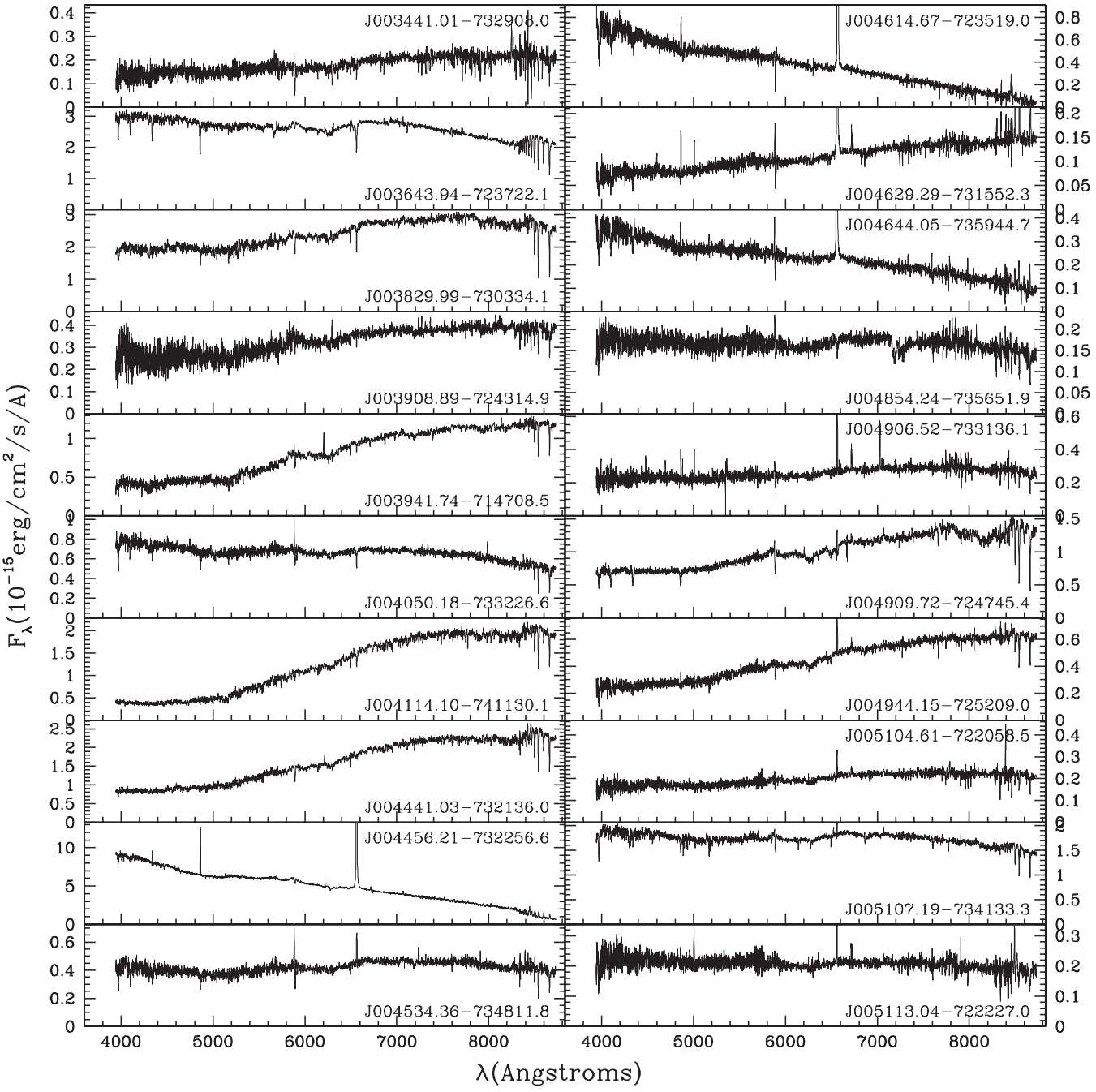

Figure C5. The low-resolution AAOmega optical spectra for the sample of high-probability q 1 post-AGB/RGB candidates. Occasionally, the spectra can have fluxes less than zero at the end due to poor sky subtraction. Note that for some objects the spectra of the region >7000 Åis dominated by noise introduced during sky subtraction. The emission feature near the sodium doublet is an artefact of the data reduction process resulting from poor sky subtraction of the sodium doublet emission from the SMC, Galaxy and the night sky. We note that, occasionally, the spectra can have fluxes less than zero at the end due to poor sky subtraction. The spectra are ordered by RA.

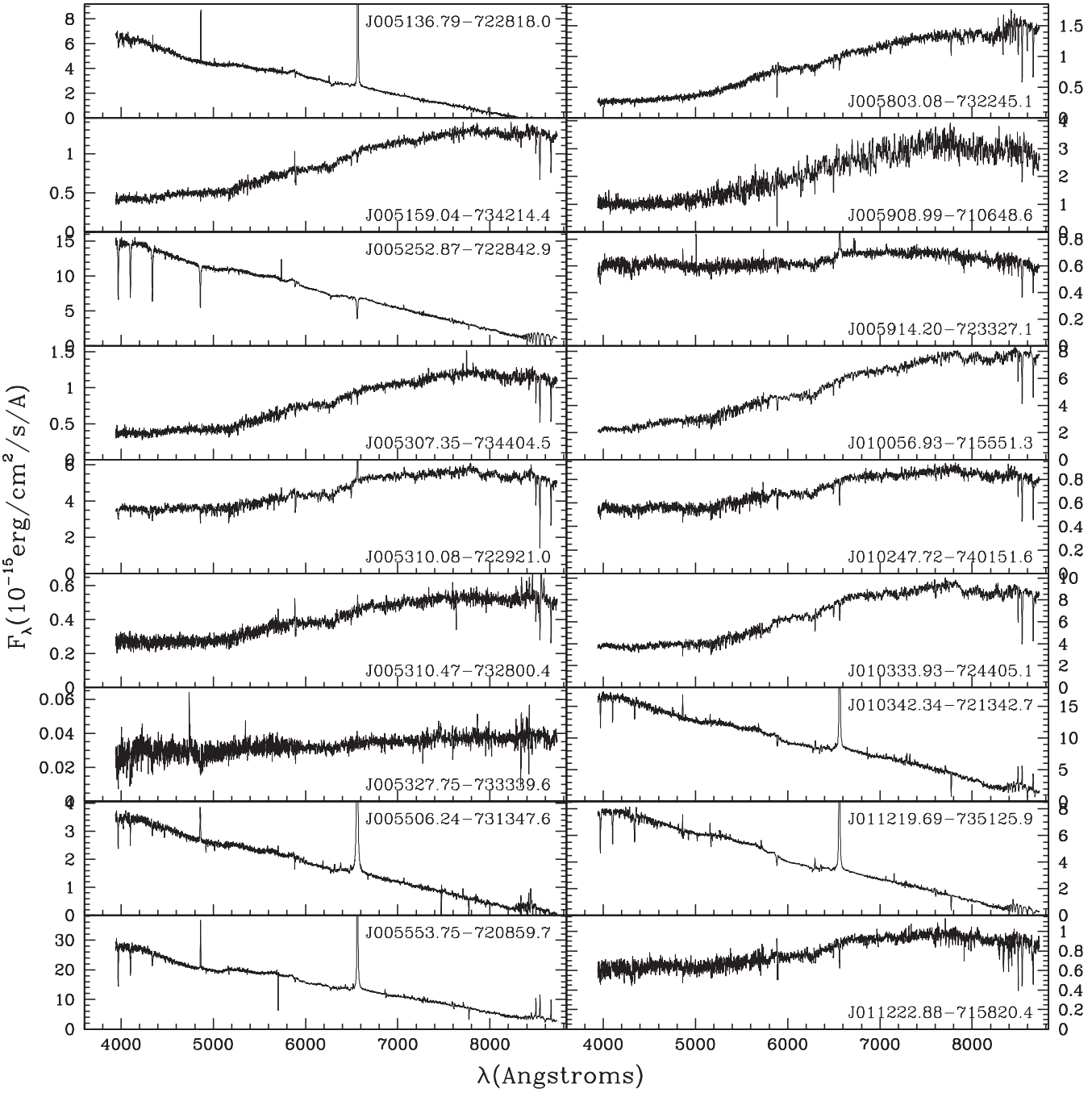

Figure C5 – *continued*

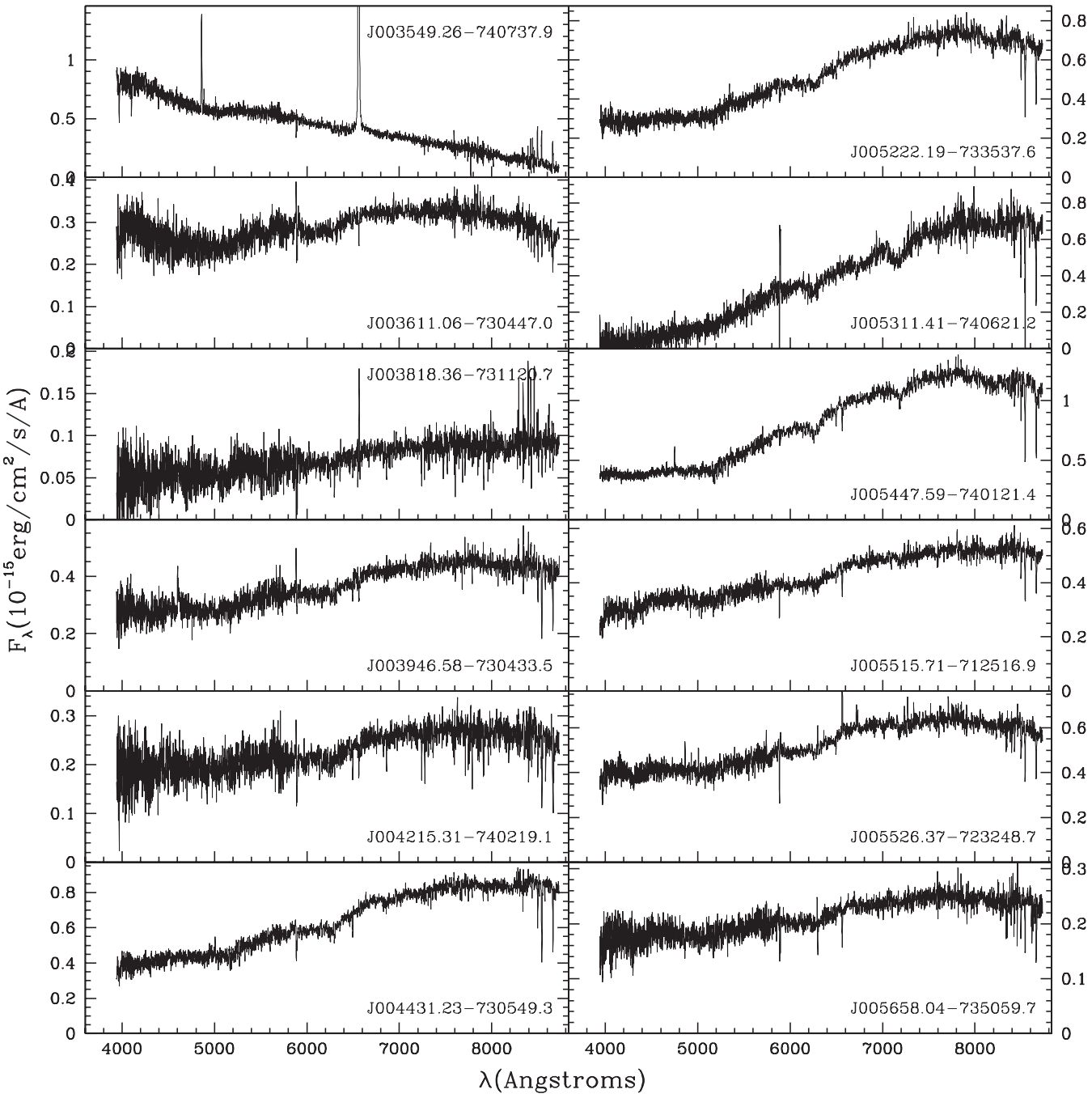

Figure C6. Same as Fig. C5, but for the high-probability quality 2 post-AGB/RGB candidates.

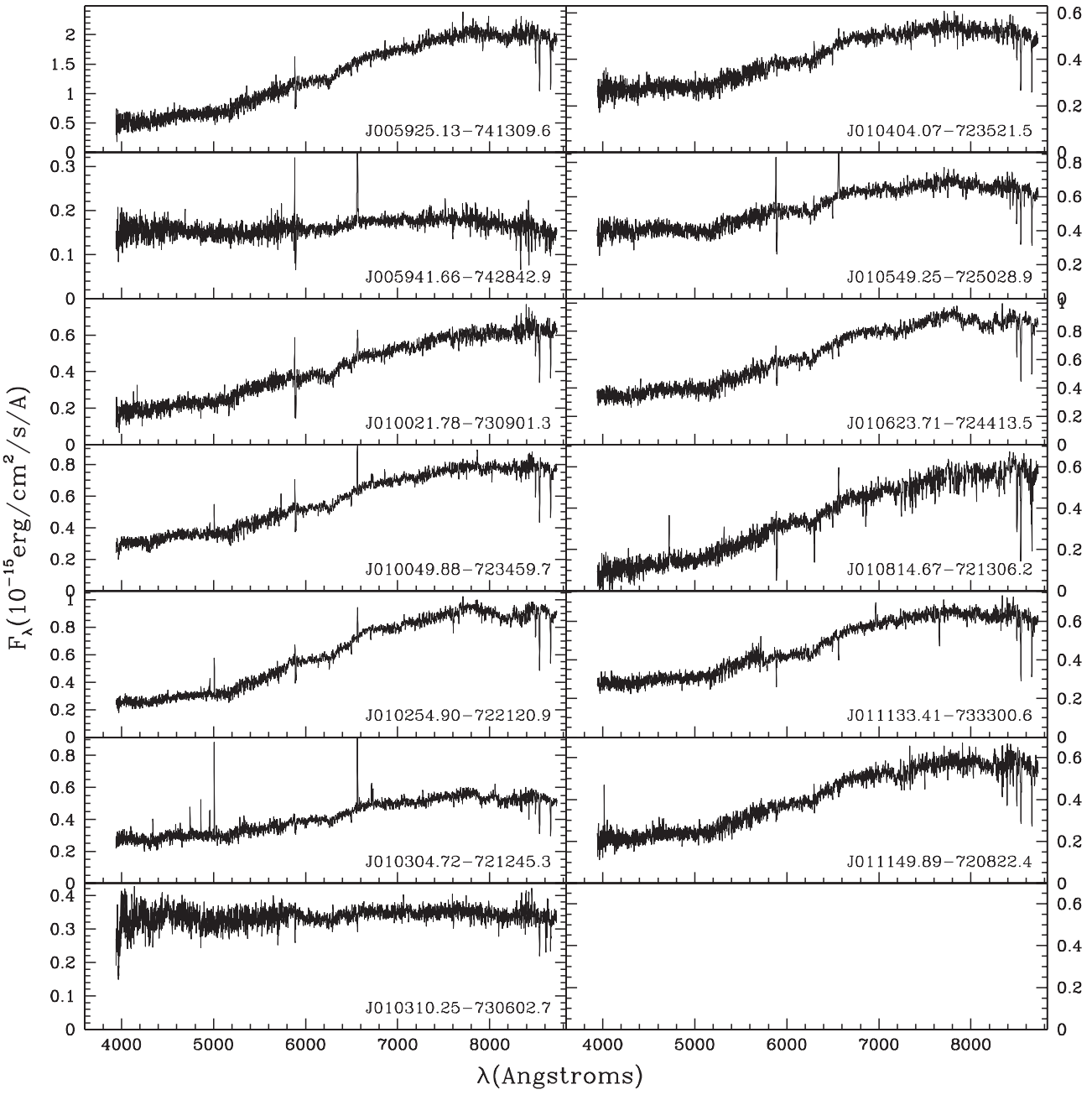

Figure C6 – *continued*

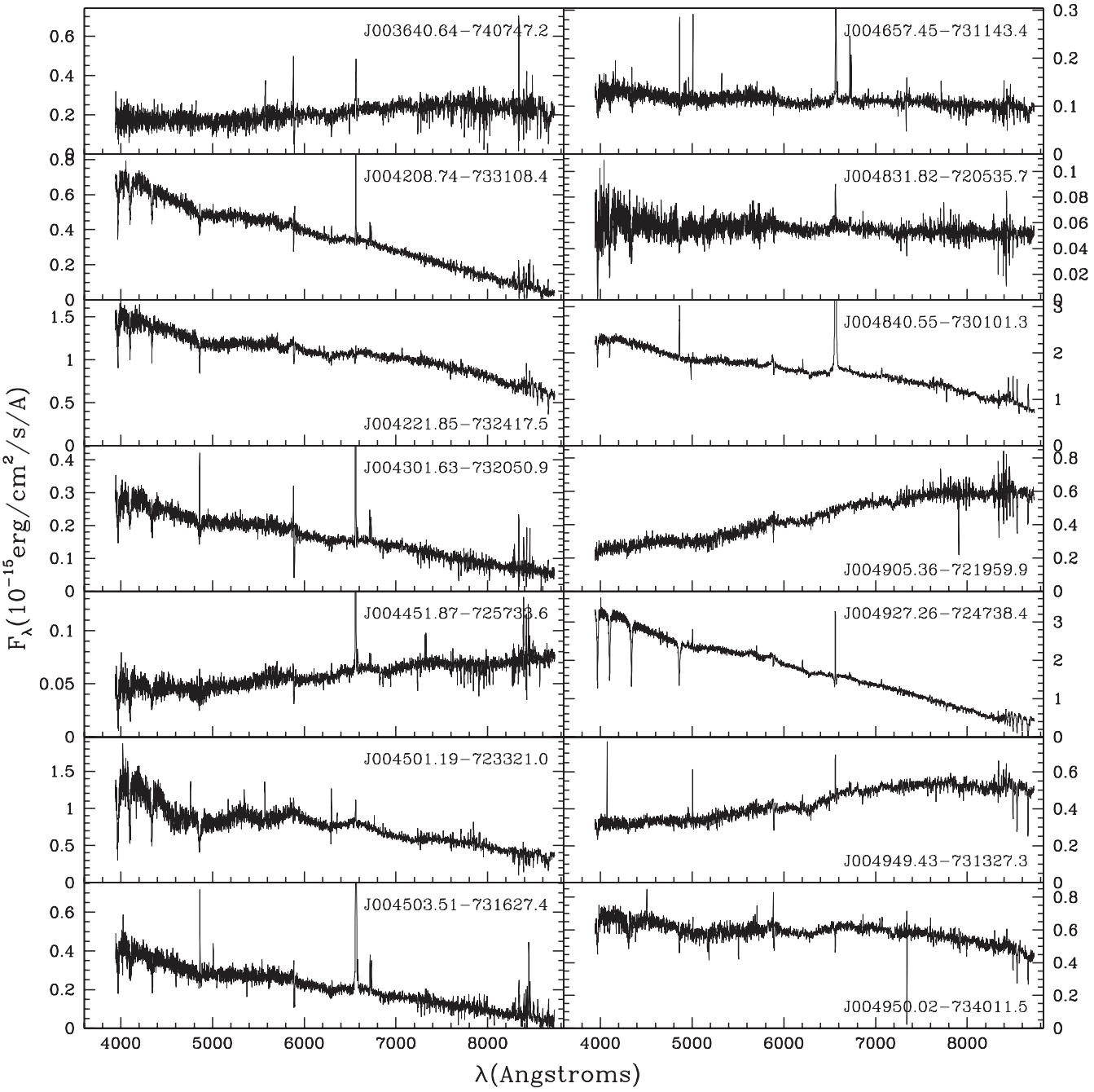

Figure C7. Same as Fig. C5 but for the high-probability quality 1 YSO candidates.

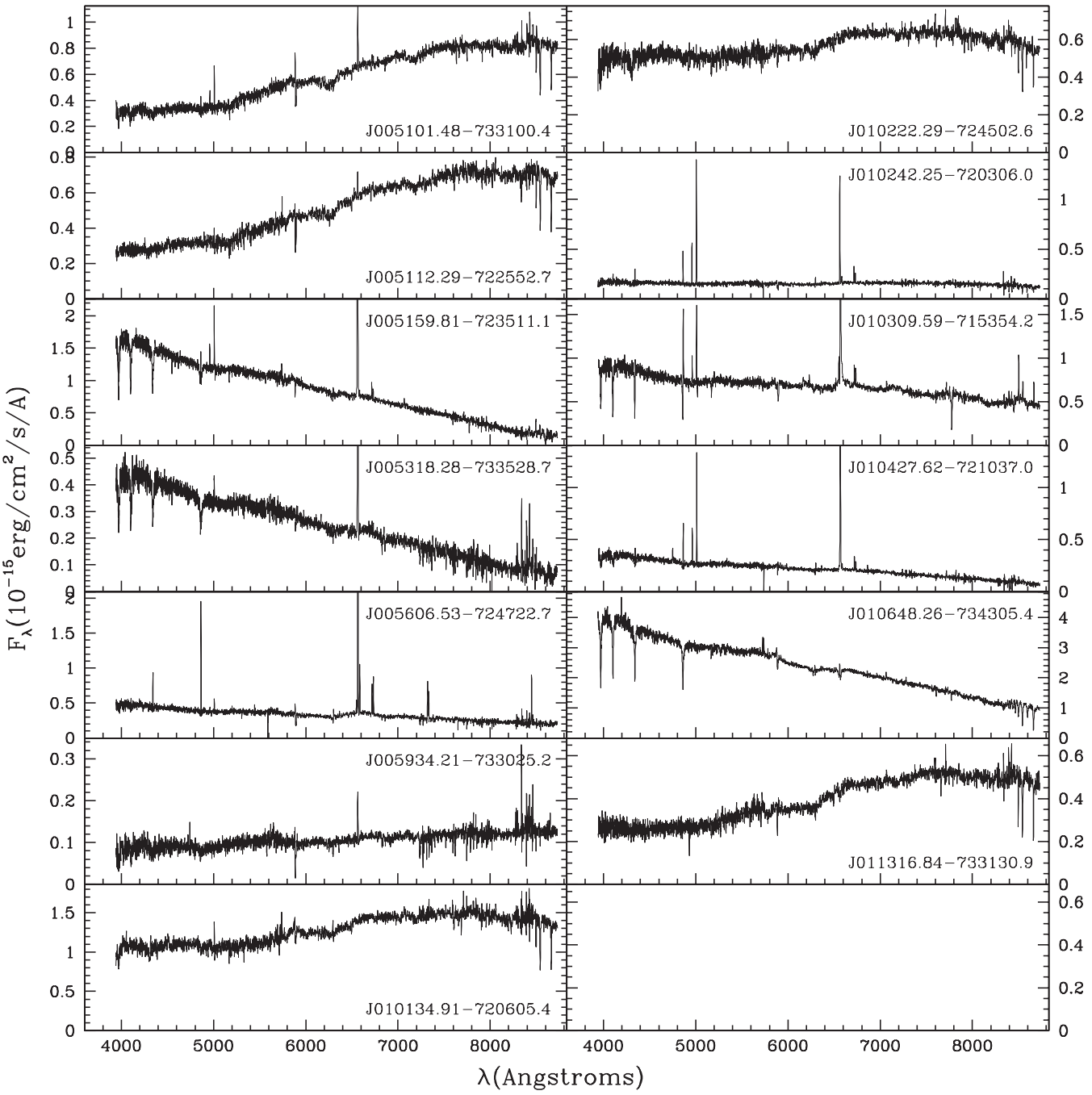

Figure C7 – *continued*

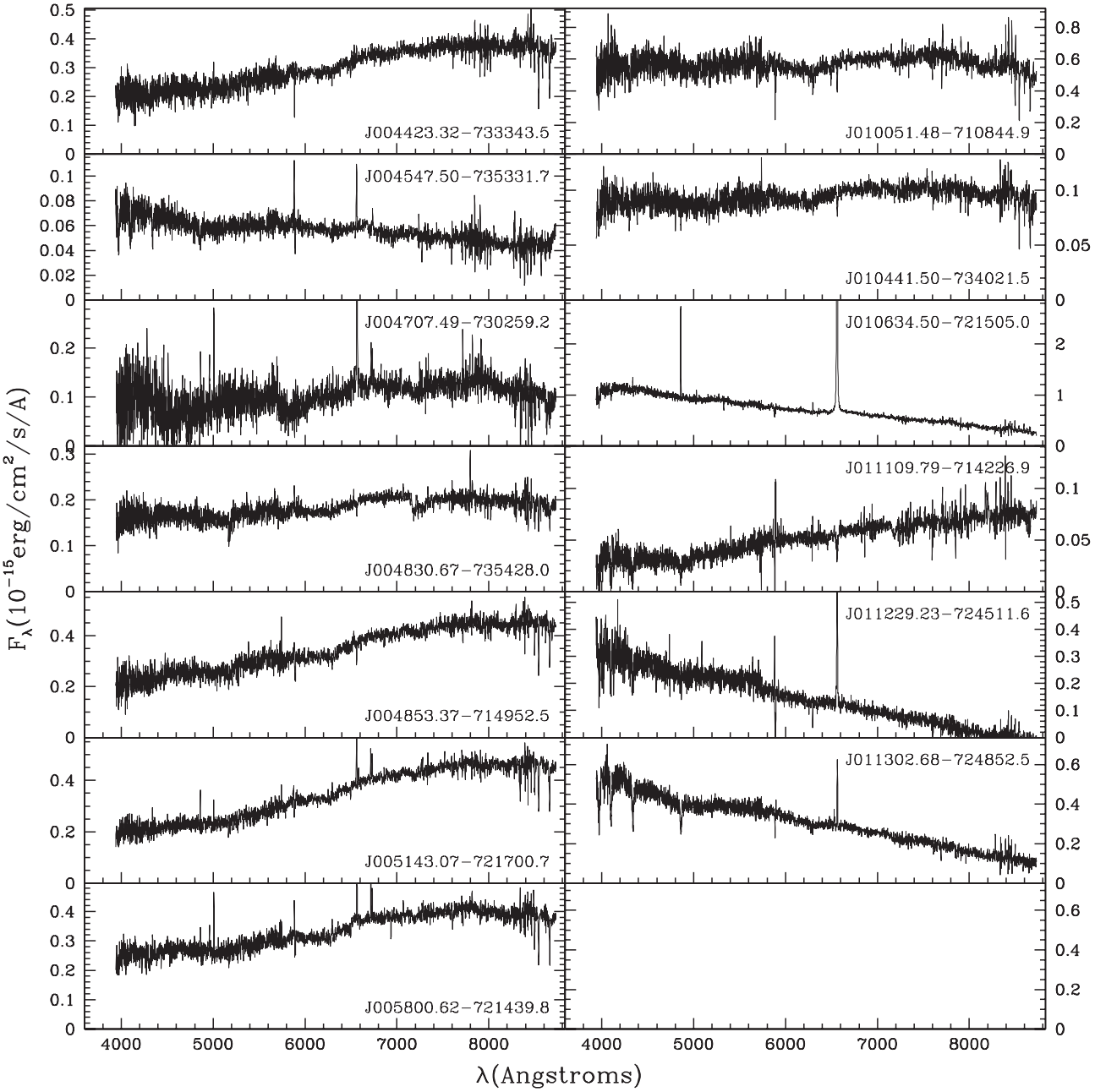

Figure C8. Same as Fig. C5 but for the high-probability quality 2 YSO candidates.

Table C1. Features in the spectra of the sample of Q1 post-AGB/RGB candidates. In this table 'a' represents absorption, 'e' represents emission, '0' indicates that the feature is not observed. ':' indicates that there is some line blending that has taken place or there is an absorption line with an emission core or the line indicates signs of strong winds and therefore mass-loss. '?' represents that the nature of the spectral line is uncertain. 'p' indicates a P-Cygni line profile. Note: the low-resolution of the spectra could possibly affect the identification of a given line.

Name	Hα	Hβ	Hγ	[O III]	[O III]	He I	He I	[S II]	[S II]	[N II]	[N II]	Ca II	Ca II	Ca II	Li	Ba	Pa
Wavelength (Å)	6563	4861	4341	4659	5007	4471	5876	6717	6731	6548	6584	8498	8542	8662	6708	4554	–
Candidates with [Fe/H] estimates from spectra																	
J003441.01-732908.0	a	0	0	0	0	0	0	0	0	0	0	a	a	a	0	0	0
J003643.94-723722.1	a	a	a	0	0	0	0	0	0	0	0	a	a	a	0	a	a
J003829.99-730334.1	a	a	a	0	0	0	0	0	0	0	0	a	a	a	0	0	0
J003908.89-724314.9	a	a	?	0	0	0	0	0	0	0	0	a	a	a	0	0	0
J003941.74-714708.5	a	a?	0	0	0	0	0	0	0	0	0	a	a	a	a?	0	0
J004050.18-733226.6	a	a	a	0	0	e	0	0	0	0	0	a	a	a	0	0	0
J004114.10-741130.1	a	a	0	0	0	0	0	0	0	0	0	a	a	a	0	a	a
J004441.03-732136.0	0	a:	a:	0	?	0	0	0	0	0	0	a	a	a	0	a	a
J004906.52-733136.1	e	e	e	0	0	e	e	e	e	e?	e?	a	a	a	a?	0	0
J004909.72-724745.4	e:	a:	a:	0	e	0	0	e	e	a:	0	a	a	a	a	0	a
J004944.15-725209.0	e	e	a	0	e	0	0	e	e	0	0	a	a	a	a	0	0
J005107.19-734133.3	e	a:	a	0	0	0	0	0	0	0	0	a	a	a	0	a	a
J005159.04-734214.4	a	a	0	0	0	0	0	0	0	0	0	a	a	a	a?	0	0
J005252.87-722842.9	a	a	a	0	0	0	0	e	e	0	0	a	a	a	0	0	a
J005307.35-734404.5	a	a	0	0	0	0	0	0	0	0	0	a	a	a	0	0	0
J005310.08-722921.0	e	a	a	0	0	0	0	0	0	0	0	a	a	a	0	0	0
J005803.08-732245.1	a	a:	a:	0	0	0	0	0	0	0	0	a	a	a	0	0	a
J005914.20-723327.1	e	e	0	0	e	0	0	e	e	0	0	a	a	a	0	0	0
J010056.93-715551.3	a	a	a	0	0	0	0	0	0	0	0	a	a	a	a	0	0
J010247.72-740151.6	a	a	0	0	0	0	0	0	0	0	0	a	a	a	0	a	0
J010333.93-724405.1	a	a	a	e	0	0	0	0	0	0	0	a	a	a	0	0	0
J011219.69-735125.9	e	e	a	0	0	a	a	0	0	0	0	a	a	a	0	0	a
J011222.88-715820.4	a	a?	a?	0	0	0	0	0	0	0	0	a	a	a	a?	0	0
Candidates with assumed [Fe/H] $= -1.00$																	
J004534.36-734811.8	e	a	a	0	0	0	0	0	0	0	0	0	0	0	0	0	a
J004456.21-732256.6	e	e	e:	0	a?:	a:	0	e	0	0	0	e	e	e	0	0	e
J004614.67-723519.0	e	e	0	0	0	0	0	0	0	0	0	0	0	0	0	0	0
J004629.29-731552.3	e	e	e:	0	e	0	0	e	e	0	0	0	0	0	a?	0	e
J004644.05-735944.7	e	e	a:	0	0	0	0	0	0	0	0	e	e	e	0	0	0
J004854.24-735651.9	a:	a:	0	0	0	0	0	0	0	0	0	a	a	a	0	0	0
J005104.61-722058.5	e	e:	?	0	e?	0	0	e	e	e?	e?	a?	a?	a?	0	0	0
J005113.04-722227.0	e	e	?	0	e	0	0	e	e	0	0	0	0	0	?	0	e:?
J005136.79-722818.0	e	e	e	0	e	0	0	0	0	0	0	0	0	0	0	0	e
J005310.47-732800.4	e	e	?	0	e	e?	?	?	?	?	?	a?	a?	a?	0	0	?
J005327.75-733339.6	e:	a	a	0	0	0	0	0	0	0	0	?	?	?	0	0	0
J005506.24-731347.6	e	e	a:	0	0	a	0	0	0	0	0	0	0	0	0	?	a
J005553.75-720859.7	e	e	a:	0	0	0	0	0	0	0	0	e	e	e	0	0	0
J005908.99-710648.6	e?	?	?	0	0	0	0	0	0	0	0	a	a	a	0	a	0
J010342.34-721342.7	e	e	a	0	e	a	0	0	0	0	0	e	e	e	0	0	0

Table C2. Same as Table C1, for the Q2 post-AGB/RGB candidates.

Name	Hα	Hβ	Hγ	[O III]	[O III]	He I	He I	[S II]	[S II]	[N II]	[N II]	Ca II	Ca II	Ca II	Li	Ba	Pa
Wavelength (Å)	6563	4861	4341	4659	5007	4471	5876	6717	6731	6548	6584	8498	8542	8662	6708	4554	–
Candidates with [Fe/H] estimates from spectra																	
J003611.06-730447.0	a	a?	0	0	0	0	0	0	0	0	0	0	a	0	0	0	0
J003818.36-731120.7	e	0	0	0	0	0	0	0	0	0	0	e?	a	a	0	0	0
J003946.58-730433.5	a	a?	0	0	0	0	0	0	0	0	0	a	a	a	0	0	0
J004215.31-740219.1	a	a	0	0	0	0	0	0	0	0	0	a	a	a	0	0	0
J004431.23-730549.3	e	0	0	0	e	0	e	0	0	0	0	a	a	a	0	0	0
J005222.19-733537.6	0	0	0	0	0	0	0	0	0	0	0	a	a	a	a?	0	0
J005311.41-740621.2	0	0	0	0	0	0	0	a?	a?	0	0	a	a	a	0	0	0
J005447.59-740121.4	a	a	0	0	0	0	0	e	e	0	0	a	a	a	0	0	0
J005515.71-712516.9	a	a	0	0	0	0	0	0	0	0	0	a	a	a	0	0	0
J005526.37-723248.7	e	e	0	0	e	0	0	e	e	0	0	a	a	a	0	0	0
J005658.04-735059.7	a	0	0	0	0	0	0	0	0	0	0	a	a	a	0	0	0
J005925.13-741309.6	a	a	a	0	0	e	0	0	0	0	0	a	a	a	a	0	0
J005941.66-742842.9	e	a	0	0	0	0	0	0	0	0	0	a	a	0	0	a?	0
J010021.78-730901.3	e	a	0	0	0	0	0	0	e	0	0	a	a	a	a	0	0
J010049.88-723459.7	e	e	0	e	e	0	0	e	e	0	0	a	a	a	a	0	0
J010254.90-722120.9	e	e	0	0	e	0	0	e?	e?	0	0	a	a	a	a?	0	0
J010304.72-721245.3	e	e	e	0	e	0	e:	e	e	e	e	a	a	a	0	0	0
J010310.25-730602.7	a:	a	0	0	0	0	0	0	0	0	0	a	a	a	0	0	0
J010404.07-723521.5	e:	e	0	0	0	0	0	0	0	0	0	a	a	a	0	0	0
J010549.25-725028.9	e	e	a	0	e	0	0	0	e	0	0	a	a	a	a?	0	0
J010623.71-724413.5	a	0	a	e	0	0	0	0	0	0	0	a	a	a	a	0	0
J010814.67-721306.2	e	0	a	0	0	0	0	0	0	0	0	a	a	a	a?	0	0
J011133.41-733300.6	a	a	0	0	0	0	0	0	0	0	0	a	a	a	0	0	0
J011149.89-720822.4	a	a	a	e	0	a	e	0	0	0	0	a	a	a	a?	0	0
Candidates with assumed [Fe/H] = −1.00																	
J003549.26-740737.9	e	e	0	0	0	0	0	0	0	0	0	e	e	e	0	0	0

Table C3. Same as Table C1, but for the Q1 YSO candidates.

Name	Hα	Hβ	Hγ	[O III]	[O III]	He I	He I	[S II]	[S II]	[N II]	[N II]	Ca II	Ca II	Ca II	Li	Ba	Pa
Wavelength (Å)	6563	4861	4341	4659	5007	4471	5876	6717	6731	6548	6584	8498	8542	8662	6708	4554	–
Candidates with [Fe/H] estimates from spectra																	
J004927.26-724738.4	e	a	a	0	e	0	0	e	e	0	0	a	a	a	a?	0	a
J004949.43-731327.3	e	0	0	e?	e	0	0	e	e	0	0	a	a	a	a	0	0
J010134.91-720605.4	0	a	0	0	e	0	0	0	0	0	0	a	a	a	0	0	0
J010222.29-724502.6	0	0	0	0	0	0	0	e	e	0	0	a	a	a	0	0	0
J010648.26-734305.4	e	a	a	0	0	0	0	0	0	0	0	a	a	a	0	0	a
J011316.84-733130.9	?	?	?	0	0	0	0	0	0	0	0	a	a	a	0	0	0
Candidates with assumed [Fe/H] = −1.00																	
J003640.64-740747.2	e	e:?	?	0	0	0	0	0	0	e?	e?	?	a	a	0	0	0
J004208.74-733108.4	e	e:	a:	e	e	a	0	e	e	0	0	e	e?	e?	0	0	0
J004221.85-732417.5	e	a	a	0	0	0	0	0	0	0	0	a	a	a	0	0	a
J004301.63-732050.9	e	e:	e:	0	0	e?	0	e	e	e?	0	0	0	0	0	0	0
J004451.87-725733.6	e	e	e:	0	0	0	0	e	e	0	0	0	0	0	0	0	e
J004501.19-723321.0	e	a:	a:	0	0	0	0	0	0	0	0	0	0	0	0	0	a?
J004503.51-731627.4	e	e	e:	0	0	0	0	e	e	0	0	0	0	0	0	0	e
J004657.45-731143.4	e	e	e	0	e	0	e	e	e	e?	e?	0	0	0	0	0	?
J004831.82-720535.7	e	a	a	0	0	0	0	e	e	0	0	a	a	a	a	0	0
J004840.55-730101.3	e	e	0	0	e?	0	e	e	e	0	0	e	e	e	0	0	e
J004905.36-721959.9	?	?	?	0	?	0	0	0	0	0	0	a	a	a	0	0	0
J004950.02-734011.5	a	a	a:?	0	0e?	0	0	0	0	0	0	a	a	a	0	0	0
J005101.48-733100.4*	e	e	?	e	e	?	?	e	e	e?	e?	a	a	a	0	a?	0
J005112.29-722552.7	e	e	?	e	e	e?	0	e	e	0	0	a	a	a	a?	0	0
J005159.81-723511.1	e	e:	a:	0	e	0	0	e	e	0	0	e	e	e	0	0	0
J005318.28-733528.7	e	a:	a:	0	e	0	0	e	e	0	0	0	0	0	0	0	0
J005606.53-724722.7	e	e	e	0	e	a:	0	e	e	0	0	0	0	0	0	0	0
J005934.21-733025.2	e	a:?	a:?	0	0	0	0	0	0	0	0	0	0	0	0	0	0
J010242.25-720306.0	e	e	e:	0	e	0	0	e	e	0	0	0	0	0	0	0	e
J010309.59-715354.2	e	ep	ep?	e?	e	?	0	e	e	e	e	e	e	e	0	0	0
J010427.62-721037.0	e	e	e:	0	e	e?	0	e	e	e	e	?	?	?	0	0	?

Table C4. Same as Table C1, but for the Q2 YSO candidates.

Name	Hα	Hβ	Hγ	[O III]	[O III]	He I	He I	[S II]	[S II]	[N II]	[N II]	Ca II	Ca II	Ca II	Li	Ba	Pa
Wavelength (Å)	6563	4861	4341	4659	5007	4471	5876	6717	6731	6548	6584	8498	8542	8662	6708	4554	–
Candidates with [Fe/H] estimates from spectra																	
J004423.32-733343.5	e	0	0	0	e	0	0	e	e	0	0	a	a	a	a	0	0
J004830.67-735428.0	a	0	0	0	0	0	0	0	0	0	0	a	a	a	0	0	0
J004853.37-714952.5	a	a	0	0	0	0	0	0	0	0	0	a	a	a	0	0	0
J005143.07-721700.7	e	e	e	0	e	0	e	e	e	0	0	a	a	a	0	0	0
J005800.62-721439.8	e	e	e	0	e	0	0	e	e	0	0	a	a	a	0	0	0
J010051.48-710844.9	a	a	0	0	0	0	0	0	0	0	0	a	a	a	0	0	0
J010441.50-734021.5	a	0	0	0	e	0	0	0	0	0	0	a	a	a	0	0	0
Candidates with assumed [Fe/H] = −1.00																	
J004547.50-735331.7	e	a:	a:	0	0	0	0	0	e:	0	0	0	0	0	0	0	0
J004707.49-730259.2	e	e	0	0	e	0	0	e	e	0	0	0	0	0	a?	0	0
J010634.50-721505.0	e	e	e	0	0	0	0	e	e	0	0	e	e	e	0	0	0
J011109.79-714226.9	a:	a:	a:	0	0	0	0	0	0	0	0	0	0	0	0	0	0
J011229.23-724511.6	e	e	a	0	0	0	0	0	0	0	0	e	e	e	0	0	0
J011302.68-724852.5	e	a:	a:	0	0	0	0	0	0	0	0	e	0	0	0	0	0

SUPPORTING INFORMATION

Additional Supporting Information may be found in the online version of this article:

Table 1. A photometric table (T1_full.txt) with the photometry of the 1194 initial sample of candidates.
2) A tar and gzipped file containing the spectral typing fit results (PDF format) for the final sample of post-AGB/RGB and YSO candidates. (CDS_SpectralTypingResult.tar.gz)
3) A tar and gzipped file (CDS_Spectra.tar.gz) containing the spectra (fits format) for the final sample of post-AGB/RGB and YSO candidates.

(http://mnras.oxfordjournals.org/lookup/suppl/doi:10.1093/mnras/stt2033/-/DC1).
Please note: Oxford University Press is not responsible for the content or functionality of any supporting materials supplied by the authors. Any queries (other than missing material) should be directed to the corresponding author for the article.

This paper has been typeset from a TEX/LATEX file prepared by the author.